UNIVERSIDADE FEDERAL DE MINAS GERAIS
Instituto de Ciências Exatas
Programa de Pós-graduação em Física

Everton Pereira de Andrade

STRAIN-DRIVEN OPTOELECTRONIC PROPERTIES OF $CsPb(Br_{1-x}Cl_x)_3$ PEROVSKITE NANOWIRES

Belo Horizonte
2025

Everton Pereira de Andrade

STRAIN-DRIVEN OPTOELECTRONIC PROPERTIES OF $CsPb(Br_{1-x}Cl_x)_3$ PEROVSKITE NANOWIRES

Doctoral Thesis Proposal presented to the Graduate Program in Physics at the Institute of Exact Sciences of the Federal University of Minas Gerais as a final requirement for obtaining the title of Doctor of Science.

Advisor: Gustavo de Almeida Magalhães Sáfar

Belo Horizonte
2025

Dados Internacionais de Catalogação na Publicação (CIP)

A554s Andrade, Everton Pereira de.
Strain-driven optoelectronic properties of $CsPb(Br_{1-x}Cl_x)_3$ perovskite nanowires / Everton Pereira de Andrade. – 2025.
95 f. : il.

Orientador: Gustavo de Almeida Magalhães Sáfar.
Tese (doutorado) – Universidade Federal de Minas Gerais, Departamento de Física.
Bibliografia: f. 57-62.

1. Semicondutores. 2. Nanofios. 3. Fotoluminescência. 4. Análise espectral. 5. Transições de fases. 6. Optoeletrônica. I. Título. II. Sáfar, Gustavo de Almeida Magalhães. III. Universidade Federal de Minas Gerais, Departamento de Física.

CDU – 537.311.322 (043)

Ficha catalográfica elaborada por Romário Martins Ribeiro – CRB6 3595
Biblioteca Professor Manoel Lopes de Siqueira – Departamento de Física - UFMG

UNIVERSIDADE FEDERAL DE MINAS GERAIS

ATA

ATA DA SESSÃO DE ARGUIÇÃO DA 445ª TESE DO PROGRAMA DE PÓS-GRADUAÇÃO EM FÍSICA, defendida por **EVERTON PEREIRA DE ANDRADE** orientado pelo professor Gustavo de Almeida Magalhães Sáfar para obtenção do grau de **DOUTOR EM CIÊNCIAS, área de concentração Física**. Às 09:00 horas do dia seis de outubro de dois mil e vinte e cinco reuniu-se, por videoconferência, a Comissão Examinadora composta pelos professores **Gustavo de Almeida Magalhães Sáfar** (Orientador - Departamento de Física/UFMG), **Edmar Avellar Soares** (Departamento de Física/UFMG), **Mário Sérgio de Carvalho Mazzoni** (Departamento de Física/UFMG), **Gilberto Rodrigues da Silva Júnior** (Departamento de Física/UFV), **Weber Hanry Morais e Feu** (Centro Federal de Educação Tecnológica de Minas Gerais) e **Franklin Massami Matinaga** (Centro de Desenvolvimento da Tecnologia Nuclear), para dar cumprimento ao Artigo 37 do Regimento Geral da UFMG, submetendo **EVERTON PEREIRA DE ANDRADE** à arguição de seu trabalho, que recebeu o título de **"Strain-Driven Optoelectronic Properties of $CsPb(Br_{1-x}Cl_x)_3$ Perovskite Nanowires"**. O candidato fez uma exposição oral de seu trabalho durante aproximadamente 50 minutos. Após esta, os membros da comissão prosseguiram com a sua arguição, e apresentaram seus pareceres individuais sobre o trabalho, concluindo pela aprovação do candidato.

Belo Horizonte, 06 de outubro de 2025.

Prof. Gustavo de Almeida Magalhães Sáfar
Orientador do estudante
Departamento de Física /UFMG

Prof. Edmar Avellar Soares
Departamento de Física /UFMG

Porf. Mário Sérgio de Carvalho Mazzoni
Departamento de Física /UFMG

Prof. Gilberto Rodrigues da Silva Júnior
Departamento de Física /UFV

Prof. Franklin Massami Matinaga
Centro de Desenvolvimento da Tecnologia Nuclear

Prof. Weber Hanry Morais e Feu
Centro Federal de Educação Tecnológica de Minas Gerais

Candidato: Everton Pereira de Andrade

Documento assinado eletronicamente por **Everton Pereira de Andrade**, **Usuário Externo**, em 07/10/2025, às 11:59, conforme horário oficial de Brasília, com fundamento no art. 5º do Decreto nº 10.543, de 13 de novembro de 2020.

Documento assinado eletronicamente por **Franklin Massami Matinaga**, **Professor do Magistério Superior**, em 07/10/2025, às 12:23, conforme horário oficial de Brasília, com fundamento no art. 5º do Decreto nº 10.543, de 13 de novembro de 2020.

Documento assinado eletronicamente por **Gustavo de Almeida Magalhaes Safar**, **Professor do Magistério Superior**, em 07/10/2025, às 12:57, conforme horário oficial de Brasília, com fundamento no art. 5º do Decreto nº 10.543, de 13 de novembro de 2020.

Documento assinado eletronicamente por **Gilberto Rodrigues da Silva Júnior**, **Usuário Externo**, em 07/10/2025, às 16:11, conforme horário oficial de Brasília, com fundamento no art. 5º do Decreto nº 10.543, de 13 de novembro de 2020.

Documento assinado eletronicamente por **Edmar Avellar Soares**, **Professor do Magistério Superior**, em 07/10/2025, às 17:11, conforme horário oficial de Brasília, com fundamento no art. 5º do Decreto nº 10.543, de 13 de novembro de 2020.

Documento assinado eletronicamente por **Mario Sergio de Carvalho Mazzoni**, **Membro**, em 08/10/2025, às 14:56, conforme horário oficial de Brasília, com fundamento no art. 5º do Decreto nº 10.543, de 13 de novembro de 2020.

Documento assinado eletronicamente por **Weber Hanry Morais e Feu**, **Usuário Externo**, em 10/10/2025, às 11:02, conforme horário oficial de Brasília, com fundamento no art. 5º do Decreto nº 10.543, de 13 de novembro de 2020.

A autenticidade deste documento pode ser conferida no site https://sei.ufmg.br/sei/controlador_externo.php?acao=documento_conferir&id_orgao_acesso_externo=0, informando o código verificador **4616773** e o código CRC **91E4C64C**.

Acknowledgments

First and foremost, I am grateful to God for granting me strength, perseverance, and the opportunities that have guided me throughout this journey.

I owe my deepest gratitude to my family. To my wife, Gabriela Fernanda, for standing unwaveringly by my side and offering unconditional support in every circumstance. To my parents, Ervio and Dulcinéia, for their boundless encouragement, motivation, and trust. To my brother, Esdras, for inspiring me with his genuine enthusiasm for my work and studies. I am also thankful for the incomparable emotional support provided by my dogs and other pets, whose companionship has been a constant source of comfort.

I am profoundly indebted to my advisor, Professor Gustavo de Almeida Magalhães Sáfar, who has guided me from my earliest steps in research to the conclusion of this doctorate, shaping the scientist I have become. His insightful discussions, thoughtful advice, and steadfast dedication to my career have been invaluable. I also extend my sincere thanks to the Nanoscopia UHV Laboratory team, including Professors Rogério Magalhães Paniago and Angelo Malachias, whose unique scientific and personal perspectives have enriched my academic path while always fostering a supportive group environment. I would further like to thank Professor Luiz Alberto Cury for his generous guidance, professional advice, and ability to convey vast knowledge through subtle yet impactful insights.

I also acknowledge all past and present members of the Nanoscopia UHV Laboratory from 2016 to 2025. While I cannot name each individually, I am sincerely grateful for the contributions, conversations, and moments of camaraderie that have shaped my academic and personal growth.

My gratitude extends as well to the staff and members of the IMBUIA beamline at CNPEM, for their technical support, scientific input, and warm reception during experiments, with special thanks to Dr. Francisco Maia.

I am equally thankful to all collaborators who contributed to publications during my doctoral studies. Their commitment and expertise were essential in advancing this work.

Finally, I would like to acknowledge the *LCPnano* for providing access to equipment that significantly enhanced the quality of this research. I am also grateful to the funding agencies *CAPES*, CNPq, FAPEMIG, and INCT Nanocarbono, whose support made this entire journey possible.

"Research is what I'm doing when I don't know what I'm doing."

Wernher von Braun

Abstract

This doctoral thesis investigates the optoelectronic properties of metal halide perovskite (MHP) nanowires, with emphasis on heterostructured $CsPb(Br_{1-x}Cl_x)_3$ systems. The nanowires were synthesized using a template-assisted epitaxial growth process followed by controlled gas-phase anion exchange in an Ar/Cl_2 atmosphere, enabling the formation of axially stepped heterojunctions with tunable halide composition. Atomic force microscopy (AFM) revealed high morphological uniformity, with average lengths of 3–5 μm and diameters of $\sim$250 nm. Photoluminescence (PL) mapping demonstrated clear spectral gradients across the heterojunction, with emission peaks shifting from 523 nm in the Br-rich region to 507 nm in the Cl-rich region.

Temperature-dependent PL and time-correlated single-photon counting (TCSPC) measurements revealed a remarkable enhancement of exciton lifetimes near crystallographic phase transitions, particularly around 305 K in the Cl-rich domains and 361 K in Br-rich nanowires. Bi-exponential decay analysis showed that while the radiative recombination channel remained nearly stable, the non-radiative channel exhibited a pronounced slowdown at the transition, leading to lifetimes up to three times longer than the baseline values. This behavior was reproducible across multiple thermal cycles and was accompanied by hysteresis in the PL peak position, indicating structural reordering.

To interpret these results, the nanowires are modeled as disordered strain superlattices, where ferroelastic domains and flexoelectric polarization gradients modulate the electronic band structure and exciton dynamics. This framework highlights the interplay between strain, phase transitions, and carrier recombination in low-dimensional perovskite systems.

Overall, this work provides fundamental insights into how structural phase transitions extend exciton lifetimes and tune the optical response of $CsPb(Br_{1-x}Cl_x)_3$ nanowires. These findings establish design principles for exploiting ferroelasticity and flexoelectricity in perovskite nanostructures, with direct implications for high-efficiency optoelectronic devices such as solar cells, light-emitting diodes, and pho-

todetectors operating under elevated temperatures and concentrated illumination.

Keywords: Metal halide perovskites; $CsPb(Br_{1-x}Cl_x)_3$ nanowires; photoluminescence; time-resolved spectroscopy; exciton dynamics; ferroelasticity; flexoelectricity; phase transitions; photon recycling; optoelectronics.

Resumo

Esta tese de doutorado investiga as propriedades optoeletrônicas de nanofios de perovskitas inorgânicas de haletos de chumbo, com ênfase em sistemas heteroestruturados de $CsPb(Br_{1-x}Cl_x)_3$. Os nanofios foram sintetizados por crescimento epitaxial assistido por template de óxido de alumínio anódico (AAO), seguido de processo controlado de troca aniônica em fase gasosa em atmosfera de Ar/Cl_2, permitindo a formação de heterojunções axiais com composição aniônica ajustável. As medidas de microscopia de força atômica (AFM) revelaram elevada uniformidade morfológica, com comprimentos médios de 3–5 μm e diâmetros em torno de 250 nm. Os mapeamentos de fotoluminescência (PL) evidenciaram gradientes espectrais ao longo da heterojunção, com picos de emissão variando de 523 nm na região rica em Br até 507 nm na região rica em Cl.

As medidas de PL e de correlação temporal de fótons únicos (TCSPC) em função da temperatura revelaram aumento notável no tempo de vida excitônico próximo às transições de fase cristalográficas, particularmente em torno de 305 K nas regiões ricas em Cl e de 361 K nos nanofios ricos em Br. A análise biexponencial mostrou que, enquanto o canal radiativo de recombinação manteve-se praticamente estável, o canal não radiativo apresentou forte desaceleração próximo às transições, levando a tempos de vida até três vezes superiores aos valores de base. Esse comportamento foi reproduzido em múltiplos ciclos térmicos e acompanhado por histerese na posição dos picos de PL, indicando reordenação estrutural.

Para interpretar esses resultados, os nanofios foram modelados como super-redes desordenadas de deformações, em que domínios ferroelásticos e gradientes de polarização flexoelétrica modulam a estrutura eletrônica e a dinâmica excitônica. Esse quadro destaca a interação entre deformações, transições de fase e recombinação de portadores em sistemas perovskíticos unidimensionais.

No conjunto, este trabalho fornece uma compreensão fundamental de como transições de fase cristalográficas prolongam o tempo de vida excitônico e ajustam a resposta óptica de nanofios de $CsPb(Br_{1-x}Cl_x)_3$. Os resultados estabelecem princípios de projeto para explorar ferroelasticidade e flexoeletricidade em nanoestruturas

de perovskita, com implicações diretas para o desenvolvimento de dispositivos optoeletrônicos de alta eficiência, como células solares, diodos emissores de luz e fotodetectores, especialmente em condições de operação acima da temperatura ambiente e sob iluminação concentrada.

Palavras-chave: Perovskitas de haletos metálicos; nanofios de $CsPb(Br_{1-x}Cl_x)_3$; fotoluminescência; espectroscopia resolvida no tempo; dinâmica excitônica; ferroelasticidade; flexoeletricidade; transições de fase; reciclagem de fótons; optoeletrônica.

Summary

1 Introduction **14**

2 Literature Review **16**

2.1 Perovskites 17

2.2 Crystalline Structure and Bravais Lattices 18

2.3 Metal Halide Perovskites (MHPs) 21

2.4 Ferroelasticity 23

2.4.1 Ferroelasticity in Metal Halide Perovskites 24

2.5 Strain 25

2.5.1 Strain and Ferroelasticity in Perovskites 26

2.6 Phase Transitions 27

2.7 Flexoelectricity 28

2.7.1 Applications of Flexoelectricity 28

3 Experimental Techniques **30**

3.1 Atomic Force Microscopy (AFM) 30

3.2 Photoluminescence (PL) Spectroscopy 33

3.3 Time-Correlated Single Photon Counting (TCSPC) 35

3.4 Synthesis 37

3.4.1 Synthesis of $CsPb(Br_{1-x}Cl_x)_3$ Nanowires (NWs) 38

4 Results and Discussion **43**

4.1 Detailed Results and Analysis of $CsPb(Br_{1-x}Cl_x)_3$ Nanowires 44

4.1.1 Morphological Characterization 44

4.1.2 Photoluminescence (PL) Characterization 45

4.1.3 Exciton Dynamics and Lifetime Measurements 47

4.1.4 Ferroelasticity and Flexoelectricity 50

4.1.5 Photoluminescence Peak Shifts and Strain Effects 53

5 Conclusion **55**

References **56**

Appendix A - Additional Data **63**

Appendix B - List of Complete Publications and Collaborations **73**

Appendix C - Published Article: $CsPb(Br_{1-x}Cl_x)_3$ Nanowires **75**

Chapter 1

Introduction

The exploration of novel materials with remarkable optoelectronic properties has become a central theme in modern materials science and condensed matter physics. Among the wide range of candidates, metal halide perovskites (MHPs) have attracted tremendous interest due to their versatile applications in photovoltaics, nanophotonics, and optoelectronics. Their outstanding combination of strong light absorption, tunable bandgaps, long carrier diffusion lengths, and defect tolerance make them highly suitable for next-generation devices such as solar cells, light-emitting diodes (LEDs), and photodetectors [1–4].

In particular, perovskite nanowires (NWs) offer unique opportunities for exploring fundamental optoelectronic processes at the nanoscale. Their geometry provides efficient charge transport pathways, enhanced light guiding, and strong coupling between structural and electronic degrees of freedom, enabling integration into nanoscale optoelectronic architectures. Beyond their technological potential, perovskite NWs also represent an excellent platform for investigating the interplay between structural dynamics and excitonic behavior, especially near crystallographic phase transitions.

This thesis focuses on the synthesis, optical characterization, and strain-driven effects in $CsPb(Br_{1-x}Cl_x)_3$ nanowires. These NWs were fabricated using an epitaxial deposition method in anodized aluminum oxide (AAO) templates, followed by a controlled gas-phase anion exchange process to generate heterojunction structures with tunable halide composition. This approach enables the engineering of axial heterostructures where Br-rich and Cl-rich domains coexist within the same nanowire, thus allowing systematic investigation of bandgap gradients and interface effects.

A central theme of this work is the role of strain and ferroelasticity in modulating the optoelectronic response of perovskite nanowires. It is well established that MHPs undergo structural phase transitions (e.g., orthorhombic-to-tetragonal

and tetragonal-to-cubic), which can strongly influence their optical properties and carrier dynamics. However, the microscopic mechanisms connecting ferroelastic domain formation, flexoelectric polarization, and exciton recombination in confined nanostructures remain insufficiently understood [2, 5]. Addressing this knowledge gap is critical not only for advancing fundamental science but also for guiding the design of stable and efficient perovskite-based devices.

The experimental approach presented in this thesis combines atomic force microscopy (AFM), steady-state photoluminescence (PL), temperature-dependent PL, and time-resolved PL (TRPL) to provide a comprehensive view of exciton dynamics in $CsPb(Br_{1-x}Cl_x)_3$ nanowires. Special emphasis is placed on identifying how ferroelastic reordering and flexoelectric polarization gradients influence photoluminescence peak shifts, exciton lifetimes, and hysteresis effects across thermal cycles. The analysis is framed within the concept of *disordered strain superlattices*, in which local strain gradients reorganize during phase transitions and thereby modulate the mean free path and recombination probability of excitons.

By integrating synthesis, advanced spectroscopy, and theoretical interpretation, this thesis aims to contribute new insights into the fundamental mechanisms linking strain, ferroelasticity, and exciton dynamics in metal halide perovskite nanowires. These findings not only shed light on the physics of perovskite nanostructures but also establish guiding principles for exploiting strain engineering, photon recycling, and ferroelastic effects in the development of high-performance optoelectronic devices.

Chapter 2

Literature Review

This chapter provides a comprehensive review of the fundamental physical phenomena and material systems relevant to the research presented in this thesis. The focus is on the development of metal halide perovskites (MHPs), with particular attention to their optoelectronic properties, the role of strain effects such as ferroelasticity and flexoelectricity, and their synthesis in the form of nanowires.

The review begins with a discussion of the unique electronic and optical characteristics of MHPs, including their defect tolerance, strong light absorption, and bandgap tunability. Emphasis is placed on how crystallographic phase transitions and strain-driven effects influence exciton dynamics and charge transport. Particular consideration is given to ferroelastic domain reordering and flexoelectric polarization, which have recently been recognized as important mechanisms for modulating recombination pathways and extending carrier lifetimes [1, 2, 6, 7].

In addition, the synthesis of perovskite nanowires is reviewed, with a focus on template-assisted growth and subsequent halide exchange processes that enable the formation of heterostructured $CsPb(Br_{1-x}Cl_x)_3$ nanowires. Previous studies have demonstrated that these heterostructures allow spatial control of bandgap composition, enabling gradual shifts in emission profiles and providing a platform for investigating excitonic behavior in confined geometries.

By analyzing the current state of research in this field, this chapter establishes the necessary background for understanding the synthesis strategies, experimental techniques, and theoretical framework used in this thesis. The literature review highlights the relevance of heterostructured perovskite nanowires to the broader context of nanotechnology and optoelectronics, emphasizing their potential for integration into advanced light-emitting devices, photodetectors, and photovoltaics.

2.1 Perovskites

Perovskites are an important class of crystalline materials that play a significant role in various fields of physics and materials science. The goal of this doctoral thesis project is to investigate the optoelectronic properties of a type of perovskite known as metal halide perovskites (MHPs), exploring their structures, compositions, and applications in optoelectronic devices [1].

The term *perovskite* is derived from the natural mineral of the same name, which was named after Russian mineralogist Lev Perovski in the 19th century. The perovskite mineral, with the chemical formula $CaTiO_3$, was first discovered in Russia. Its distinctive crystal structure (see Figure 2.1) has inspired the creation of a wide family of synthetic materials with diverse properties [6].

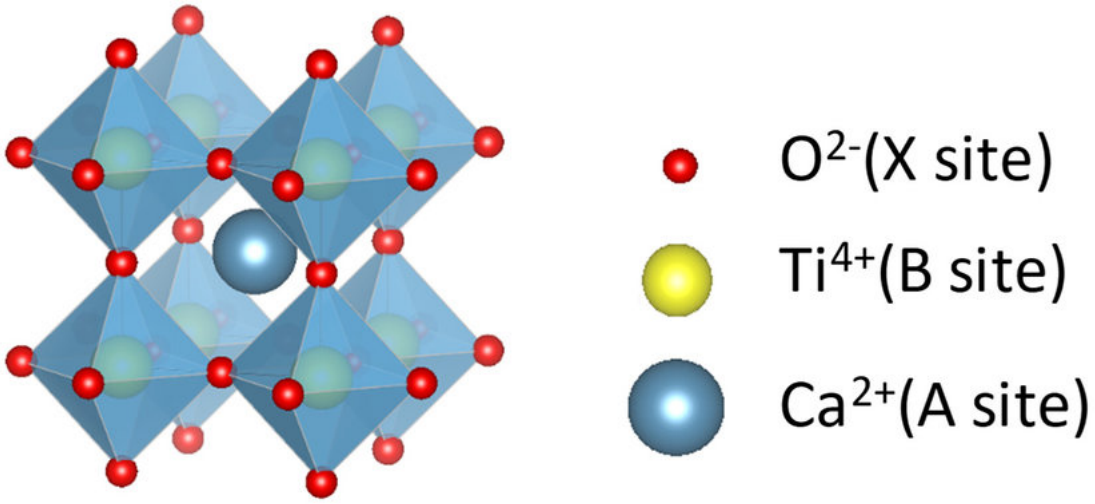

Figura 2.1: Crystal structure of the mineral perovskite $CaTiO_3$, highlighting the positions of the calcium cation (Ca^{2+}) at the A site, the titanium cation (Ti^{4+}) at the B site, and oxygen anions (O^{2-}) at the X site. This structure serves as the prototype for the broader family of perovskite materials, including metal halide perovskites used in modern optoelectronic devices.

Perovskites are found in many areas of physics and materials science, including:

- **Photovoltaics**: Metal halide perovskites have demonstrated high efficiency in solar cells, becoming a leading material in the development of next-generation photovoltaic technologies [7, 8].

- **Light Emitting Diodes (LEDs)**: The tunable bandgap and high photoluminescence quantum yield of perovskites make them excellent candidates for light-emitting devices [1, 2].

- **Ferroelectric and Ferroelastic Materials**: Some perovskites exhibit ferroelectric or ferroelastic properties, which are essential for memory storage, actuators, and other electronic applications [2].

- **Superconductivity**: Certain perovskite oxides have been found to exhibit high-temperature superconductivity, an area of ongoing research [9].

- **Thermoelectric Materials**: Perovskite materials are being explored for their ability to convert heat into electricity, making them promising for energy harvesting [7].

In the last decade, halide perovskites, particularly those incorporating lead and tin, have revolutionized the field of photovoltaics. Their high efficiency in converting solar energy into electricity has led to rapid advancements in solar cell technology, with potential applications in tandem solar cells and flexible electronics [1, 2].

2.2 Crystalline Structure and Bravais Lattices

Before we dive into the specifics of Bravais lattices, it is essential to understand the general concept of a crystalline structure. A crystalline structure refers to the organized, repeating arrangement of atoms, ions, or molecules in a solid. Unlike amorphous materials, where the atomic arrangement is random, crystals possess a high degree of symmetry due to the periodicity in their atomic structure [10,11]. This periodicity can be described mathematically using translational symmetry, where the entire structure can be generated by repeating a specific arrangement of atoms (called a unit cell) in three-dimensional space. The unit cell is the smallest repeating unit that fully defines the crystal structure, and its geometry and atomic arrangement determine the material's macroscopic properties, such as optical behavior, conductivity, and mechanical strength [10, 12].

Mathematically, a crystal structure can be described by a set of lattice vectors, denoted as $\mathbf{a}_1$, $\mathbf{a}_2$, and $\mathbf{a}_3$, which define the position of atoms within the unit cell relative to an origin. Any point in the crystal lattice can be expressed as:

$$\mathbf{R} = n_1\mathbf{a}_1 + n_2\mathbf{a}_2 + n_3\mathbf{a}_3$$

where n_1, n_2, and n_3 are integers, and represents the position vector of the point in the lattice. Crystals can be further classified into primitive and non-primitive lattices. In a primitive lattice, the unit cell contains only one lattice point, while

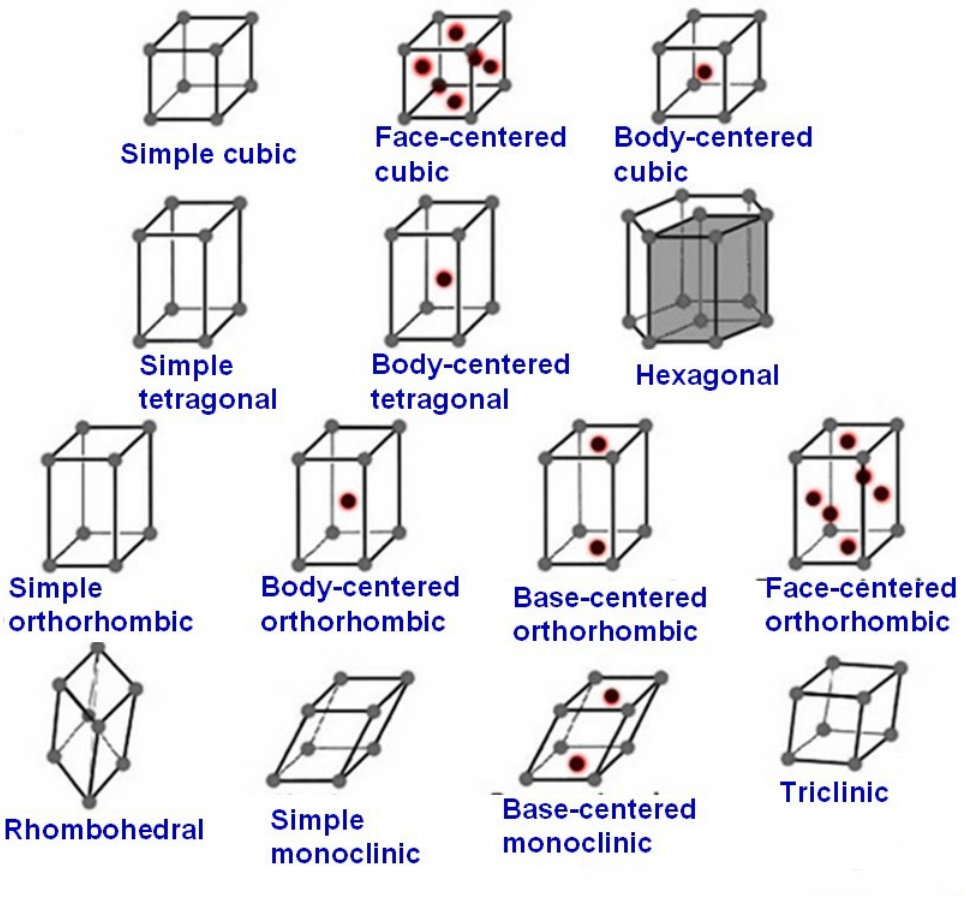

Figura 2.2: The 14 Bravais lattices in three dimensions, categorized into seven crystal systems. Each lattice represents a geometric arrangement of unit cells, defining how atoms are periodically arranged in space. Understanding these basic lattices is essential for comparing simpler crystal structures with more complex systems like perovskites [13].

non-primitive lattices contain additional lattice points, often at the center or face of the unit cell [10, 11].

Another critical aspect of crystalline structures is their symmetry. In addition to translational symmetry, crystals may have rotational, mirror, and inversion symmetries, classified through point groups and space groups, which describe all possible symmetry operations for a given structure [10]. These symmetries greatly influence the material's electronic properties, particularly its electron band structure, which determines whether a material behaves as a conductor, semiconductor, or insulator [11, 12].

Crystals are often categorized using Bravais lattices, which define all possible periodic arrangements of points in three-dimensional space. There are 14 distinct Bravais lattices (see Figure 2.2), categorized into seven crystal systems: cubic, tetragonal, orthorhombic, hexagonal, rhombohedral, monoclinic, and triclinic [13, 14].

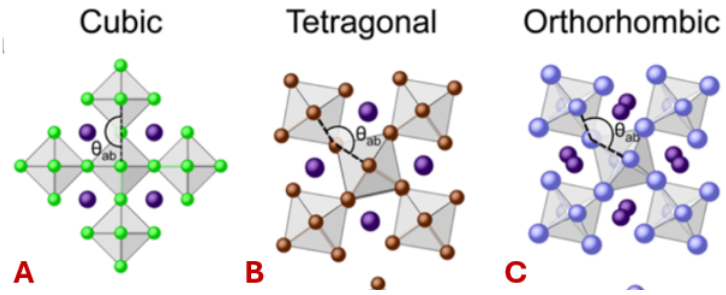

Figura 2.3: Schematic representation of the most common crystallographic phases in halide perovskites. (A) Cubic phase, characterized by a symmetric arrangement of corner-sharing octahedra with minimal distortion. (B) Tetragonal phase, in which the octahedra exhibit a slight tilt that reduces the in-plane bond angle θ_{ab}. (C) Orthorhombic phase, showing stronger octahedral tilting and distortion, typically stabilized at lower temperatures. The progressive decrease in symmetry from cubic to orthorhombic directly influences the electronic band structure and optical properties of the material.

Each crystal system describes the shape of the unit cell and its angles. For example:

- **Cubic System**: The most symmetric, with all sides equal and all angles at 90° [10].
- **Tetragonal and Orthorhombic Systems**: Less symmetric, with sides of different lengths but still maintaining orthogonal angles [11].
- **Hexagonal System**: Defined by two equal-length sides and one distinct side, with angles of 120° between the equal sides [14].

The crystal structure of perovskites follows the general chemical formula ABX_3, where:

- A is a large cation, often an alkali metal or organic molecule, positioned at the center of a cubic unit cell.
- B is a smaller metal cation, typically a transition metal like lead or tin, located at the corners of the unit cell.
- X represents halide anions, positioned at the face centers, forming an octahedral coordination with the B-site cation.

The perovskite structure belongs to the cubic crystal system, forming a three-dimensional network of corner-sharing octahedra. However, this ideal cubic configuration can distort depending on external factors such as temperature or pressure,

leading to changes in bond angles and lattice parameters that directly influence its physical properties [11, 13]. Figure 2.3 illustrates the most common crystallographic configurations observed in halide perovskites: (A) cubic, (B) tetragonal, and (C) orthorhombic phases, which typically appear as a function of temperature.

The ability of perovskites to deform and tilt their octahedral network is key to their unique ferroelastic and ferroelectric properties, which are essential for applications in optoelectronic devices [10, 13].

2.3 Metal Halide Perovskites (MHPs)

Metal halide perovskites (MHPs) are a groundbreaking class of materials that have garnered significant attention in recent years, especially in the fields of photovoltaics and optoelectronics. These materials belong to the perovskite family but stand out due to their unique combination of elements, which grants them exceptional optoelectronic properties. The basic structure of an MHP follows the perovskite formula ABX_3 (see Figure 2.4), where the cation A is typically a monovalent species like cesium (Cs^+) or organic cations like methylammonium (MA^+) and formamidinium (FA^+). The B cation is often a divalent metal such as lead (Pb^{2+}) or tin (Sn^{2+}), and the X site is occupied by halide anions such as iodine (I^-), bromine (Br^-), or chlorine (Cl^-) [15].

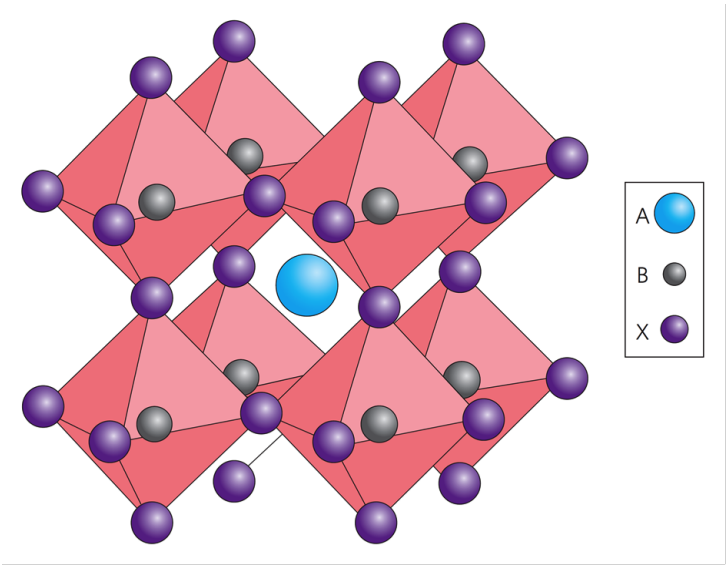

Figura 2.4: Schematic representation of an ideal unit cell for the perovskite structure ABX_3, showing the octahedral coordination and the central A-site cation [13].

This particular arrangement of cations and anions results in a crystal structure that is highly efficient for light absorption and charge carrier generation, making

MHPs ideal candidates for various optoelectronic applications. MHPs exhibit a direct bandgap, which can be precisely tuned by adjusting the halide composition at the X-site. For example, increasing iodine content narrows the bandgap, enhancing the material's ability to absorb a broader range of the solar spectrum. On the other hand, bromine-rich perovskites are particularly useful in light-emitting devices due to their superior photoluminescence quantum yields. The tunable bandgap and high absorption coefficients of MHPs make them extremely promising materials for solar energy conversion, having already achieved power conversion efficiencies exceeding 25%, rivaling traditional silicon-based solar cells [16].

Structurally, MHPs consist of:

- **A monovalent cation** (such as cesium (Cs^+) for inorganic perovskites, or organic cations like methylammonium (MA^+) or formamidinium (FA^+) for hybrid perovskites).
- **A divalent transition metal cation** (commonly lead (Pb^{2+}) or tin (Sn^{2+})).
- **Halide anions** (like iodine (I^-), bromine (Br^-), or chlorine (Cl^-)).

The versatility of this structure is key to the performance of perovskite-based devices. Their efficiency in capturing light and converting it into electrical energy stems from the crystal structure's ability to allow easy movement of charge carriers—electrons and holes—across the material. This is particularly important in solar cells, where the effectiveness of energy conversion hinges on minimizing recombination losses and enhancing charge mobility.

One of the advantages of MHPs is their ease of fabrication. Unlike conventional semiconductors such as silicon, which require high-temperature processing, MHPs can be fabricated using solution-based methods at relatively low temperatures. Techniques such as spin-coating, vapor deposition, and printing have been employed to produce high-quality perovskite films for use in devices like solar cells, LEDs, and photodetectors. Notably, in this thesis, the growth of MHP nanowires was achieved using anodic aluminum oxide (AAO) templates, which provides an efficient method for producing well-defined nanostructures. This method, alongside other fabrication techniques, enables the integration of MHPs into flexible electronic devices, paving the way for next-generation technologies such as wearable solar cells and foldable displays [17].

The potential of MHPs in optoelectronic applications extends beyond just solar cells. Their tunable optical properties make them suitable for light-emitting diodes (LEDs), lasers, and photodetectors. The ability to control their bandgap, depending

on the halide used, allows the emission of light across the visible spectrum, from red to green to blue. This makes MHPs attractive candidates for high-efficiency, color-tunable LEDs, with applications in displays and lighting.

Despite their remarkable properties, one of the key challenges for MHPs production is their stability. These materials are known to degrade under environmental stresses such as moisture, oxygen, and elevated temperatures. Degradation often leads to a loss of optoelectronic performance over time, which poses a significant challenge for their widespread commercialization. However, recent developments in material engineering and encapsulation technologies have improved their stability, with some devices now demonstrating operational lifetimes approaching those of established technologies. Strategies such as substituting lead with tin or germanium, improving surface passivation, and developing multi-layer encapsulation techniques are actively being explored to enhance the long-term stability of MHP devices [18].

In summary, metal halide perovskites hold immense promise for a variety of optoelectronic applications, including solar cells, LEDs, and flexible electronics. The combination of their unique crystal structure, tunable optical properties, and ease of fabrication gives them an edge over traditional semiconductor materials. While challenges remain, particularly concerning their stability, ongoing research into new material compositions and device architectures continues to push the boundaries of what MHPs can achieve.

2.4 Ferroelasticity

Ferroelasticity is a property of certain crystalline materials where a spontaneous and reversible shape change occurs in response to mechanical stress. This deformation is driven by a structural phase transition between two or more stable crystal configurations, referred to as ferroelastic domains. The domains reorient under stress, allowing the material to deform without permanent structural changes [3, 19].

Ferroelastic materials possess two or more stable phases, and they switch between these phases under the influence of stress, similar to how ferroelectric and ferromagnetic materials exhibit spontaneous electric or magnetic polarization, respectively [10, 11]. In these materials, mechanical stress induces a reorientation of the crystal lattice, leading to a phase transition between different variants of the crystal structure. The strain associated with this transition is reversible upon stress removal.

Mathematically, ferroelasticity can be described by the relationship between

strain (ϵ) and stress (σ):

$$\sigma = C \cdot \epsilon + D \cdot S$$

where σ is the applied stress, ϵ is the strain, C is the elastic compliance tensor, and S is the spontaneous strain due to domain reorientation [19]. The spontaneous strain term describes internal deformation during a phase transition.

The concept of ferroelastic domain switching involves the movement of domain walls, which separate regions of different ferroelastic variants. Domain switching allows large, reversible deformations under stress, and the coercive stress is the threshold beyond which permanent domain switching occurs [20]. Below this threshold, the material behaves elastically, while above it, a phase transition between ferroelastic domains occurs.

Ferroelasticity is valuable for applications such as:

- **Actuators**: These materials convert stress into controlled deformation, useful in precision systems such as MEMS [19].
- **Shape Memory Alloys**: Materials like NiTi undergo reversible shape changes with heating, widely used in medical and aerospace fields [3].
- **Sensors**: Ferroelastic materials can detect strain, making them ideal for structural health monitoring [20].
- **Memory Devices**: Ferroelasticity enables non-volatile memory applications based on domain switching [19].
- **Energy Harvesting**: The large deformations can be used to generate electricity in piezoelectric devices [21].

2.4.1 Ferroelasticity in Metal Halide Perovskites

Ferroelasticity has been observed in metal halide perovskites (MHPs), particularly in hybrid perovskites like methylammonium lead iodide ($CH_3NH_3PbI_3$). These materials undergo phase transitions between cubic and tetragonal phases, forming ferroelastic domains that affect their optoelectronic properties [3, 19]. The interaction of ferroelastic domain walls with charge carriers can influence the efficiency of perovskite solar cells [21].

In the context of this thesis, ferroelastic behavior in perovskite nanowires is critical for enhancing mechanical and optoelectronic properties. Domain wall motion and spontaneous strain could improve charge carrier mobility, contributing to higher efficiency in flexible devices [3, 20].

Ferroelasticity has broad applications, especially in flexible electronics and nanotechnology. Understanding this phenomenon at the nanoscale may lead to breakthroughs in quantum computing, energy harvesting, and optoelectronics [21].

2.5 Strain

Strain is a measure of deformation that quantifies how much a material stretches or compresses when subjected to an external force or stress. This concept is fundamental in solid mechanics and is critical for understanding how materials respond to mechanical forces [10, 11]. The strain is dimensionless and can be expressed as the ratio of the change in length to the original length:

$$\epsilon = \frac{\Delta L}{L_0}$$

where ΔL is the change in length, and L_0 is the original length. Strain can be extended to three dimensions using the strain tensor ϵ_{ij}, defined by:

$$\epsilon_{ij} = \frac{1}{2}\left(\frac{\partial u_i}{\partial x_j} + \frac{\partial u_j}{\partial x_i}\right)$$

where u_i and u_j are the displacements in the i and j directions, respectively [19]. Strain can be classified into two main types: normal strain, which occurs along the axis of applied force, and shear strain, where deformation is parallel to a plane. Both types can be elastic (recoverable) or plastic (permanent) [21].

At the nanoscale, strain has a pronounced effect on the mechanical and electronic properties of materials. For example, thin films deposited on substrates often experience strain due to lattice mismatch, which can drastically alter their physical properties, such as band structure, phase transitions, or magnetic behavior [19]. Strain engineering enables the precise control of these properties, offering a pathway to design materials with tailored functionalities [22].

In perovskite nanowires, strain is a crucial factor that influences optoelectronic properties. The flexible crystal structure of perovskites allows for the accommodation of strain, which can modify the material's electronic band structure, enhancing performance in devices such as solar cells and LEDs [23]. Strain can also induce ferroelastic domains, affecting the dynamics of charge carriers in perovskite-based devices [19].

The ability to control strain has led to its widespread application in various fields:

- **Semiconductor Devices**: Strain is used to enhance carrier mobility in transistors, improving the performance of microelectronics [23].

- **Piezoelectric Sensors and Actuators**: Strain in piezoelectric materials generates electric fields, used in precision sensors and energy harvesting devices [23].

- **Optoelectronics**: Strain can tune the bandgap of semiconductors, enhancing the efficiency of optoelectronic devices such as lasers and detectors [24].

- **Straintronics**: This emerging field uses strain to control electronic and magnetic properties, providing energy-efficient alternatives to traditional electronics [23].

2.5.1 Strain and Ferroelasticity in Perovskites

Strain and ferroelasticity are closely linked in metal halide perovskites. In materials like $CsPb(Br_{1-x}Cl_x)_3$, strain can induce ferroelastic domain switching, which significantly impacts the material's electronic and optical behavior. For example, strain gradients in nanowires can result in flexoelectric polarization, which influences exciton behavior and recombination dynamics [23]. Strain mapping, as shown in Figure 2.5, reveals how localized strain influences ferroelastic domains and their effect on optoelectronic performance.

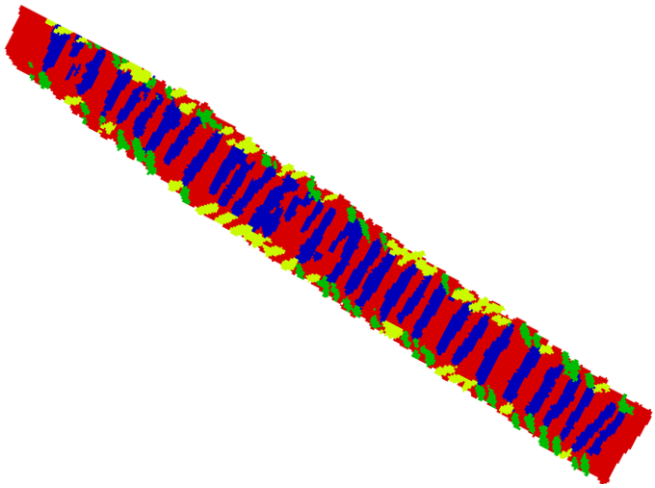

Figura 2.5: Strain mapping of a perovskite nanowire, highlighting compressive and tensile strain distribution, which can affect ferroelastic domain behavior and optoelectronic properties [25].

Understanding how strain interacts with ferroelasticity in perovskites is critical for optimizing their performance in applications ranging from solar cells to flexible electronics [24].

2.6 Phase Transitions

Phase transitions are fundamental processes in material science where a substance changes its phase or state in response to external parameters, such as temperature, pressure, or electromagnetic fields. These transitions involve abrupt changes in the physical properties of the material, such as its structure, electrical conductivity, optical properties, and mechanical behavior [26, 27].

At the microscopic level, phase transitions are driven by changes in the arrangement of atoms or molecules within a material, often resulting from competition between thermal energy and cohesive forces between particles. When a material crosses a critical threshold, such as the melting point or Curie temperature, it undergoes a structural reconfiguration [26, 28].

Phase transitions are commonly classified as:

- **First-Order Phase Transitions**: These are characterized by discontinuities in the first derivative of the free energy (e.g., volume, entropy), where the material absorbs or releases latent heat. Examples include melting and freezing [28, 29].

- **Second-Order Phase Transitions**: These transitions show continuous first derivatives of free energy but discontinuities in second-order derivatives. They involve critical phenomena like divergence of correlation lengths, seen in ferromagnetic transitions at the Curie point [26, 30].

In crystalline solids, phase transitions typically involve changes in the lattice structure, known as *crystallographic phase transitions*. For instance, metal halide perovskites exhibit transitions between cubic and tetragonal phases, impacting their optoelectronic properties such as band structure and charge mobility [26, 31].

In perovskite nanowires, such as $CsPb(Br_{1-x}Cl_x)_3$, phase transitions significantly influence optical behavior, with the orthorhombic to tetragonal transition affecting photoluminescence and exciton dynamics [28]. These transitions are essential for applications in solar cells and LEDs, where performance can be optimized by tuning phase behavior [6, 31].

The ability to control phase transitions is essential for improving optoelectronic performance. In devices like solar cells, optimizing phase behavior can lead to enhanced charge mobility and greater device stability under varying environmental conditions, such as high temperatures [26, 31].

Applications of phase transitions in various fields include:

- **Electronic Devices**: Phase transitions can modulate electrical and optical properties in semiconductors, improving transistors and memory devices [26, 28].

- **Energy Storage**: Phase-change materials store and release heat efficiently, useful in thermal management and memory technologies [28].

- **Optoelectronics**: Controlling phase transitions in perovskites enhances their efficiency in solar cells and LEDs [26, 31].

2.7 Flexoelectricity

Flexoelectricity refers to the phenomenon where electric polarization is induced in a dielectric material due to a non-uniform mechanical strain, i.e., a strain gradient. Unlike piezoelectricity, which is restricted to non-centrosymmetric materials, flexoelectricity is present in all dielectric materials and becomes particularly significant at the nanoscale, where strain gradients can be substantial [32, 33].

The flexoelectric effect can be described by the following constitutive relation:

$$P_i = \mu_{ijkl} \frac{\partial \epsilon_{kl}}{\partial x_j}$$

where P_i is the induced polarization in the i-direction, μ_{ijkl} is the flexoelectric coefficient (a fourth-rank tensor), and $\frac{\partial \epsilon_{kl}}{\partial x_j}$ represents the gradient of the strain tensor [34]. Flexoelectricity is particularly relevant in nanoscale materials due to the large strain gradients often observed in these systems [33].

To distinguish flexoelectricity from piezoelectricity, it is useful to compare their constitutive relations. While piezoelectricity is a first-order effect, producing polarization in response to uniform stress, flexoelectricity is a second-order effect, depending on strain gradients. Flexoelectric effects thus become dominant in nanostructures such as thin films and nanowires, where strain gradients are naturally large [32].

In perovskite nanowires, such as $CsPb(Br_{1-x}Cl_x)_3$, the presence of strain gradients due to mechanical deformations can induce flexoelectric polarization, which in turn influences charge carrier dynamics, exciton recombination rates, and overall optoelectronic performance [35]. The ability to control these effects is essential for optimizing devices like solar cells and LEDs [36].

2.7.1 Applications of Flexoelectricity

Flexoelectricity has numerous potential applications, particularly in nanotechnology and electromechanical systems:

- **Nanoscale Sensors**: Flexoelectric materials can be used to design highly sensitive strain and force sensors at the nanoscale, critical for applications in biomedical engineering and MEMS [32, 34].

- **Energy Harvesting**: Flexoelectric materials convert mechanical energy from strain gradients into electrical energy, making them suitable for energy harvesting in wearable devices and flexible electronics [35, 37].

- **Tunable Dielectric Devices**: Flexoelectricity allows the design of tunable capacitors and dielectric devices where mechanical strain modulates dielectric properties [32].

- **Electromechanical Coupling in Nanostructures**: The strong electromechanical coupling in nanostructures like nanowires and thin films due to flexoelectricity opens up new possibilities for advanced optoelectronic applications [33].

In summary, flexoelectricity is a versatile phenomenon with significant implications for nanotechnology, enabling new functionalities in nanoscale sensors, energy harvesting devices, and electromechanical systems. In the context of metal halide perovskite nanowires, flexoelectricity plays a crucial role in modulating optoelectronic properties, contributing to the development of more efficient photovoltaic and optoelectronic devices [36].

Chapter 3

Experimental Techniques

In this chapter, the principles and techniques employed for the synthesis and characterization of $CsPb(Br_{1-x}Cl_x)_3$ perovskite nanowires are presented. The methods discussed include template-assisted growth, halide anion exchange, and a range of optical and microscopy techniques used to investigate their structural, morphological, and optoelectronic properties. Special emphasis is placed on atomic force microscopy (AFM), photoluminescence (PL) spectroscopy, temperature-dependent measurements, and time-correlated single photon counting (TCSPC), which together provide a comprehensive framework for understanding the excitonic behavior and strain effects in these nanostructures.

3.1 Atomic Force Microscopy (AFM)

Atomic Force Microscopy (AFM) is a high-resolution imaging technique that allows for the topographical mapping of surfaces at the nanometer scale. Unlike optical microscopes that are limited by the diffraction of light, AFM can achieve atomic-level resolution by scanning a sharp tip across the surface of a sample [38]. AFM is widely used in materials science, nanotechnology, and biology to study surface properties, morphology, and mechanical characteristics of a wide range of materials.

At the core of AFM is a cantilever with a sharp tip, typically made of silicon or silicon nitride, that interacts with the sample surface. As the tip approaches and interacts with the surface, forces between the tip and the sample cause the cantilever to deflect. These forces include van der Waals forces, electrostatic forces, chemical bonding, magnetic interactions, and mechanical forces depending on the sample's composition and the mode of operation [39].

The deflection of the cantilever is monitored by a laser beam reflected off the

back of the cantilever into a position-sensitive photodetector. The force F acting on the tip can be described by Hooke's law:

$$F = -k \cdot z,$$

where k is the stiffness (spring constant) of the cantilever and z is the deflection of the cantilever. The high sensitivity of the cantilever allows AFM to measure minute forces on the order of piconewtons (pN) [40].

AFM operates in several modes depending on the interaction between the tip and the sample. The three most commonly used modes are:

- **Contact Mode**: The tip makes physical contact with the surface. The deflection of the cantilever is kept constant, and vertical movement is translated into a topographical image. This mode is useful for hard surfaces but may damage soft materials [38].
- **Non-Contact Mode**: The tip oscillates slightly above the surface. The attractive van der Waals forces shift the cantilever's resonance frequency, allowing surface mapping without direct contact. This mode is ideal for fragile samples [40].
- **Tapping Mode**: The cantilever oscillates near its resonance frequency, intermittently tapping the surface to reduce lateral forces. This mode balances high-resolution imaging with minimal sample damage, making it ideal for soft or sticky materials [39].

In addition to imaging, AFM can be used for quantitative measurements of various material properties (see Figure 3.1):

- **Force-Distance Curves**: These provide insights into mechanical properties like stiffness, adhesion, and elasticity, valuable for biological materials and polymers [38].
- **Surface Roughness**: AFM measures surface roughness, critical in fields like semiconductor manufacturing and materials science [40].
- **Phase Imaging**: In tapping mode, phase shifts provide information about material properties such as viscoelasticity and stiffness [39].
- **Electrostatic and Magnetic Force Microscopy (EFM/MFM):** Although both techniques are derived from atomic force microscopy (AFM), they require specific cantilevers and operational modes. In EFM, a conductive tip and an applied bias are used to detect variations in surface potential through long-range

electrostatic forces. In MFM, a magnetically coated cantilever is employed to sense magnetic field gradients arising from surface magnetic domains. These extensions of AFM enable the mapping of local electrical or magnetic properties, complementing topographical information [40].

- **Kelvin Probe Force Microscopy (KPFM):** A derivative mode of AFM that employs a conductive cantilever and an applied bias to measure local surface potential and work function with nanometric resolution. By detecting electrostatic forces between the tip and the sample, KPFM provides quantitative information essential for studying charge distribution and electronic properties in semiconductor materials [38].

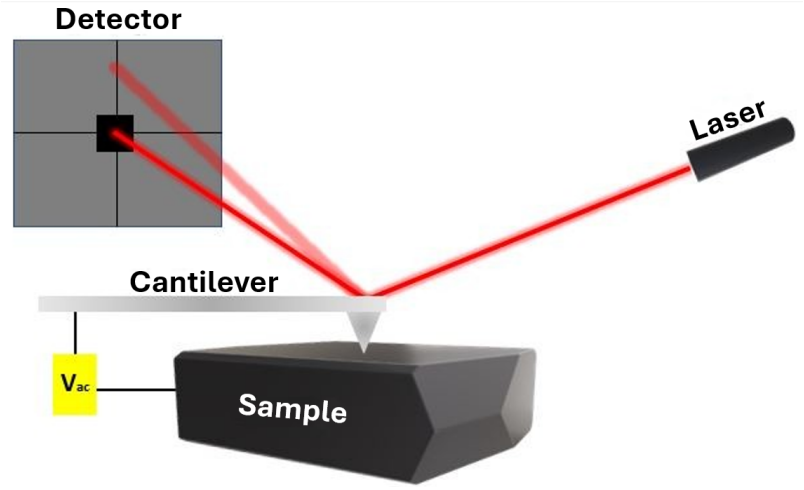

Figura 3.1: Schematic representation of the Atomic Force Microscopy (AFM) setup. A laser is focused on the back of the cantilever, and the reflected beam is detected by a position-sensitive detector. As the cantilever interacts with the sample surface, its deflection provides information about the surface topography and mechanical properties of the sample. The applied voltage (V_{ac}) enables additional measurements such as electrostatic or magnetic force microscopy depending on the mode of operation.

AFM plays a crucial role in this thesis. For $CsPb(Br_{1-x}Cl_x)_3$ nanowires, AFM is used to measure dimensions and surface morphology, verifying the uniformity of nanowire growth.

AFM has broad applications in nanotechnology, biology, and materials science:

- **Nanotechnology**: AFM is essential for nanofabrication and inspection of nanoscale features [39].

- **Biology and Medicine**: AFM is used to study the mechanical properties of cells, proteins, and biomolecules [40].

- **Materials Science**: AFM helps characterize surface roughness, hardness, and friction, important for evaluating material performance [38].

AFM remains one of the most versatile tools for surface analysis at the nanoscale, providing essential insights into the structural and mechanical properties of nanostructures [38, 40].

3.2 Photoluminescence (PL) Spectroscopy

Photoluminescence (PL) is a widely used optical technique that enables the study of the electronic structure of materials through the detection of light emitted from a material after photon absorption. When a material absorbs photons with sufficient energy, electrons are excited from the valence band to the conduction band, creating electron-hole pairs (excitons). These excitons eventually recombine, emitting light at characteristic wavelengths, providing insights into the material's electronic band structure, defect states, and other important properties [41, 42].

The energy of the emitted photons, E_{PL}, can be described as:

$$E_{PL} = h\nu = E_c - E_v - \Delta E,$$

where h is Planck's constant, ν is the emission frequency, E_c is the conduction band minimum, and E_v is the valence band maximum. The correction term ΔE accounts for factors that shift the emission below the free band-to-band transition. These include primarily the exciton binding energy (E_b), which lowers the emission energy relative to the electronic bandgap, as well as possible contributions from defect-related states and other non-radiative interactions such as phonon coupling [43, 44].

Therefore, photoluminescence does not measure the bare bandgap directly, but rather the effective optical transition energy, which reflects the interplay between the band structure, excitonic effects, and defect states.

PL is a non-destructive and versatile tool used in many material systems including semiconductors, organic materials, and nanostructures. It provides several key advantages:

- **Defect Sensitivity**: PL is highly sensitive to defects and impurities, crucial for studying nanowires and thin films [41, 45].

- **Bandgap Determination**: By analyzing the emission spectrum, PL directly measures the bandgap energy of semiconductors, which is essential for applications such as solar cells and LEDs [42].

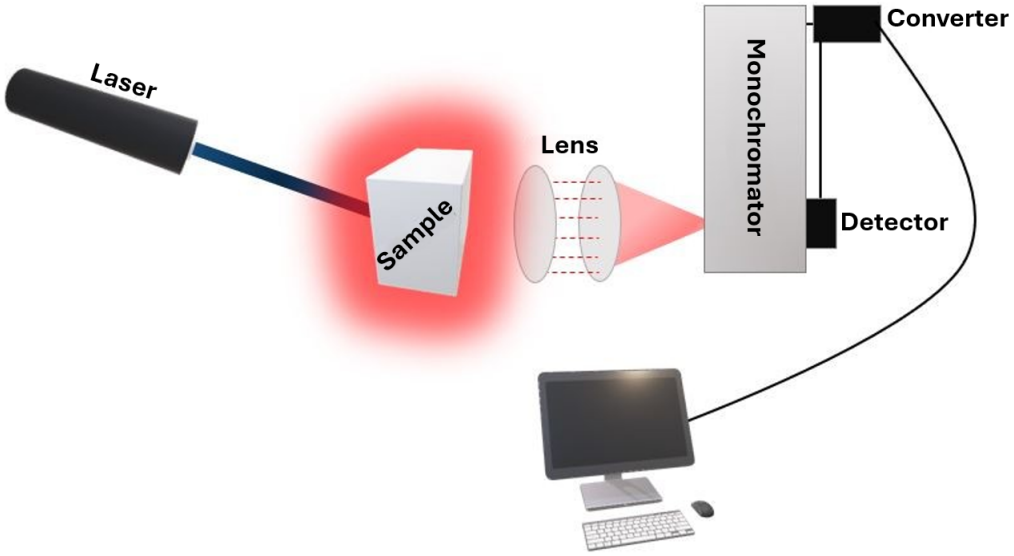

Figura 3.2: Schematic diagram of the Photoluminescence (PL) measurement setup. A laser excites the sample, causing it to emit light, which is collected by a series of lenses and directed into a monochromator. The monochromator separates the light into its constituent wavelengths, which are then detected and analyzed. The signal is sent to a computer for processing, allowing for detailed characterization of the material's optical properties. Although not shown in the diagram, the laser beam is focused onto the sample using a lens system to ensure efficient excitation. The converter represents the detection module responsible for converting the optical signal into an electrical one, allowing the emission spectrum to be displayed and analyzed on the computer.

- **Environmental Flexibility**: PL can be performed at various temperatures and in controlled atmospheres, making it ideal for studying temperature-dependent optical properties [46].

The typical PL setup consists of the following components (see also Figure 3.2):

- **Excitation Source**: A laser provides photons of energy greater than the material's bandgap [47].
- **Sample Stage**: The sample is often placed in a controlled environment to allow for variable temperature studies [48].
- **Detection System**: The emitted light is captured and analyzed by a spectrometer [49].

For time-resolved PL (TRPL) measurements, pulsed lasers are used to probe exciton recombination dynamics, providing the characteristic lifetimes associated with radiative and non-radiative decay channels [41]. In this thesis, both steady-state PL and TRPL are essential for investigating the optical behavior of $CsPb(Br_{1-x}Cl_x)_3$

nanowires. The bandgap tunability, achieved through anion exchange, shifts the PL emission peak, confirming the successful bandgap engineering of the perovskite nanowires [45].

Overall, PL is indispensable in the development of optoelectronic devices, providing critical insights for the design of solar cells, LEDs, and nanophotonic systems [41, 42].

- **Solar Cells**: PL helps optimize the absorber layers in solar cells by providing detailed information on defect states and bandgaps [50].
- **LEDs**: PL is used to study emission efficiency and wavelength tuning, particularly in perovskite-based LEDs [51].
- **Nanophotonics**: PL assists in studying phonon-polariton interactions, which is essential for advanced nanophotonic applications [41, 46].

3.3 Time-Correlated Single Photon Counting (TCSPC)

Time-Correlated Single Photon Counting (TCSPC) is a sensitive and widely-used technique for measuring the temporal dynamics of photon-emitting processes, such as photoluminescence and fluorescence. TCSPC provides critical insights into exciton dynamics, carrier lifetimes, and recombination processes in materials, making it invaluable for optoelectronic applications [52, 53].

The principle behind TCSPC involves detecting single photons and accurately measuring the time delay between the excitation pulse and the subsequent photon emission. In this technique, a pulsed laser excites the sample, and the emitted photons are captured by a highly sensitive single-photon detector, such as a photomultiplier tube or avalanche photodiode. The time of arrival of each photon is recorded relative to the excitation pulse, creating a histogram that represents the photoluminescence decay, providing a direct measurement of the excited state's lifetime [52]. A schematic illustration of a typical TCSPC setup is shown in Figure 3.3, which highlights the main components of the technique and how the detection process is performed in practice.

The key components in a TCSPC setup include:

- **Pulsed Laser Source**: Provides excitation pulses at regular intervals, typically on the order of picoseconds or nanoseconds.
- **Single Photon Detector**: Detects the emitted photons with high time resolution.

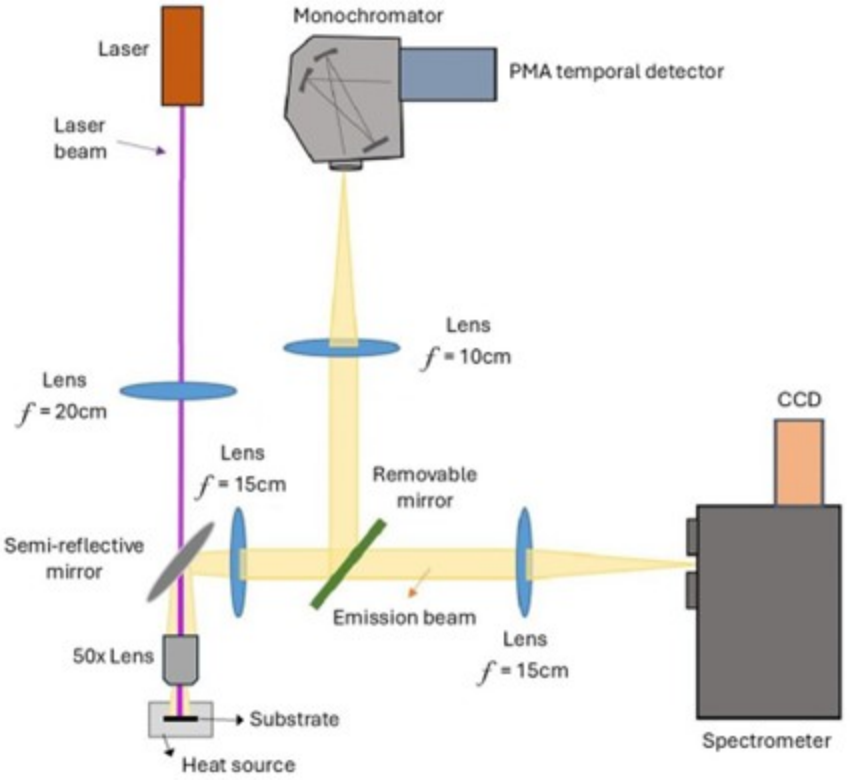

Figura 3.3: Schematic diagram of a typical TCSPC setup. A pulsed laser excites the sample, and the emitted photons are collected and directed through a monochromator before being detected by a photomultiplier tube or equivalent single-photon detector. Timing electronics register the delay between excitation and detection events, producing a histogram of photon arrival times that can be analyzed to extract photoluminescence lifetimes.

- **Timing Electronics**: Records the time interval between the excitation pulse and photon detection.

The recorded data are processed to create a histogram of photon arrival times, which reveals the sample's decay characteristics. By fitting the decay curve to an exponential model, the photoluminescence lifetime can be extracted, providing valuable insights into the material's recombination dynamics [54].

A typical TCSPC setup includes the following components:

- A pulsed laser to excite the sample.
- A monochromator and a photomultiplier tube (PMA) or another time-resolved photon detector to measure the emitted light.
- Additional optics to focus and manipulate both the excitation and emission beams.

- A spectrometer for spectral analysis of the emitted light.

In this setup, the laser beam is directed at the sample, and the emitted photons are collected and directed through a monochromator before being detected by a photomultiplier tube. The time-correlated photon counting system records the arrival times of the photons, allowing for a detailed analysis of the photoluminescence decay [52].

Time-Resolved Photoluminescence (TRPL) is one of the main applications of the Time-Correlated Single Photon Counting (TCSPC) technique. In this method, the temporal evolution of the photoluminescence emission is measured after pulsed excitation. While TRPL refers to the optical measurement that tracks how the luminescence intensity decays over time, TCSPC denotes the instrumental technique used to achieve the required temporal resolution by recording the arrival time of individual photons relative to the excitation pulse. This combination enables the reconstruction of PL decay curves with sub-nanosecond precision. In our experimental setup, the overall temporal resolution of the TCSPC system is approximately 100 ps. TRPL measurements provide insights into:

- **Exciton Dynamics**: The lifetime of excitons before recombination.
- **Carrier Lifetimes**: The recombination lifetimes of charge carriers in a material.
- **Non-Radiative and Radiative Recombination**: TRPL helps distinguish between radiative recombination (where photons are emitted) and non-radiative recombination (where energy is dissipated as heat).

TCSPC and TRPL are complementary, with TCSPC used for time-resolved measurements beyond photoluminescence, such as fluorescence lifetimes and quantum optical experiments [54].

In this thesis, TCSPC is used to analyze the PL decay in $CsPb(Br_{1-x}Cl_x)_3$ nanowires. By measuring the decay dynamics, the technique helps to determine carrier lifetimes and recombination processes, providing key insights into the material's optoelectronic properties for use in applications such as solar cells and LEDs. Furthermore, TCSPC is instrumental in studying heterojunction effects within the nanowires, where the substitution of bromine with chlorine alters the electronic structure and exciton behavior [55].

3.4 Synthesis

The synthesis of nanostructures and hybrid systems is a crucial aspect of material science and nanotechnology, particularly when investigating advanced optoe-

lectronic properties. In this thesis, two distinct synthesis processes are explored to create systems with unique photonic and phononic characteristics. First, we present the synthesis of $CsPb(Br_{1-x}Cl_x)_3$ nanowires (NWs), which are fabricated using a template-assisted growth method and further modified via an anion exchange process to fine-tune their optical properties. These NWs exhibit highly tunable photoluminescence, making them ideal candidates for applications in solar cells and light-emitting devices [56, 57].

3.4.1 Synthesis of $CsPb(Br_{1-x}Cl_x)_3$ Nanowires (NWs)

The synthesis of perovskite nanowires (NWs) is a critical step in ensuring high-quality nanostructures with well-defined optoelectronic properties. In this study, $CsPb(Br_{1-x}Cl_x)_3$ NWs were grown using a method based on epitaxial deposition in porous anodic alumina templates [58]. The growth process involved careful control over temperature, pressure, and precursor concentrations to ensure uniformity and minimize defect formation in the NWs [56].

Synthesis of $CsPbBr_3$ Nanowires

The first stage of the process involved the synthesis of pure $CsPbBr_3$ nanowires using anodic alumina (AAO) templates. These templates provide the necessary confinement for the NW growth, ensuring that the structures form with high aspect ratios and uniform diameters. The key steps in this synthesis are outlined as follows:

- **Preparation of the AAO Template**: The template was prepared by anodizing aluminum foils in an acidic electrolyte, creating a porous structure with cylindrical pores. These pores act as molds for the nanowire growth, controlling their diameter and length [58].

- **Infiltration of Precursors**: After the template preparation, a solution containing the perovskite precursors (CsBr and $PbBr_2$) was infiltrated into the AAO template using a capillary effect or an external pressure gradient to ensure the complete filling of the pores [59, 60].

- **Thermal Treatment**: The template containing the precursors was subjected to a thermal annealing process at temperatures around 70°C. This thermal treatment promotes the crystallization of the perovskite phase while avoiding degradation or excessive growth beyond the pore walls [56].

- **Nanowire Liberation and Transfer**: After the crystallization process, the $CsPbBr_3$ nanowires were carefully transferred from the alumina template onto

silicon nitride (Si_3N_4) substrates using a mechanical probe. This method allows for precise handling and avoids the need for dissolving the template, preserving the integrity of the nanowires and ensuring a clean transfer for further characterization [60].

- **Structural Characterization**: To confirm the successful synthesis, techniques such as scanning electron microscopy (SEM) and atomic force microscopy (AFM) were used to examine the morphology and dimensions of the NWs. Additionally, X-ray diffraction (XRD) was employed to verify the crystallinity and phase purity of the $CsPbBr_3$ [56].

Figure 3.4 shows a schematic representation of the NW growth process within the AAO template, as well as the final liberated nanowires on a substrate.

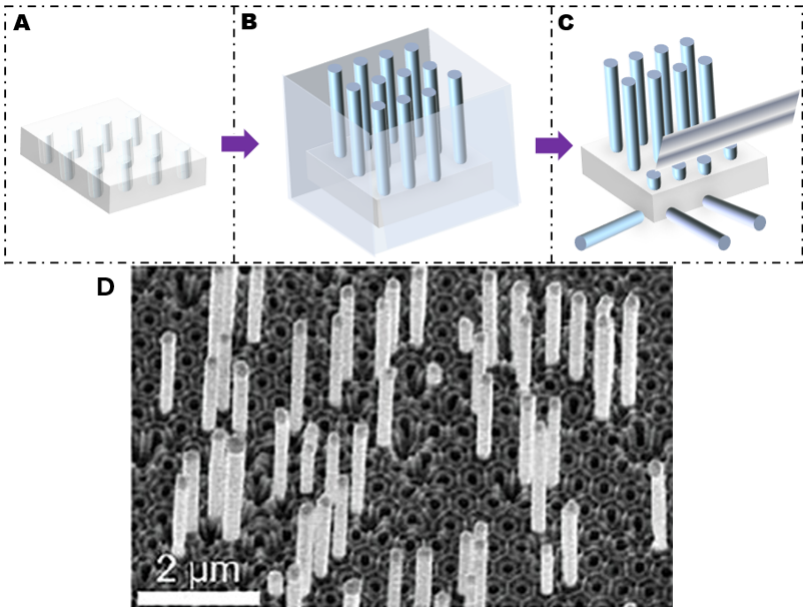

Figura 3.4: Schematic illustration of the synthesis process for $CsPbBr_3$ nanowires. (A) Represents the porous anodic alumina (AAO) template used to confine the growth of the nanowires. (B) Shows the epitaxial growth of the nanowires extending from the template, with the wires protruding outward. (C) Illustrates the transfer process where a probe is used to carefully extract the nanowires and deposit them onto a substrate for further characterization. (D) Scanning electron microscopy (SEM) image showing $CsPbBr_3$ nanowires emerging from the AAO template pores after the growth process, confirming the successful formation and alignment of the nanowires within the template structure.

Anion Exchange: Incorporation of Chlorine

The second stage of the process involves the controlled exchange of bromine (Br) with chlorine (Cl) in the $CsPbBr_3$ nanowires to form heterostructured $CsPb(Br_{1-x}Cl_x)_3$

nanowires. This anion exchange is performed in a gaseous atmosphere and requires careful control to avoid degradation of the perovskite structure [57]. The substitution of Br with Cl is crucial for tuning the optical properties of the nanowires, particularly for adjusting the bandgap and emission wavelength [56, 61].

- **Partial Anion Exchange**: The anion exchange process was performed to create $CsPb(Br_{1-x}Cl_x)_3$ nanowires with a well-defined heterojunction. Initially, $CsPbBr_3$ NWs were transferred to a sapphire carrier wafer using a mechanical probe. These wafers were then loaded into a Plasma-Therm Apex RIE tool, where the gas-phase anion exchange took place.

  The NWs were exposed to an Ar/Cl_2 atmosphere held at a total pressure of 1.33×10^{-4} bar, with a Cl_2 partial pressure of 3.33×10^{-5} bar. The exchange occurred via a diffusion mechanism, where Cl atoms progressively replaced Br atoms in the perovskite lattice while maintaining the crystal structure intact.

  $CsPb(Br_{1-x}Cl_x)_3$ heterojunction NWs were fabricated using an electron beam lithography process. A polymethyl methacrylate (PMMA) layer was applied to partially cover selected NWs. This process exposed only half of each NW to the Cl_2 atmosphere, preventing the other half from undergoing the exchange reaction. The result was the formation of axially stepped heterostructures with a sharp compositional gradient, as shown in Figure 3.5. The portion of the NW exposed to Cl_2 experienced a gradual replacement of Br with Cl, forming a Cl-rich region, while the PMMA-covered half remained Br-rich [61].

- **Control of Exchange Degree**: The degree of substitution (i.e., the value of x in $CsPb(Br_{1-x}Cl_x)_3$) is controlled by adjusting the temperature, pressure, and exposure time during the chlorine gas treatment. Higher Cl concentrations (x) shift the photoluminescence (PL) emission from green to blue, offering tunability for optoelectronic applications [57].

- **Characterization**: After the anion exchange, the nanowires were characterized to confirm the successful incorporation of Cl. Photoluminescence (PL) measurements were performed to observe shifts in the emission peak, and X-ray diffraction (XRD) was used to detect any structural changes. Time-correlated single-photon counting (TCSPC) was employed to examine the effect of the anion exchange on exciton dynamics [57, 62].

Figure 3.5 shows a schematic of the anion exchange process and the resulting heterostructured nanowires, highlighting the gradual transition from bromine-rich to chlorine-rich regions.

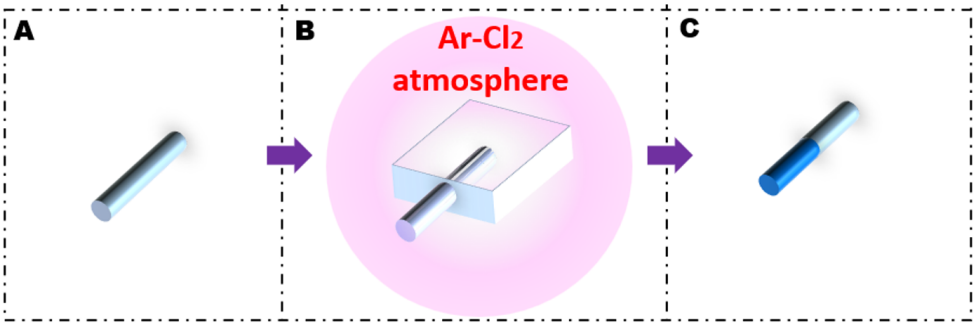

Figura 3.5: Illustration of the partial anion exchange process from $CsPbBr_3$ to $CsPb(Br_{1-x}Cl_x)_3$ nanowires. (A) Shows the $CsPbBr_3$ NW transferred to a substrate. (B) Depicts the NW exposed to an Ar-Cl_2 atmosphere, with half of the NW coated with PMMA to prevent exchange in that region. The exposed half undergoes anion exchange where Br atoms are gradually replaced by Cl atoms. (C) The final heterostructured nanowire is shown, where the Cl-rich region is represented in blue and the Br-rich region in green, demonstrating the successful formation of the heterojunction.

To further verify the successful anion exchange and its effects on the optical properties, photoluminescence (PL) measurements were carried out along the length of the nanowires. As shown in Figure 3.6, the photoluminescence (PL) spectra of $CsPbBr_3$, $CsPbCl_3$ nanowires, and their heterojunctions reveal distinct emission peaks corresponding to the Br-rich and Cl-rich regions. The $CsPbBr_3$ nanowires exhibit a green emission, while the $CsPbCl_3$ nanowires display a blue-shifted emission, with the heterojunction nanowires showing intermediate properties due to the anion exchange process [58,62]. In addition, a noticeable broadening of the emission peak is observed for the heterojunction nanowires, which can be attributed to the spatial overlap of emissions from Br- and Cl-rich regions and to photon recycling effects that enhance reabsorption and re-emission processes within the structure.

The PL measurements clearly demonstrate the compositional heterogeneity of the nanowires, with different PL peaks corresponding to different degrees of anion substitution. This tunability in emission properties is critical for optoelectronic applications such as multi-color LEDs and wavelength-tunable lasers.

The incorporation of chlorine into $CsPbBr_3$ nanowires significantly alters their optoelectronic properties. Specifically, the bandgap of the material widens as Br is replaced by Cl, leading to a blue shift in the photoluminescence emission. This tunability is crucial for applications in light-emitting diodes (LEDs) and other optoelectronic devices, where precise control over the emission wavelength is necessary.

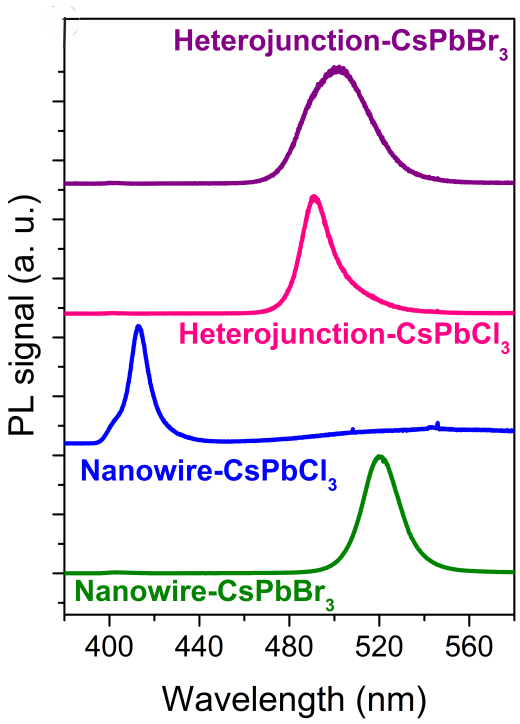

Figura 3.6: Photoluminescence (PL) spectra of $CsPbBr_3$ and $CsPbCl_3$ nanowires and heterojunctions. The green and blue curves represent PL emissions from pure $CsPbBr_3$ and $CsPbCl_3$ nanowires, respectively, while the purple and pink curves show the emissions from $CsPbBr_3/CsPbCl_3$ heterojunction nanowires. The shifts in emission peaks between the nanowires and heterojunctions demonstrate the effect of the anion exchange process on optical properties. The measurements were performed using a focused 357 nm excitation laser with a power of 0.1 mW; for heterojunction nanowires, the laser was focused separately on each extremity to probe the Br-rich and Cl-rich regions.

Chapter 4

Results and Discussion

This chapter presents and discusses the key results obtained from the investigation of $CsPb(Br_{1-x}Cl_x)_3$ metal halide perovskite nanowires (NWs). The study focused on how controlled anion exchange, from bromine to chlorine within the perovskite lattice, influences the morphological, optical, and excitonic properties of the nanowires. By fabricating heterostructured NWs with Br-rich and Cl-rich segments, it was possible to explore bandgap tunability, spatially resolved photoluminescence, and the emergence of interfacial phenomena.

Special attention is given to the role of strain, ferroelasticity, and flexoelectricity in modulating the optoelectronic response of the nanowires. These structural effects are shown to influence exciton recombination dynamics, photoluminescence peak shifts, and lifetime enhancements near crystallographic phase transitions. The results not only provide fundamental insight into the excitonic behavior of halide perovskite nanostructures, but also establish design principles for exploiting strain engineering in next-generation optoelectronic devices.

In the following sections, the synthesis process, experimental techniques, and detailed analysis of the morphological and optical properties of the nanowires are presented. Each subsection emphasizes the correlation between structural dynamics and optoelectronic response, building a comprehensive picture of how halide composition and ferroelastic effects govern exciton dynamics in $CsPb(Br_{1-x}Cl_x)_3$ nanowires.

4.1 Detailed Results and Analysis of $CsPb(Br_{1-x}Cl_x)_3$ Nanowires

This section presents a comprehensive analysis of the experimental work conducted on $CsPb(Br_{1-x}Cl_x)_3$ nanowires (NWs), focusing on their synthesis, **optical** properties, and the results obtained through photoluminescence (PL) and time-resolved photoluminescence (TCSPC) measurements. Furthermore, we delve into the implications of the observed flexoelectric effect in these nanostructures, evaluating its potential role in the modulation of their optical behavior and its importance in advancing perovskite-based devices.

4.1.1 Morphological Characterization

Atomic force microscopy (AFM) was employed to investigate the morphology of the $CsPbBr_3$ and $CsPb(Br_{1-x}Cl_x)_3$ nanowires, confirming a high degree of uniformity in both pristine and exchanged compositions. Representative AFM images are shown in Figures 1,2 and 3 (see Appendix 5). The nanowires exhibit average lengths of 3–5 μm and diameters of approximately 250 nm, consistent with the pore size of the anodized aluminum oxide (AAO) template used for synthesis.

The AFM height profiles confirm that the diameter remains constant along the nanowire axis, reflecting the success of the template-assisted growth method. In the case of $CsPbCl_3$ nanowires obtained through complete anion exchange (Figure 2, see Appendix 5), the morphology remains smooth and uniform, demonstrating that the substitution of Br by Cl does not degrade the structural integrity of the nanowires.

In addition, AFM images of heterojunction nanowires (Figure 3, Appendix 5) reveal no visible topographic discontinuity between the Br-rich and Cl-rich segments. This indicates that the compositional gradient established during anion exchange does not introduce morphological defects at the interface. Occasionally, individual nanowires exhibited mechanical fragility, with breakage observed during AFM scanning. This effect is attributed to local strain heterogeneities, consistent with the ferroelastic reorganization processes discussed in Section 4.1.4.

Altogether, the AFM analysis confirms that the nanowires are structurally uniform, morphologically stable after halide substitution, and suitable for systematic optical characterization.

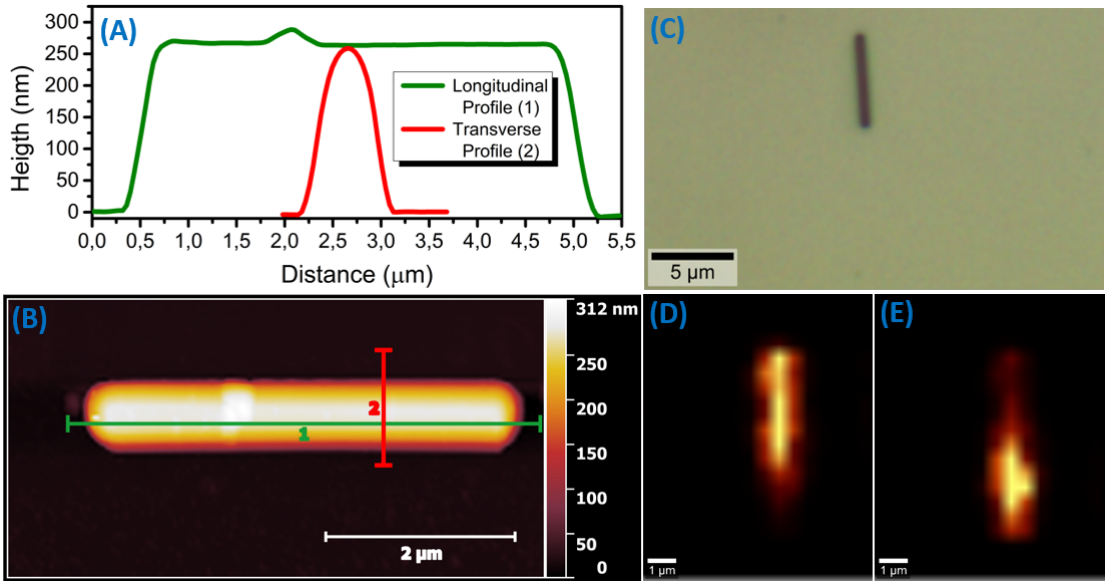

Figura 4.1: (A) Profile of the NW obtained using Gwyddion software from AFM measurements. (B) AFM topographic image of a $CsPb(Br_{1-x}Cl_x)_3$ heterojunction NW. (C) Optical microscopy image of the heterojunction NW alongside its photoluminescence (PL) response when excited at $\lambda_{exc} = 457$ nm. (D) and (E) PL emission maps centered at 507 nm and 523 nm, respectively, obtained by integrating the emission intensity over a 10 nm spectral range around each PL peak center.

4.1.2 Photoluminescence (PL) Characterization

Steady-state photoluminescence (PL) measurements were conducted to investigate the optical properties of the $CsPb(Br_{1-x}Cl_x)_3$ NWs. The emission spectra clearly demonstrate the gradual shift in emission peak position from green (Br-rich) to blue (Cl-rich), confirming the successful creation of a heterojunction within the NW. Figure 3.6 shows the PL curves for the fully exchanged NW (Cl-rich) and the pristine $CsPbBr_3$ NW, alongside the heterostructured NW. The spatially resolved PL map (Figures 4.1(D) and 4.1(E)) shows a gradual transition in the emission peak along the NW, further confirming the Br-to-Cl compositional gradient.

The μ-PL measurements were performed using a WITec alpha300 RA spectrometer equipped with a 50× objective lens. Excitation was provided by a 457 nm continuous-wave laser, delivering 0.5 mW of power and focused to a ∼0.3 μm spot size. The nanowire was scanned along its axis with 0.15 μm step resolution, enabling high-resolution luminescence mapping. This spatial resolution was crucial for resolving the compositional gradient along the heterostructure.

Spatially resolved PL maps were also acquired at fixed detection wavelengths. Figures 4.1(D) and 4.1(E) illustrate the emission distribution centered at 507 nm (Cl-rich) and 523 nm (Br-rich), each with a 2 nm bandwidth. These maps clearly

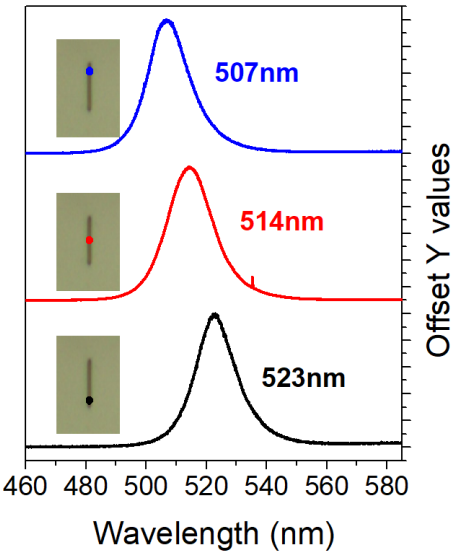

Figura 4.2: Photoluminescence spectra measured at three distinct positions along the length of a $CsPb(Br_{1-x}Cl_x)_3$ heterojunction NW. The black line corresponds to the Br-rich end of the NW (523 nm emission), the red line represents the central region (514 nm), and the blue line corresponds to the Cl-rich end (507 nm). Inset: Optical microscope images of the NW at each position where the micro-PL measurements were performed.

highlight the contrast between the two ends of the heterojunction and confirm that the emission gradient is not abrupt but continuous, consistent with partial halide substitution. The presence of the intermediate 514 nm peak at the junction further demonstrates the gradual modulation of the bandgap along the nanowire axis.

Additionally, spatially resolved micro-PL measurements were performed along the length of the NW, exciting with a $\lambda_{exc} = 457$ nm laser. Figure 4.2 illustrates the emission spectra obtained at three distinct positions: (i) at the Br-rich end, (ii) in the middle of the NW, and (iii) at the Cl-rich end. The emission peak corresponding to $CsPbBr_3$ is around 523 nm (black line), and as we move towards the Cl-rich region, a blue shift is observed, with the emission peak transitioning to 507 nm (blue line) at the Cl-rich end. This blue shift indicates the successful incorporation of chlorine along the NW and the formation of a heterojunction. The inset images in Figure 4.2 show the optical microscope images of the NW at each position where the micro-PL spectra were acquired.

The 523 nm peak measured at the Br-rich end corresponds to the emission of pure $CsPbBr_3$, whereas the 507 nm peak at the opposite end is characteristic of fully substituted $CsPbCl_3$ domains. The intermediate 514 nm emission from the center region demonstrates that the anion exchange did not occur as a sharp interface, but rather as a gradual compositional gradient along the nanowire. This observa-

tion is in agreement with reports on halide exchange in perovskite nanostructures, where incomplete substitution at the interface often results in intermediate bandgap regions.

The blue shift observed is a clear indication of the successful gradient formation along the NW, transitioning from a Br-rich to a Cl-rich composition. The $CsPbBr_3$ peak initially at 523 nm progressively shifts towards 507 nm at the Cl-rich end, illustrating the optical bandgap change due to the compositional variation.

It is also worth noting that the spectral evolution observed across the heterostructure indicates not only a compositional gradient but also potential carrier migration and photon recycling effects. Even when excitation occurs in the Cl-rich region, part of the emission can be detected with characteristics of the Br-rich side, suggesting that reabsorption and re-emission processes may couple the two halves of the nanowire. Such behavior highlights the extended mean free path of charge carriers in these single-crystal perovskite NWs, which could be advantageous for light-harvesting or light-guiding applications. Furthermore, the ability to engineer bandgap gradients within a single NW paves the way for designing nanoscale heterostructures with tailored optoelectronic functionalities, such as directional emission and enhanced exciton separation.

4.1.3 Exciton Dynamics and Lifetime Measurements

Time-resolved photoluminescence (TRPL) was measured via time-correlated single photon counting (TCSPC) to analyze the exciton lifetimes within the NW heterojunction. Figure 4.3 presents the time decay curves for different temperatures during the heating process, showing a notable increase in exciton lifetime near the phase transition temperature of 305 K. This behavior is consistent with the orthorhombic to tetragonal phase transition of the $CsPbCl_3$ region. The exciton dynamics are influenced by changes in the crystalline structure, with longer lifetimes observed during the phase transition, as the recombination process is slowed down by modifications of the electronic band structure.

The bi-exponential decay model applied to the time-resolved data (Figure 4.4) reveals two distinct exciton recombination processes, labeled as P1 and P2. The slower recombination process (P1), attributed to radiative excitonic recombination, remained relatively stable across the studied temperature range, with an average lifetime of approximately 2.6 ns. In contrast, the faster component (P2), associated with non-radiative channels, exhibited significant variation with temperature. Away from the phase transition, P2 showed average lifetimes of $\sim$0.7 ns, but at $\sim$305 K a remarkable increase was detected, reaching 2.3 ns in the Cl-rich region and 1.4 ns in

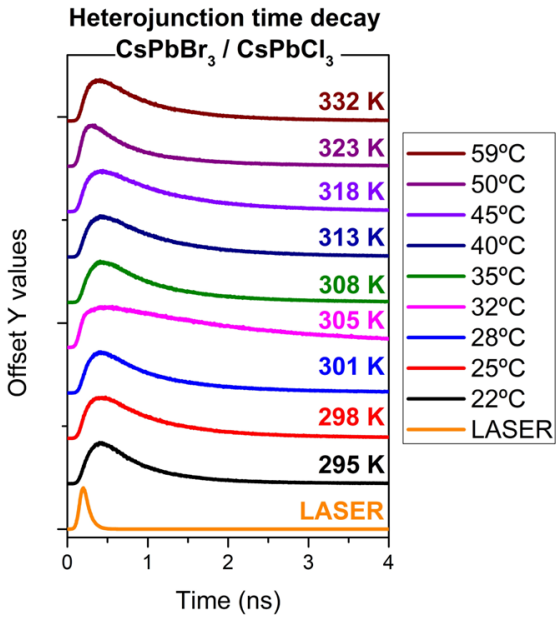

Figura 4.3: Time-resolved photoluminescence (TRPL) decay curves of $CsPbBr_3/CsPbCl_3$ heterojunction nanowires measured at different temperatures ranging from 295 K to 332 K. A gradual increase in exciton lifetime is observed near the phase transition temperature of 305 K, indicating the influence of the orthorhombic to tetragonal phase transition in the $CsPbCl_3$ region. The decay traces were collected via time-correlated single photon counting (TCSPC), with each curve representing a distinct temperature during the heating process.

the Br-rich region. This corresponds to nearly a threefold enhancement compared to the baseline values, demonstrating that the suppression of non-radiative recombination channels is the primary driver of the increased exciton lifetime during the structural phase transition.

The complete set of parameters extracted from the bi-exponential fits is summarized in Table 4.5. These values provide a quantitative confirmation of the trends shown in Figures 4.3 and 4.4: while the slower decay component (P1), associated with the dominant radiative recombination process, remains nearly constant across the studied temperature range, the faster component (P2) exhibits a pronounced increase in lifetime at the transition temperature. Although both components are radiative in origin, the temperature dependence of P2 suggests a modulation of non-radiative pathways that transiently suppress non-radiative losses during the structural phase transition. The amplitude ratios (A_1/A_2) indicate that radiative recombination dominates under most conditions, but the balance shifts during the phase transition, when structural rearrangements of ferroelastic domains significantly alter the recombination dynamics.

The simultaneous observation of lifetime changes in both halves of the hetero-

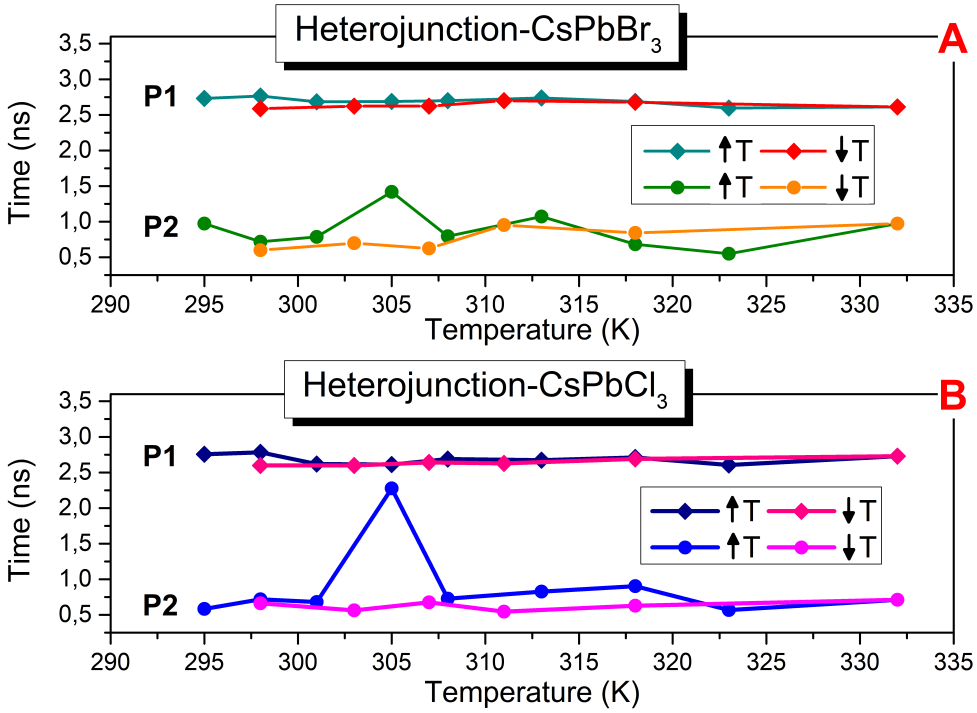

Figura 4.4: Lifetime of the two luminescent processes (P1 and P2) present in the $CsPb(Br_{1-x}Cl_x)_3$ heterojunction NW for different temperatures during heating. Measurements in (A) were performed in the Br-rich half, while (B) shows the Cl-rich half.

junction reinforces the idea that charge carriers and reabsorbed photons can diffuse across the interface [63], effectively coupling the Br-rich and Cl-rich regions. This is consistent with the photon recycling mechanism already reported in perovskite nanostructures, whereby emitted photons are reabsorbed and re-emitted in adjacent regions, extending the effective exciton diffusion length.

In addition, the hysteresis observed in the temperature-dependent PL peak positions is also reflected in the TRPL measurements. The enhancement of P2 lifetimes at the transition temperature does not immediately revert upon cooling, revealing a memory effect associated with ferroelastic domain reorganization. This finding suggests that strain heterogeneities play an active role in the modulation of recombination dynamics during thermal cycling.

Finally, multiple heating and cooling cycles performed on different heterostructured NWs confirmed the reproducibility of this behavior. The consistent enhancement of the faster decay component (P2) near the Cl-rich transition temperature, together with the stability of the slower component (P1), demonstrates that this phenomenon is intrinsic to the system rather than sample-specific. Although both components

Heterojunction-$CsPbBr_3$						Heterojunction-$CsPbCl_3$					
Temperature (K)	P1 (ns)	A1	P2 (ns)	A2	A1/A2	Temperature (K)	P1 (ns)	A1	P2 (ns)	A2	A1/A2
295	2.73	0.15	0.97	0.54	0.28	295	2.76	0.03	0.58	0.64	0.04
298	2.77	0.04	0.72	1.05	0.04	298	2.78	0.07	0.72	0.55	0.13
301	2.68	0.06	0.79	0.95	0.06	301	2.62	0.09	0.68	0.38	0.24
305	2.69	0.11	1.42	0.59	0.18	305	2.61	0.00	2.28	1.35	0.00
308	2.70	0.03	0.80	1.10	0.02	308	2.69	0.05	0.73	0.73	0.07
313	2.74	0.01	1.07	1.03	0.01	313	2.67	0.05	0.83	0.99	0.05
318	2.69	0.05	0.68	1.31	0.04	318	2.71	0.06	0.90	0.95	0.06
323	2.60	0.07	0.55	0.77	0.09	323	2.60	0.08	0.57	0.63	0.13
332	2.61	0.14	0.97	0.55	0.25	332	2.73	0.03	0.71	1.12	0.02
318	2.68	0.07	0.84	0.63	0.10	318	2.69	0.05	0.63	0.54	0.09
311	2.70	0.04	0.95	0.75	0.05	311	2.63	0.04	0.55	1.11	0.03
307	2.62	0.05	0.62	0.83	0.06	307	2.64	0.06	0.68	0.96	0.07
303	2.62	0.03	0.70	0.64	0.05	303	2.60	0.03	0.56	0.55	0.06
298	2.59	0.03	0.60	1.21	0.02	298	2.60	0.04	0.66	0.54	0.07
Average	2.67	0.06	0.83	0.85	0.09	Average	2.67	0.05	0.79	0.79	0.08

Figura 4.5: Bi-exponential decay fitting parameters extracted from TRPL measurements of $CsPb(Br_{1-x}Cl_x)_3$ heterojunction nanowires.
P1 corresponds to the radiative excitonic recombination channel and P2 to the non-radiative channel. The values of τ_1 and τ_2 represent the characteristic lifetimes of each channel, while the ratio A_1/A_2 indicates the relative contribution of radiative to non-radiative processes.

are radiative, the transient increase of P2 reflects a temporary suppression of non-radiative losses during the structural phase transition. Furthermore, during thermal cycling, the PL peak positions exhibit hysteresis — they do not fully return to their initial values upon cooling — yet subsequent measurements performed after the system has stabilized show that the emission peaks recover their original positions. These results highlight the robustness of the lifetime modulation induced by crystallographic phase transitions and underscore the role of ferroelastic and flexoelectric effects in governing exciton recombination in low-dimensional perovskites.

4.1.4 Ferroelasticity and Flexoelectricity

The observation of ferroelastic domains in the $CsPb(Br_{1-x}Cl_x)_3$ NWs provides key insights into the structural changes induced by the phase transition [25], rather than by the incorporation of chlorine alone. These domains appear as the material undergoes a crystallographic phase transition at approximately 305 K, and the NWs slowly accommodate the strain induced by this transition. As the Cl-rich region of the NW transforms from the orthorhombic to the tetragonal phase, strain accumulates along the nanowire, which in turn influences the electronic band structure and modulates the optoelectronic response. Such ferroelastic domain formation has been directly imaged in $CsPbBr_3$ nanowires using nanofocused X-ray diffraction and in situ heating experiments, confirming that strain-induced twinning and reordering are intrinsic to these systems.

Figure 4.6 illustrates how strain gradients along the NW, generated by phase

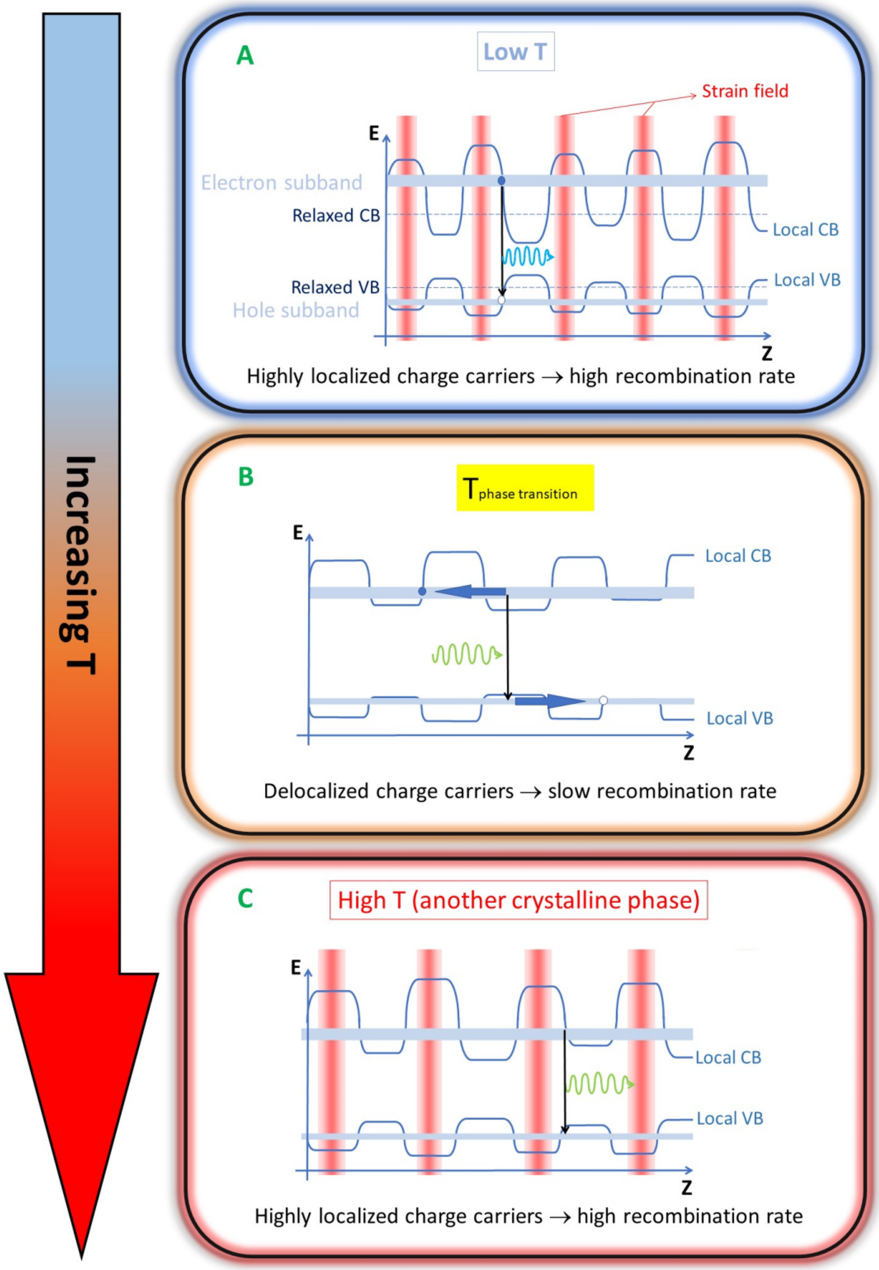

Figura 4.6: Schematic evolution of the electronic band structure as a function of the position along the NW growth direction. The temperature increases from the top to the bottom panel. Precisely at the phase transition, the charge carriers have the largest mean free path along the growth axis. The boxes show the electronic band structure for (A) low temperature, (B) at the temperature in which the probable phase transition occurs and (C) a higher temperature.

transitions, can modulate the electronic band structure and affect charge carrier dy-

namics. The presence of ferroelastic domains introduces local strain gradients, which in turn induce flexoelectric polarization within the NWs. This flexoelectric effect is particularly enhanced at the domain walls, where strain gradients are highest, effectively forming a periodic or aperiodic array of polarization regions. In this sense, the NWs can be modeled as *disordered strain superlattices*, in which alternating strain states generate local variations in band edges. Such disordered superlattices are known to promote Anderson localization of carriers, but in the case of perovskite NWs, they instead lead to a transient increase in the mean free path of charge carriers when the strain pattern is reorganized at the phase transition.

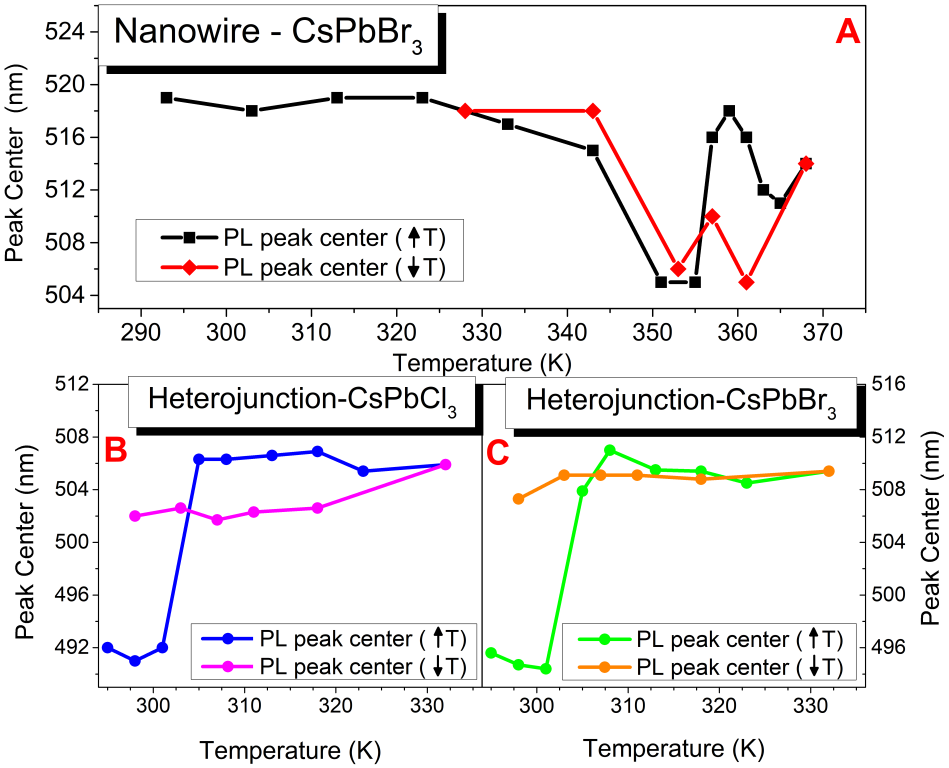

Figura 4.7: Curves of the PL peak center of the luminescence as a function of temperature. In (A) we show measurements for the $CsPbBr_3$ NW, while results for the heterojunction NW are shown in (B) for the Cl-rich half, and in (C) for the Br-rich half. Peak center error bars are smaller than point sized for all graphs.

Additionally, the hysteresis observed in the PL peak shift during thermal cycling (Figure 4.7) suggests that the reordering of ferroelastic domains occurs close to the phase transition temperature. This reorganization not only modifies the strain distribution but also reduces the overall flexoelectric polarization between adjacent domains, since the strain gradient is partially smeared out. As a consequence, the polarization dynamics are altered in such a way that the charge carrier mean free path is increased, effectively reducing the recombination probability. This microsco-

pic mechanism provides a consistent explanation for the enhanced exciton lifetimes observed near the phase transition, as reported in Section 4.1.3. The combination of ferroelastic domain dynamics and flexoelectric modulation thus emerges as a central factor controlling the optical response of $CsPb(Br_{1-x}Cl_x)_3$ nanowires.

Finally, it is important to emphasize that these effects are not artifacts of the heterojunction configuration but intrinsic to the perovskite lattice itself. Similar ferroelastic domain switching and flexoelectric responses have been reported in $CsPbBr_3$ and other halide perovskite nanostructures, indicating that strain-driven polarization fields are a general phenomenon in this material family [35, 36]. Understanding the interplay between ferroelasticity, flexoelectricity, and phase transitions is therefore crucial for exploiting perovskite nanowires in optoelectronic applications, particularly in environments where devices are expected to operate slightly above room temperature.

4.1.5 Photoluminescence Peak Shifts and Strain Effects

The strain-induced modulation of the electronic band structure also plays a decisive role in the observed shifts of the PL peak position. As the nanowires undergo structural phase transitions, the ferroelastic domains reorganize, leading to local strain gradients that alter the band edges. This effect is manifested as a shift of the PL peak towards shorter wavelengths (blue shift) near the onset of the orthorhombic-to-tetragonal transition in the Cl-rich regions at $\sim$305 K, followed by a red shift as the temperature increases further. A similar but higher-temperature shift is observed in the Br-rich domains, with the critical point occurring near $\sim$361 K, consistent with the known transition temperature of $CsPbBr_3$.

Figure 4.7 clearly shows this behavior: the Cl-rich half exhibits a distinct discontinuity in peak position at 305 K, while the Br-rich half follows the Cl-induced transition despite being below its own critical temperature. This cross-response is explained by the coupling between regions through carrier diffusion and photon recycling. The strain fields generated during the transition extend beyond the local domain boundaries, effectively influencing the optoelectronic response of the entire heterojunction.

Another important feature is the hysteresis observed during thermal cycling: upon cooling, the PL peak does not return precisely to its initial position, but instead remains slightly shifted. This indicates that the ferroelastic domains do not immediately recover their original configuration, leaving residual strain in the lattice. Such hysteresis is a fingerprint of ferroelastic reordering and is consistent with the memory effects described in Section 4.1.4. The persistence of strain after

thermal cycling highlights the metastable character of domain configurations in these perovskite nanowires.

Overall, the PL peak shifts observed in $CsPb(Br_{1-x}Cl_x)_3$ nanowires arise from the interplay between ferroelastic strain and structural phase transitions. These effects not only explain the blue- and red-shift cycles in Figure 4.7, but also emphasize the central role of strain in modulating the optoelectronic properties of halide perovskite nanostructures. Strain engineering thus emerges as a powerful approach for tailoring the optical response of perovskite nanowires and for enabling temperature-tunable optoelectronic devices.

Chapter 5

Conclusion

This thesis investigated the excitonic and optoelectronic properties of $CsPb(Br_{1-x}Cl_x)_3$ nanowires with particular emphasis on heterostructured systems obtained through controlled anion exchange. The combined use of AFM, steady-state PL mapping, temperature-dependent spectroscopy, and time-resolved PL provided a comprehensive picture of how structural phase transitions and strain gradients influence exciton dynamics in one-dimensional metal halide perovskites.

The nanowires exhibited excellent morphological uniformity, with lengths of 3–5 μm and diameters of $\sim$250 nm, while retaining their structural integrity even after full or partial anion exchange. Spatially resolved PL confirmed the successful formation of heterojunctions, with emission peaks shifting gradually from 523 nm (Br-rich) to 507 nm (Cl-rich) along the nanowire axis. This bandgap gradient demonstrates the effectiveness of gas-phase halide substitution in engineering compositional and optical heterostructures.

Temperature-dependent measurements revealed critical behaviors associated with phase transitions. In $CsPbCl_3$ segments, a discontinuity at $\sim$305 K was observed, while $CsPbBr_3$ nanowires showed a transition near $\sim$361 K. Remarkably, both regions of heterojunction nanowires responded to the Cl-rich transition, evidencing strong coupling through carrier diffusion and photon recycling. Hysteresis between heating and cooling cycles further indicated the reorganization of ferroelastic domains and the persistence of residual strain.

Time-resolved PL measurements identified two recombination channels: a stable radiative channel (P1, $\sim$2.6 ns) and a non-radiative channel (P2, $\sim$0.7 ns away from transitions). At $\sim$305 K, P2 lifetimes increased up to 2.3 ns in Cl-rich regions and 1.4 ns in Br-rich regions, representing nearly a threefold enhancement. This lifetime extension indicates a transient reduction in non-radiative losses during the structural transition, consistent with the reorganization of ferroelastic domains that

modifies the local recombination dynamics. The reproducibility of these effects across multiple cycles and samples confirms their intrinsic nature.

The interplay between ferroelasticity and flexoelectricity was shown to be a central mechanism underlying these observations. Strain gradients at ferroelastic domain walls generate local polarization fields that modulate the band structure and charge transport. The nanowires can thus be described as disordered strain superlattices, where dynamic reordering of strain patterns at phase transitions enhances the mean free path of carriers and prolongs exciton lifetimes. Photoluminescence peak shifts and hysteresis were directly linked to this strain-polarization coupling, underscoring the importance of structural instabilities in dictating optical response.

In summary, this work demonstrates that crystallographic phase transitions and strain-driven ferroelastic and flexoelectric effects are powerful levers for controlling exciton dynamics in halide perovskite nanowires. The findings provide fundamental insights into how exciton lifetimes can be extended and optical responses tuned in low-dimensional perovskites. These results establish guiding principles for exploiting strain engineering, photon recycling, and ferroelastic reordering in the design of next-generation optoelectronic devices.

Beyond their fundamental implications, these results also provide valuable guidance for real-world applications, particularly in the field of photovoltaics. The ability to tune the bandgap and exciton dynamics via controlled anion exchange improves light absorption across the solar spectrum and contributes to the stability of devices exposed to fluctuating illumination and temperature. Furthermore, the investigation of the flexoelectric effect in $CsPb(Br_{1-x}Cl_x)_3$ nanowires highlights how mechanical stresses — such as those induced by thermal expansion or bending in solar panels — may influence device performance. By addressing these nanoscale interactions, this thesis paves the way for the development of more robust and efficient perovskite-based solar cells and optoelectronic devices, capable of sustaining high performance under realistic operational conditions.

References

[1] Jiazhen He, Xiaoqian Wang, Jinfeng Liu, and Yong Liu. Hot-injection synthesis of cesium lead halide perovskite nanowires with tunable optical properties. *Materials*, 17:2173, 2024.

[2] Hui-Seon Kim. Engineered lattice strain for perovskite solar cells. *Proceedings of International Conference on Hybrid and Organic Photovoltaics*, page 059, 2024.

[3] Xin Li Runda Guo, Weizhuo Zhang et al. Efficient blue cspb(br–cl) nanoparticles enabled by strontium halide and amine halide synergetic optimization. *Journal of Materials Chemistry C*, 10:12345–12354, 2022.

[4] Xiaosheng Tang, Zhiqiang Zu, Haibing Shao, et al. All-inorganic perovskite cspb(br/i) nanorods for optoelectronic application. *Nanoscale*, 8:123–130, 2016.

[5] Ya-Ping Gong, Xiao-Xian Chen, Guo-Zhang Huang, et al. Ferroelasticity, thermochromism, semi-conductivity, and ferromagnetism in a new layered perovskite: (4-fluorophenethylaminium)[cucl]. *Journal of Materials Chemistry C*, 10:5678–5689, 2022.

[6] Dawei Duan, Chuangye Ge, Md. Zahidur Rahaman, Chun-Ho Lin, Yumeng Shi, Haoran Lin, Hanlin Hu, and Tom Wu. Recent progress with one-dimensional metal halide perovskites: from rational synthesis to optoelectronic applications. *NPG Asia Materials*, 15, 2023.

[7] G. Divitini, S. Cacovich, F. Matteocci, L. Cinà, A. Di Carlo, and C. Ducati. In situ observation of heat-induced degradation of perovskite solar cells. *Nature Energy*, 1:15012, 2016.

[8] H.T. Zhang, J. Tersoff, S. Xu, H.X. Chen, Q.B. Zhang, K.L. Zhang, and Y. Yang. Approaching the ideal elastic strain limit in silicon nanowires. *Science Advances*, 2(8):e1501382, 2016.

[9] Md Saiduzzaman, Hikaru Yoshida, Takahiro Takei, Sayaka Yanagida, Nobuhiro Kumada, Masanori Nagao, Hisanori Yamane, Masaki Azuma, Mirza H. K. Rubel, Chikako Moriyoshi, and Yoshihiro Kuroiwa. Hydrothermal synthesis and crystal structure of a (ba0.54k0.46)4bi4o12 double-perovskite superconductor with onset of the transition tc 30 k. *Inorganic Chemistry*, 58(18):11997–12001, 2019. PMID: 31469548.

[10] Charles Kittel. *Introduction to Solid State Physics*. John Wiley & Sons, 2005.

[11] Neil W. Ashcroft and N. David Mermin. *Solid State Physics*. Saunders College, 1976.

[12] Auguste Bravais. Mémoire sur les systèmes formés par des points distribués régulièrement sur un plan ou dans l'espace. *Journal de l'École polytechnique*, 1951.

[13] LibreTexts. Crystal lattices and unit cells. *Chemistry LibreTexts*, 2023.

[14] Byjus. Bravais lattice - 14 possible crystal structures with illustrations. 2023.

[15] H. Zhang et al. Metal halide perovskite for next-generation optoelectronics: progresses and prospects. *eLight*, 2(3):540–555, 2023.

[16] H. Zhang et al. Highly flexible organo-metal halide perovskite solar cells based on silver nanowire–polymer hybrid electrodes. *Nanoscale*, 15:5429–5436, 2023.

[17] K. Lim et al. Flexible optoelectronic devices based on metal halide perovskites. *Energy & Environmental Science*, 14:2009–2035, 2021.

[18] M. Wang et al. Strategies for enhancing the stability of metal halide perovskites towards robust solar cells. *Science China Materials*, 65:2032–2050, 2022.

[19] Xin Li and others. Dynamic ferroelasticity in methylammonium lead halide perovskites. *Science Advances*, 5(5):eaaw5558, 2019.

[20] Wei Li, Tao Zhang, and Xiao Chen. Dynamic domain wall motion and strain-driven phenomena in perovskite nanowires. *Nature Communications*, 12(345):2045–2052, 2021.

[21] Xin Wang and Hongjie Zhao. Ferroelasticity in halide perovskites and its implications for electronic applications. *Journal of Applied Physics*, 127(20):2017–2021, 2020.

[22] Quanxi Jia. Strain engineering: A pathway for tunable functionalities of perovskite metal oxide films. *Nanomaterials*, 12:835, 2022.

[23] Shuai Wang et al. Strain effects in 2d hybrid organic–inorganic perovskite microplates: bandgap, anisotropy, and stability. *Nanoscale*, 12:6644–6650, 2020.

[24] Bowen Yang et al. Strain effects on halide perovskite solar cells. *Chemical Society Reviews*, 51:7509–7530, 2022.

[25] L. A. B. Marcal et al. In situ imaging of ferroelastic domain dynamics in cspbbr3 perovskite nanowires by nanofocused scanning x-ray diffraction. *ACS Nano*, 14:15973–15982, 2020.

[26] Jun Yin and Li Wang. Pressure-induced phase transitions and photoluminescence of cspbbr3 perovskite. *Journal of Physical Chemistry Letters*, 11(3):785–793, 2020.

[27] Li Wang, Jun Yin, et al. Pressure-induced phase transitions and photoluminescence of $cspbbr_3$ perovskite. *Journal of Physical Chemistry Letters*, 11(3):785–793, 2020.

[28] Lucas M Farigliano, Fabio Negreiros Ribeiro, and Gustavo Martini Dalpian. Phase transitions in cspbbr3: evaluating perovskite behavior over different time scales. *Materials Advances*, 5(12):5794–5801, 2024.

[29] D.L. Zhao and Z. Liu. Pressure-induced structural and optical properties of cspbbr3 perovskite nanocrystals. *Journal of Physical Chemistry C*, 125:3752–3758, 2021.

[30] Zhiwei Guo, Haitao Jiang, and Hong Chen. Hyperbolic metamaterials: From dispersion manipulation to application. *J. Appl. Phys.*, 127:071101, 2020.

[31] Xuelei Jing, Dongli Zhou, Rui Sun, et al. Phase stability and electronic structure of cspbbr3 perovskites under rare-earth doping and hydrostatic pressure. *Journal of Materials Science*, 56(9):7400–7411, 2021.

[32] A. K. Tagantsev and P. Yudin. Flexoelectricity in solids: From theory to applications. *Journal of Electroceramics*, 30:173–182, 2013.

[33] W. Ma and L. E. Cross. Flexoelectricity of barium titanate. *Applied Physics Letters*, 88:232902, 2006.

[34] L. E. Cross. Flexoelectricity in ceramics and its use in sensors and actuators. *Journal of Materials Science*, 41:53–63, 2006.

[35] R. Pirc and J. Koruza. Flexoelectricity and strain effects in perovskite solar cells. *Nanomaterials*, 10(6):1167, 2020.

[36] L. Wang, S. Shi, et al. Giant flexoelectric polarization in perovskite materials. *Physical Review B*, 87(6):064104, 2013.

[37] S. Zhou et al. Flexoelectricity in nanostructures: Tunable energy harvesting and sensing. *Journal of Vibration Engineering & Technologies*, 12:85–98, 2023.

[38] Vytautas Bučinskas, Darius Viržonis, and Inga Morkvėnaitė-Vilkončienė. Characteristics and functionality of cantilevers and scanners in atomic force microscopy. *Materials*, 16(19):6379, 2023.

[39] Burg T. P. and others. Fluidic applications for atomic force microscopy (afm) with microcantilever sensors. *Experiments in Fluids*, 15:1466–1476, 2006.

[40] Zhang H. Xu J., Li Y. Atomic force microscopy-based advanced characterization of thermal properties. *Nano Energy*, 80:1051–1060, 2021.

[41] C. S. De Castro E. V. Péan, S. Dimitrov and M. L. Davies. Interpreting time-resolved photoluminescence of perovskite materials. *Physical Chemistry Chemical Physics*, 22:28345–28358, 2020.

[42] Chaohui Li et al. Christian Kupfer, Vincent M. Le Corre. Unravelling material properties of halide perovskites by combined microwave photoconductivity and time-resolved photoluminescence spectroscopy. *Journal of Materials Chemistry C*, 12:95–102, 2024.

[43] Peter Y. Yu and Manuel Cardona. *Fundamentals of Semiconductors: Physics and Materials Properties*. Springer, Berlin, Heidelberg, 4th edition, 2010.

[44] Claus F. Klingshirn. *Semiconductor Optics*. Springer, Berlin, Heidelberg, 3rd edition, 2007.

[45] Qingquan He Jun Pan Kang Qu, Tao Zhang. Metal halide perovskite nanowires: Controllable synthesis, mechanism, and application in optoelectronic devices. *Nanomaterials*, 13:419, 2023.

[46] Haizheng Zhong Xiaohui Li, Xinzheng Zhang. Nanophotonics with hybrid perovskite nanowires. *Journal of Materials Chemistry C*, 4:5872–5880, 2016.

[47] MIT OpenCourseWare. Laser fundamentals i, 2008. Massachusetts Institute of Technology.

[48] ECE533 Cornell. Handout 11: Experimental setup, 2010. Cornell University.

[49] Gary Blair. The basics of light, 2019. Johns Hopkins University.

[50] Tomas Leijtens James M. Ball Alain Goriely Henry J. Snaith Samuel D. Stranks, Victor M. Burlakov. Recombination kinetics in organic-inorganic perovskites: Excitons, free charge, and subgap states. *Physical Review Applied*, 2(3):034007, 2014.

[51] S. Pathak L. E. Klintberg D. D. Jarausch R. Higler S. Huttner T. Leijtens S. D. Stranks H. J. Snaith M. Atature R. T. Phillips R. H. Friend F. Deschler, M. Price. High photoluminescence efficiency and optically pumped lasing in solution-processed mixed halide perovskite semiconductors. *The Journal of Physical Chemistry Letters*, 5:1421–1426, 2014.

[52] HORIBA Scientific. Time-correlated single photon counting (tcspc): A comprehensive guide. 2020. Accessed: September 29, 2024.

[53] Edinburgh Instruments. Tcspc - what is time-correlated single photon counting? 2023. Accessed: September 29, 2024.

[54] Edinburgh Instruments. *Edinburgh Instruments TCSPC Manual*, 2019. User Manual.

[55] HORIBA Scientific. Time-resolved photoluminescence studies of nanowires using tcspc. *HORIBA Applications*, 2022. Accessed: September 29, 2024.

[56] L Li, X Liu, D Yang, J Xu, and F Huang. Template synthesis and photoluminescence tuning of $cspbx_3$ (x = cl, br) nanowires. *Advanced Materials*, 30(25):1800670, 2018.

[57] X Xu, X Cao, J Liu, Y Wang, and J Zhang. Anion exchange in cesium lead halide perovskite nanowires for tunable photoluminescence. *Nanoscale*, 10:15126–15131, 2018.

[58] Q Dong, Y Fang, Y Shao, Y Yuan, and J Huang. Preparation of perovskite nanowires using anodic alumina templates. *Journal of Materials Chemistry A*, 3:5360–5367, 2015.

[59] W Yang, Q Chen, Z Jin, X Zhang, and S Liu. Growth of perovskite nanowires and their optical properties. *Journal of Physical Chemistry C*, 120:14574–14580, 2016.

[60] Nils Lamers, Zhaojun Zhang, and Jesper Wallentin. Perovskite-compatible electron-beam-lithography process based on nonpolar solvents for single-nanowire devices. *ACS Applied Nano Materials*, 5:3177–3182, 2022.

[61] Nils Lamers, Zhaojun Zhang, Igor G. Scheblykin, and Jesper Wallentin. Gas-phase anion exchange for multisegment heterostructured cspb(br1-xclx)(3) perovskite nanowires. *Advanced Optical Materials*, 7:1–9, 2023.

[62] E. Pereira-Andrade, M.V.H. Machado, N. Lamers, Z. Huang, J. Wallentin, A. Malachias, L.A. Cury, L.A.B. Marçal, and G.A.M. Sáfar. Thermal effects on the dynamics of excitons in cspb(br1xclx)3. *Solid State Sciences*, 168:108043, 2025.

[63] J. M. Richter, M. Abdi-Jalebi, A. Sadhanala, M. Tabachnyk, J. P. H. Rivett, L. M. Pazos-Outón, and et al. Enhancing photoluminescence yields in lead halide perovskites by photon recycling and light trapping. *Nature Communications*, 7:13941, 2016.

Appendix A - Additional Data

Atomic Force Microscopy (AFM)

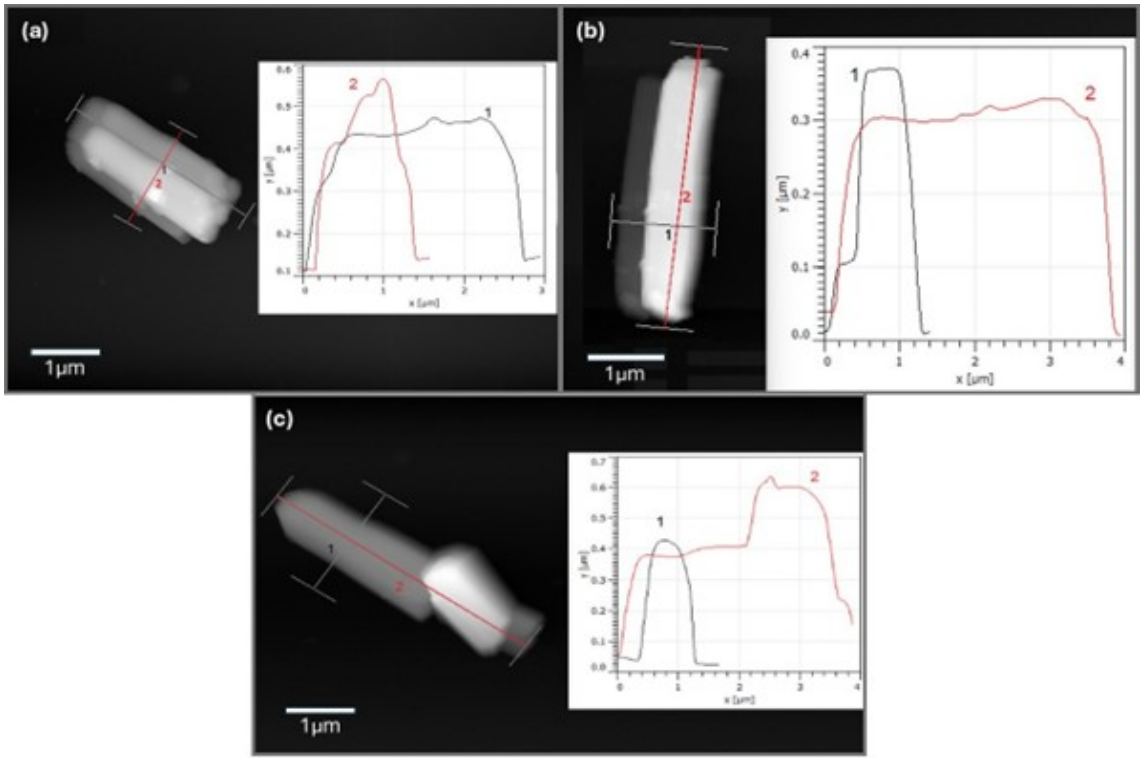

Figura 1: Topographic AFM images of $CsPbBr_3$ NWs deposited on a Si_3N_4 substrate. (a) Image of a single $CsPbBr_3$ NW showing its smooth and uniform surface. (b) Another $CsPbBr_3$ NW displaying similar morphology, confirming the consistency in synthesis. (c) AFM image of a $CsPbBr_3$ NW that broke during measurement. The insets in each panel present the corresponding horizontal (1) and vertical (2) profiles, displaying the NWs' thicknesses and lengths, extracted using Gwyddion software.

Atomic Force Microscopy (AFM) measurements were carried out to complement the morphological analysis of $CsPb(Br_{1-x}Cl_x)_3$ nanowires. These results, presented in Figures 1–3, provide detailed evidence of the structural quality of the nanowires and the effects of the anion exchange process on their morphology.

Figure 1 shows representative AFM images of as-synthesized $CsPbBr_3$ nanowires grown inside anodized aluminum oxide (AAO) templates. The nanowires exhibit lengths in the range of 3–5 μm and diameters of approximately 250 nm, consistent with the template pore sizes. The height profiles extracted from these images confirm that the NW diameter is uniform along their axis, demonstrating the effectiveness of the template-assisted growth technique. This uniformity ensures that optical characterization, such as PL mapping, can be interpreted without major morphological fluctuations influencing the emission.

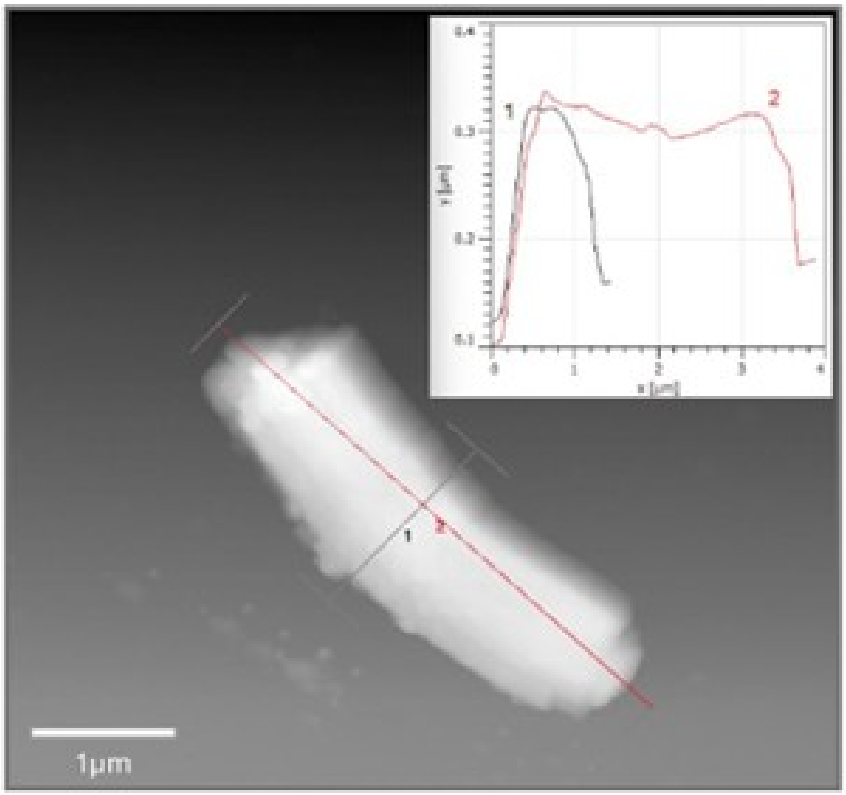

Figura 2: Topographic AFM image of a $CsPbCl_3$ NW obtained through complete anion exchange, where Br ions in the original $CsPbBr_3$ NWs are replaced by Cl ions. The NW is deposited on a Si_3N_4 substrate, maintaining a smooth and uniform surface, indicative of the successful exchange process without compromising the structural integrity. The inset displays the horizontal (1) and vertical (2) profiles, showing the NW's thickness and length, extracted using Gwyddion software.

After gas-phase anion exchange, $CsPbCl_3$ nanowires were obtained. Figure 2 displays AFM images of these fully substituted NWs. The morphology is preserved during the exchange process, with the nanowires maintaining their characteristic diameter and smooth surface topography. This demonstrates that the chemical substitution from Br to Cl does not cause surface roughening or structural degradation, confirming the robustness of the exchange method. The preservation of morphology

is critical for ensuring that any modifications in the optical response are attributed to compositional and structural changes, rather than to degradation artifacts.

Finally, Figure 3 highlights an important observation of mechanical fragility in certain nanowires. During AFM scanning, one nanowire was found to break along its length, as shown in the topography. This effect is attributed to strain heterogeneities generated by ferroelastic domain formation and reordering within the perovskite lattice. While such events were rare, they provide direct evidence of internal strain accumulation that can influence both the mechanical stability and the optoelectronic behavior of the nanostructures. This result is consistent with the discussion in Section 4.1.4, where ferroelastic reorganization was shown to strongly impact exciton recombination dynamics.

In summary, the AFM data confirm the morphological uniformity of $CsPbBr_3$ nanowires, the preservation of structural integrity after anion exchange to $CsPbCl_3$, and the occasional occurrence of mechanical fragility due to strain heterogeneity. These observations strengthen the conclusion that the optoelectronic effects reported in this thesis arise from intrinsic structural dynamics rather than from extrinsic degradation of the nanowires.

Temperature-Dependent Photoluminescence and Reproducibility

To explore the temperature dependence of the photoluminescence (PL) response in $CsPb(Br_{1-x}Cl_x)_3$ nanowires, a series of additional measurements were performed under carefully controlled heating and cooling cycles. These experiments were designed to consolidate the observations presented in the main body of the thesis, namely the abrupt PL shifts near phase transition temperatures, the associated hysteresis effects, and the enhancement of exciton lifetimes. By extending the measurements to several nanowires and repeating thermal cycling procedures, a more comprehensive picture of the optical behavior was obtained.

Figure 4 shows representative PL spectra collected from the Cl-rich half of a heterojunction nanowire over a range of temperatures. As the sample is heated, a distinct discontinuity in the emission peak is observed near 305 K. This discontinuity corresponds directly to the orthorhombic-to-tetragonal phase transition of $CsPbCl_3$, a crystallographic rearrangement that strongly influences the band structure and, consequently, the optical emission. The spectral change is abrupt rather than gradual, reflecting the sudden nature of the structural transformation. This observation is consistent with the behavior reported in Section 4.1.3, where the non-radiative

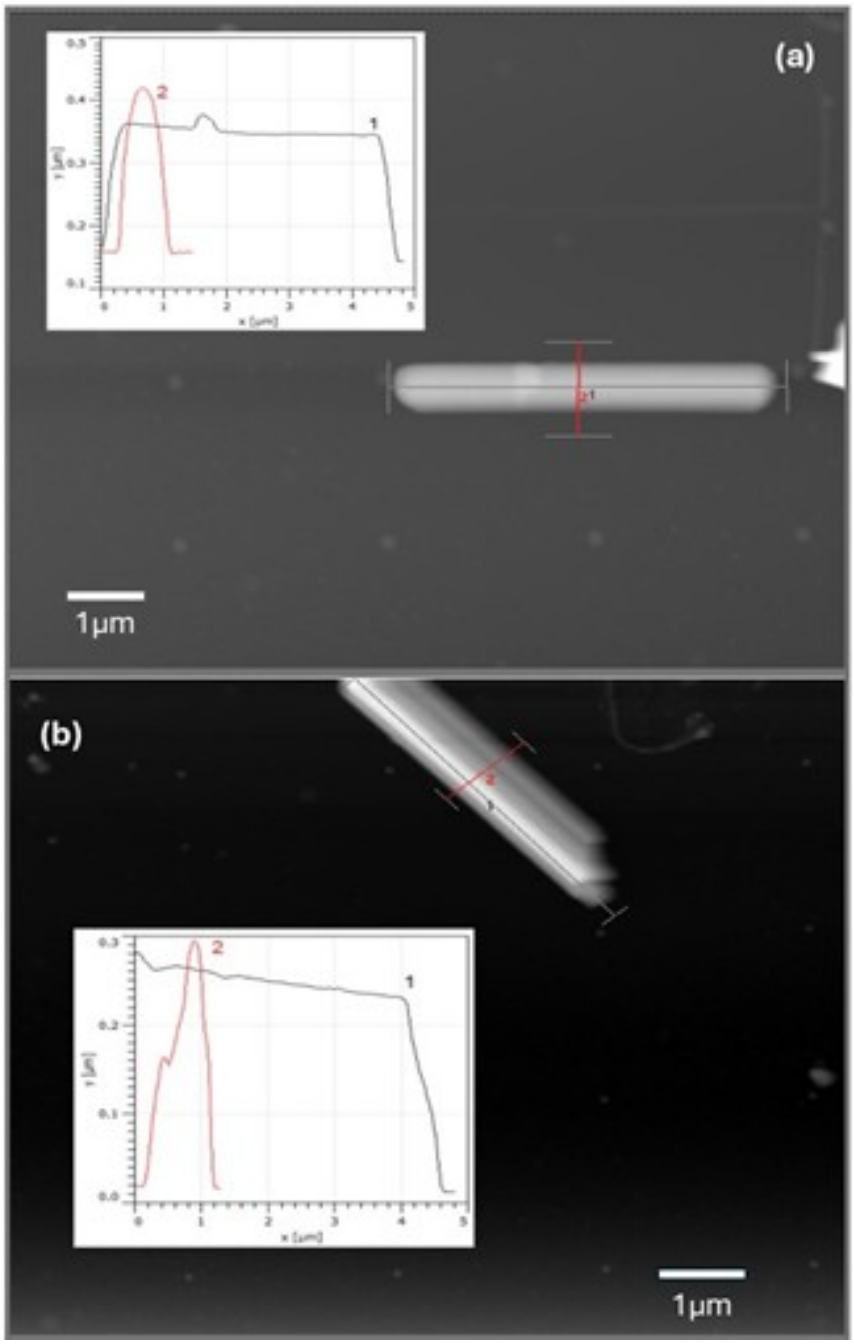

Figura 3: Topographic AFM images of two different heterojunction nanowires (NWs) composed of $CsPb(Br_{1x}Cl_x)_3$. (a) and (b) display NWs where one half consists of $CsPbBr_3$ and the other of $CsPbCl_3$. The AFM measurements reveal no visible topographic transitions along the interface. The insets in both panels show the horizontal (1) and vertical (2) profiles, highlighting the thickness and length of the NWs, obtained using Gwyddion software.

recombination channel (P2) also exhibited a marked increase in lifetime at the same transition temperature.

To investigate whether the Br-rich half of the heterojunction is also influenced

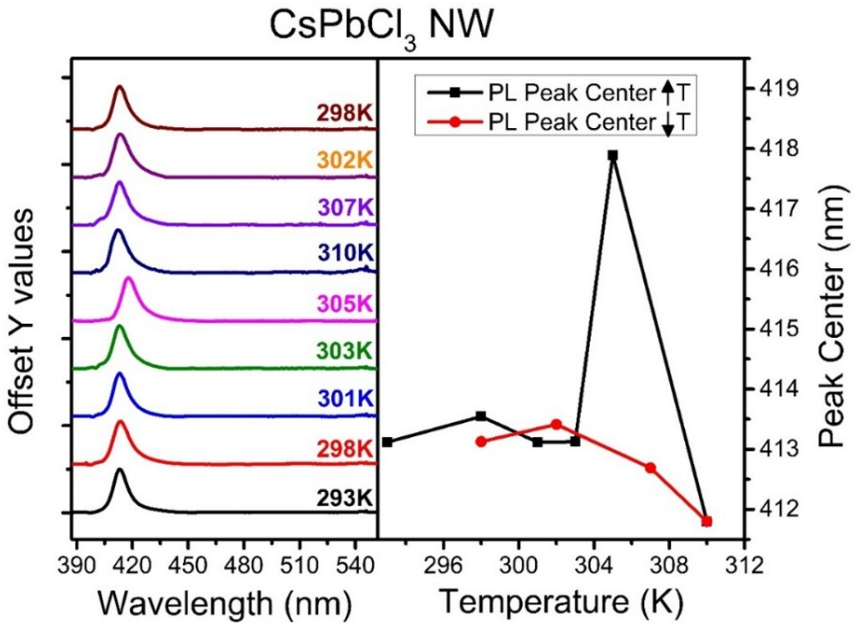

Figura 4: (Left) PL spectra of a $CsPbCl_3$ nanowire (NW) measured using the second setup, with varying temperature. (Right) Variation of the PL peak center as a function of temperature, showing a significant shift at the known phase transition temperature of $CsPbCl_3$ reported in the literature.

by the Cl-rich phase transition, PL measurements were performed under identical conditions in the opposite segment of the nanowire. The results, presented in Figure 5, reveal that even in the Br-rich half, which undergoes its intrinsic transition only at ∼361 K, a correlated feature appears at ∼305 K. This indicates that the Br-rich domain is affected by the Cl-rich transition through long-range coupling mechanisms. Two effects contribute to this behavior: (*i*) charge carrier diffusion along the nanowire axis, allowing carriers generated in one half to recombine in the other, and (*ii*) photon recycling, whereby emitted photons are reabsorbed and re-emitted in adjacent regions. Both mechanisms extend the influence of the Cl-rich transition beyond its local domain, effectively coupling the optical responses of the two segments of the nanowire. This finding reinforces the idea that heterojunction nanowires act as integrated systems rather than as isolated regions.

Another important feature revealed by these measurements is the presence of hysteresis. Figure 6 presents the evolution of the PL peak position in a Cl-rich nanowire during both heating and subsequent cooling. The trajectories are clearly not coincident: the peak position during cooling does not retrace the path followed during heating but remains shifted. This hysteresis is interpreted as a manifestation of ferroelastic domain reordering, as discussed in Section 4.1.4. When the phase transition occurs, domains reorganize to minimize internal strain, but upon cooling

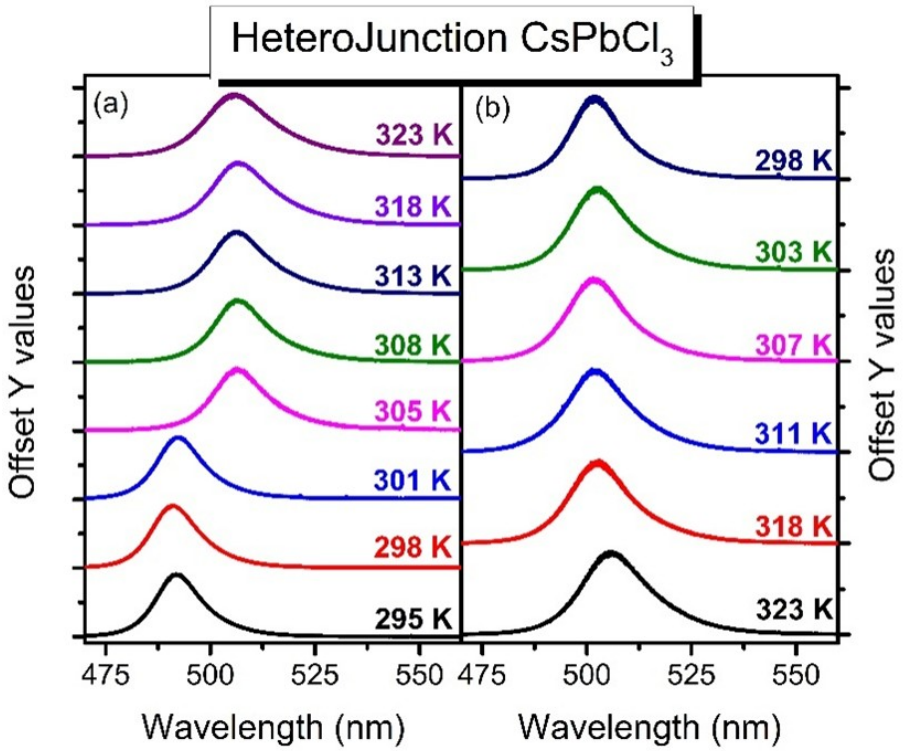

Figura 5: PL spectra of the Cl-rich region of a heterojunction NW. (a) Evolution of the spectra during the heating process. (b) PL spectra collected during the cooling process, completing a full heating-cooling cycle.

they do not immediately return to their original configuration. The residual strain introduces a memory effect in the lattice, which is reflected in the PL peak trajectory. This behavior is in line with the exciton lifetime changes summarized in Table 4.5, where the non-radiative channel P2 exhibited delayed recovery during cooling cycles.

To assess the generality of this behavior, similar measurements were carried out on additional nanowires. Figure 7 shows the temperature-dependent PL response of another heterojunction nanowire, where the emission again exhibits a discontinuity near 305 K. The recurrence of this feature in different samples under comparable conditions suggests that the optical signatures associated with the $CsPbCl_3$ transition are characteristic of the system. This strengthens the interpretation that the observed optical modulations are inherent to the material.

Finally, Figure 8 compiles PL peak positions obtained from several nanowires subjected to thermal cycling. The consistent appearance of the transition signature at 305 K across different datasets, along with the systematic hysteresis observed between heating and cooling, highlights the recurrent character of these phenomena. It is important to note that, although the laser excitation spectrum shown in Figure 8 presents a linewidth comparable to the PL emission width, no decon-

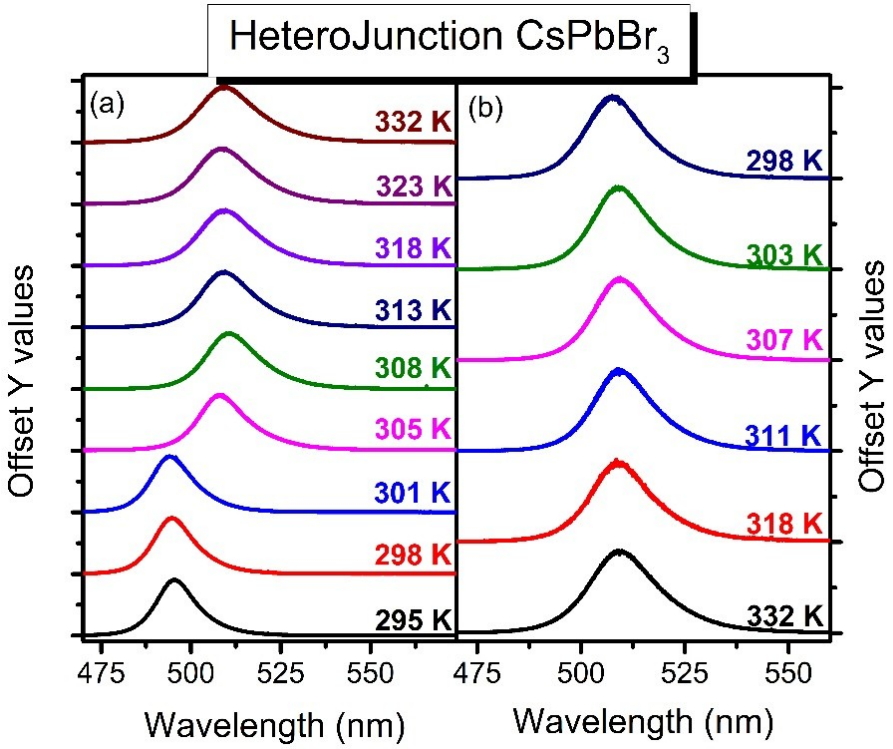

Figura 6: PL spectra of the Br-rich region of a heterojunction NW. (a) Evolution of the spectra during the heating process. (b) PL spectra collected during the cooling process, completing a full heating-cooling cycle.

volution was required. The excitation laser was used solely as the optical pump, and its spectral contribution was completely suppressed by an optical filter placed before the detector. As a result, the measured PL profiles are unaffected by the excitation source and are limited only by the monochromator resolution, thus reflecting the intrinsic emission characteristics of the nanowires. Taken together with the lifetime data summarized in Table 4.5, these results emphasize the strong connection between ferroelastic reordering, strain-induced band modulation, and excitonic dynamics in $CsPb(Br_{1-x}Cl_x)_3$ nanowires.

In addition to steady-state PL, further insights were obtained from time-resolved PL (TRPL) measurements performed on different nanowires. These complementary experiments, shown in Figure 9, reveal that the enhancement of exciton lifetime near 305 K is not limited to a single measurement but is observed consistently across independent nanowires and thermal cycles. The decay traces reproduce the same qualitative trend described in Section 4.1.3: outside the transition region, the non-radiative recombination pathway dominates and results in fast decay components, while near 305 K the suppression of non-radiative channels leads to longer decay times. The agreement between steady-state and time-resolved observations further

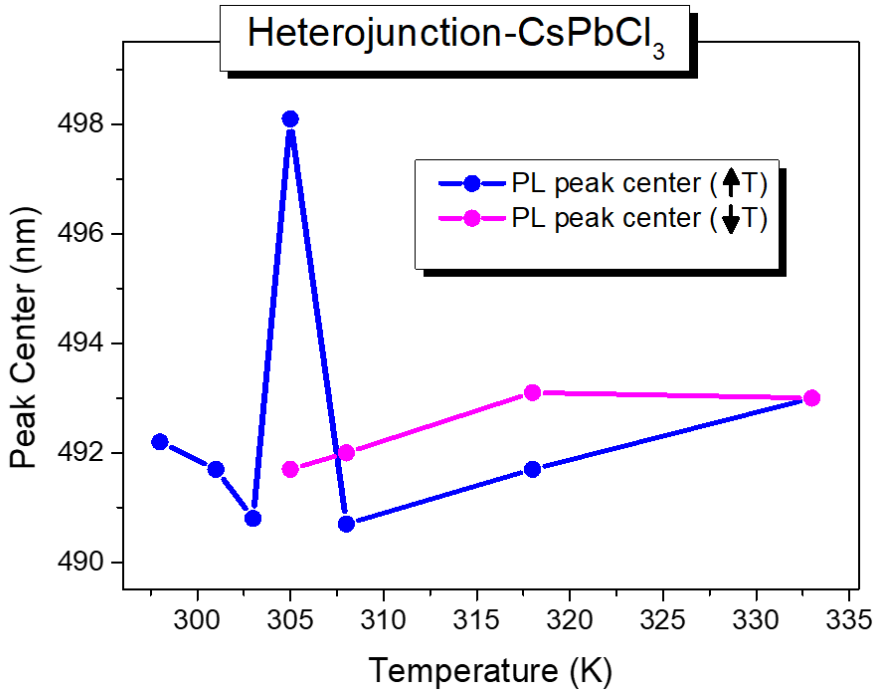

Figura 7: Evolution of the PL peak center for the Cl-rich region of the heterojunction NW during a different thermal cycle, showing both the heating (blue) and cooling (pink) processes. The consistent behavior across cycles demonstrates the reproducibility and coherence of the PL response with temperature changes.

consolidates the interpretation that structural reordering of ferroelastic domains plays a decisive role in modulating recombination dynamics.

In summary, the extended PL measurements presented in Figures 4–9, together with the quantitative analysis in Table 4.5, provide a broader perspective on the optical behavior of $CsPb(Br_{1-x}Cl_x)_3$ nanowires. The results confirm that the phase transition near 305 K consistently impacts both the PL peak position and the exciton lifetime, and that ferroelastic domain reordering gives rise to hysteresis effects that appear repeatedly across different measurement cycles. These findings reinforce the interpretation that the optical response of these nanostructures is intrinsically linked to their structural dynamics.

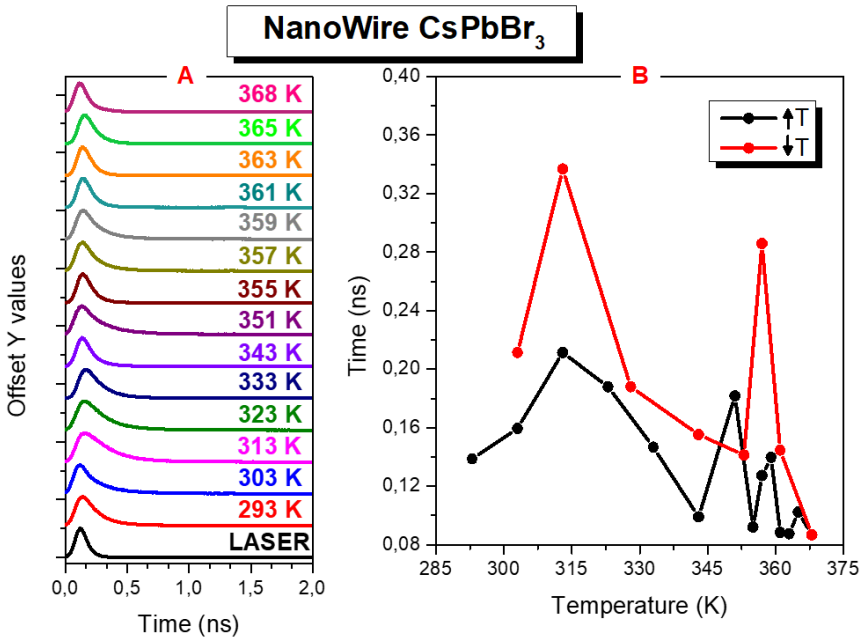

Figura 8: (a) Time-resolved PL decay spectra of a $CsPbBr_3$ NW measured across different temperatures. (b) Decay time variation as a function of temperature, showing a significant change around 361 K, corresponding to the crystallographic phase transition of $CsPbBr_3$.

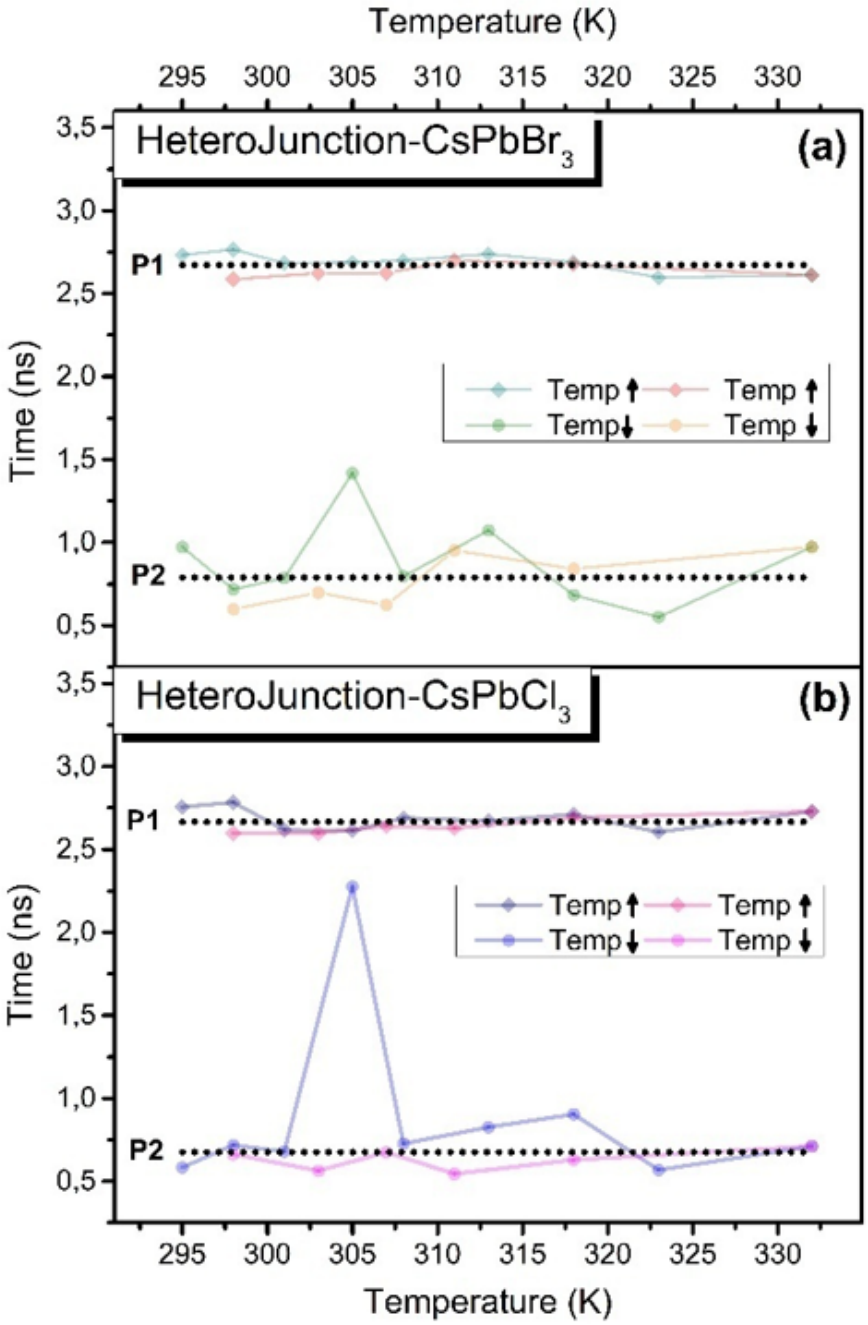

Figura 9: Comparison of decay times (P1 and P2) for the heterojunction NWs as a function of temperature. (a) Lifetime trends for the Br-rich region, and (b) Lifetime trends for the Cl-rich region. The black dotted lines represent the average decay times, excluding the 305 K point, highlighting the deviation in lifetime behavior near the phase transition. These results emphasize the differences in excitonic recombination dynamics between the two regions and across different temperatures.

Appendix B - List of Complete Publications and Collaborations

(1). Aggregation-induced emission and temperature-dependent luminescence of potassium perylenetetracarboxylate. − Samuel Brum Martins, **Everton Pereira de Andrade**, Subodh K. Gautam, Olivier Plantevin, Luiz Alberto Cury, Angelo Malachias, and Gustavo de Almeida Magalhães Sáfar − *Journal of Fluorescence*, 2021.

(2). The Special Case of the Spectral Emission of a Tb^{3+} Mono Metal Complex − Mazzoni, M. S. C.; Toledo, J. R.; **Pereira-Andrade, E.**; Krambrock, K.; Cury, L. A.; Malachias, A.; Safar, G. A. M. − *ChemPhysChem*, 2022

(3). Controlled ultrasonic nebulization: A physical vapor deposition variant for low temperature and low growth rate of small molecule thin films − Lucas Polesi, **Everton Pereira de Andrade**, Angelo Malachias, Luiz Alberto Cury, Gustavo de Almeida Magalhães Sáfar − *Organic Electronics*, 2023

(4). Evidence of thickness-dependent surface-induced ferroelectricity in few-layer germanium sulfide obtained via scanning tunneling spectroscopy. − R. R. Barreto, T. C. Ribeiro, G. H. R. Soares, **E. Pereira**, D. R. Miquita, G. A. M. Safar, and others − *Nanoscale*, 2024.

(5). Scanning Tunneling Spectroscopy Method for the Prediction of Semiconductor Heterojunction Performance as a Prequel for Device Development. − T. C. Ribeiro, D. H. S. Fonseca, R. R. Barreto, **E. Pereira-Andrade**, D. R. Miquita, and others − *ACS Applied Materials & Interfaces*, 2023.

(6) Investigation of the Impact of Thionine Functionalization on Magnetoelastic Sensor Performance. − DA SILVA, WENDERSON R. F. ; RODRIGUES-JUNIOR, GILBERTO ; DE ARAÚJO, EDUARDO N. D. ; **PEREIRA-ANDRADE, EVER-**

TON ; MALACHIAS, ÂNGELO ; MENDES, JOAQUIM B. S. – *Acs Applied Bio Materials*, 2025

(7) **Thermal effects on the dynamics of excitons in CsPb(Br1xClx)3.** – **PEREIRA-ANDRADE, E.**; MACHADO, M.V.H. ; LAMERS, N. ; HUANG, Z. ; WALLENTIN, J. ; MALACHIAS, A. ; CURY, L.A. ; MARÇAL, L.A.B. ; SÁFAR, G.A.M.. – *SOLID STATE SCIENCES*, 2025

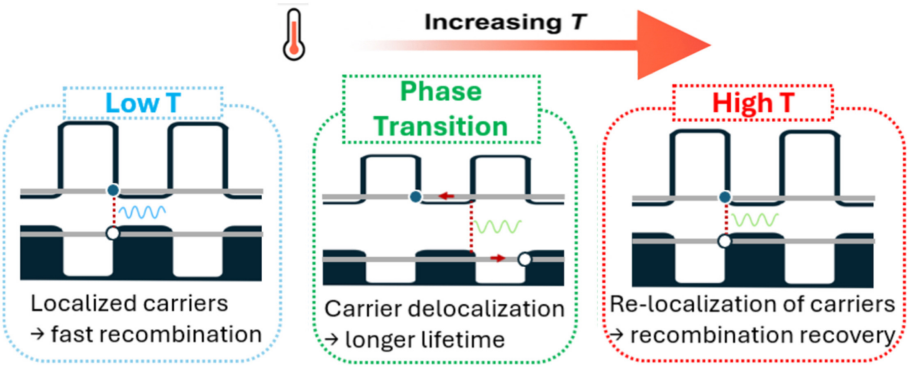

(8) **Multiple Quasiparticle Interactions in Molecularly Functionalized h-BN Polaritonic Systems.** – **Everton Pereira-Andrade**, Rafael Reis Barreto, Yuri Bernardes, Ingrid David Barcelos, Angelo Malachias, Francisco Carlos Barbosa Maia and Gustavo de Almeida Magalhaes Sáfar. – *J. Phys. Chem. C*, 2025

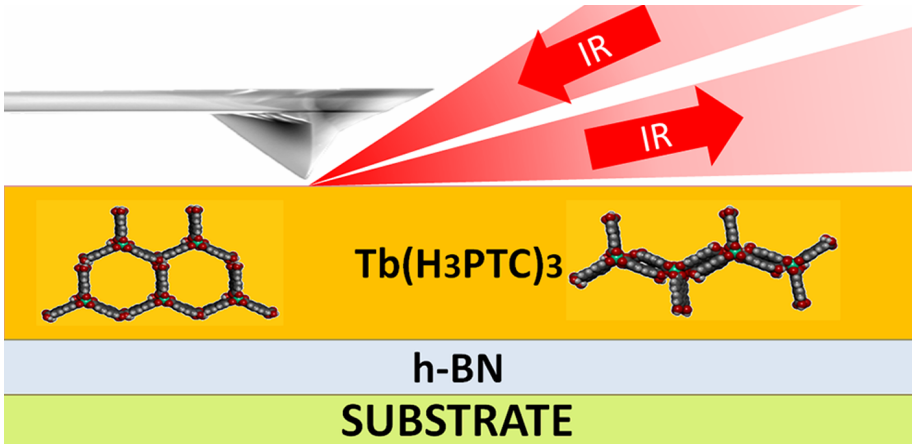

Appendix C - Published Article: $CsPb(Br_{1-x}Cl_x)_3$ Nanowires

This appendix presents the full version of the published article related to this work.

The full article is reproduced below in its original published format.

Solid State Sciences 168 (2025) 108043

Contents lists available at ScienceDirect

Solid State Sciences

journal homepage: www.elsevier.com/locate/ssscie

Thermal effects on the dynamics of excitons in $CsPb(Br_{1-x}Cl_x)_3$

E. Pereira-Andrade [a], M.V.H. Machado [a], N. Lamers [b], Z. Huang [b], J. Wallentin [b], A. Malachias [a], L.A. Cury [a], L.A.B. Marçal [c], G.A.M. Sáfar [a,*]

[a] Departamento de Física, Instituto de Ciências Exatas, Universidade Federal de Minas Gerais, Av. Antônio Carlos, Belo Horizonte, 6627, Minas Gerais, Brazil
[b] Synchrontron Radiation Research and NanoLund, Lund University, Box 118, Lund, 22100, Sweden
[c] Brazilian Synchrotron Light Laboratory (LNLS), Brazilian Center for Research in Energy and Materials (CNPEM), Campinas, 13083-970, São Paulo, Brazil

A B S T R A C T

The long-standing debate in the scientific community about whether ferroelectricity or ferroelasticity is the key property influencing the optoelectronic behavior of metal halide perovskites continues. In this study, we experimentally investigate the temperature dependence of photoluminescence from $CsPb(Br_{1-x}Cl_x)_3$ nanowires and their heterojunctions. Our findings show an enhancement of the exciton lifetime in the $CsPb(Br_{1-x}Cl_x)_3$ nanowires, which we attribute to crystallographic phase transitions, independent of halide composition explored in this study and its effect on transition temperatures. Understanding the phenomenon could help to improve perovskite-based photovoltaic devices, especially when these devices operate at temperatures slightly above room temperature. We propose a mechanism that models the nanowires as disordered strain superlattices, suggesting that flexoelectric spatial modulation plays a significant role in defining their light emission properties. These insights could, in principle, be extended to explain similar phenomena in the systems of many other metal halide perovskites. Our research provides valuable understanding into how phase transitions can be leveraged to extend exciton lifetimes and optimize charge carrier dynamics, potentially leading to advancements in the efficiency of solar cells and light-emitting devices.

1. Introduction

The long-standing debate about the influence of ferroelectricity and ferroelasticity in metal halide perovskites (MHPs) has attracted great interest of the materials science community [1–3]. Indeed, ferroelectricity has been measured in metal halide perovskites directly [3,4]. However, the mere presence of ferroelectricity could play a minor role in the optoelectronic properties of metal halide perovskites, as alleged by some.1 If ferroelasticity has a leading role in that, there is a lack of clarification on how it exerts influence on charge carriers.

Flexoelectricity is the effect of electrical polarization of dielectrics face to a strain gradient. It is present in many materials systems [5]. It was recently demonstrated that lead halide perovskites can exhibit flexoelectricity response [6]. It is also known from previous works that ferroelastic domains can appear in $CsPbBr_3$ nanostructures under different conditions, induced by crystal phase transitions [7,8], external stress [9] or geometrical constraints [10].

Recent studies have indicated that phase transitions within perovskite materials can significantly extend the exciton lifetime, enhancing the device's overall efficiency. Specifically, during these transitions, the exciton lifetime can increase to more than 1ns, thereby facilitating better charge carrier separation and reducing recombination losses [11,12]. Such enhancement in exciton lifetime is advantageous, particularly in solar cells and light-emitting devices where sustained carrier dynamics are critical for performance [13].

In this work, $CsPbBr_3$ nanowires (NWs) were epitaxially grown and transferred to a fresh substrate. Anion exchange was carried out in order to partially or totally substitute Br by Cl in some of the structures. Steady-state as well as time-decay photoluminescence were measured. Time correlation photon counting spectroscopy measurements were taken from main features of the PL spectra. A remarkable improvement of carrier lifetime at the expected phase transition of each nominal composition was retrieved when compared to any other value in the studied temperature range. We model the NWs as disordered strain superlattices, where flexoelectric modulation defines the light emission properties. These findings could help to improve the performance of perovskite-based photovoltaic devices, especially for operating in light concentration conditions where temperatures above room temperature are attained.

Similar advancements in nanoparticle-based technologies have also demonstrated potential for enhancing the performance and stability of optoelectronic devices, offering relevant insights for perovskite systems [14].

* Corresponding author.
E-mail address: safar@fisica.ufmg.br (G.A.M. Sáfar).

https://doi.org/10.1016/j.solidstatesciences.2025.108043
Received 24 June 2025; Received in revised form 29 July 2025; Accepted 5 August 2025
Available online 7 August 2025

2. Experimental

Free-standing $CsPbBr_3$ NWs were grown using anodized aluminium oxide (AAO) templates as previously described [15]. High temperature (343 K) was held for 30 min during growth to make sure part of the NWs could grow above the template and stick out from the pores. After growth, the non-buried parts of the $CsPbBr_3$ NWs were cut out of cleanroom tissue which was carefully moved over the AAO surface, breaking off the free-standing objects. By scraping the same tip across the Si_3N_4 substrate, some of these NWs were deposited onto it. $CsPbCl_3$ NWs samples were obtained by fixing $CsPbBr_3$ NWs to a sapphire carrier wafer subsequently loaded into a Plasma-Therm Apex RIE tool, where gas-phase anion exchange was performed. An Ar/Cl_2 atmosphere was held at $1.33{\cdot}10^{-4}$ bar total pressure with a $3.33{\cdot}10^{-5}$ bar Cl_2 partial pressure for the duration of the exchange process. $CsPb(Br_{1-x}Cl_x)_3$ heterojunction NWs were created using electron beam lithography process based on non-polar solvents [16]. Selected NWs covered by polymethyl methacrylate (PMMA) polymer were processed to reveal half of the NWs. Anion exchange was then carried out at the partially covered NWs, while the other half was uncovered resulting in axially stepped heterostructures, as depicted in Fig. 1.

Steady-state photoluminescence (PL) measurements were conducted on epitaxially grown $CsPbBr_3$, $CsPbCl_3$, and $CsPb(Br_{1-x}Cl_x)_3$ heterojunction NWs using two different experimental setups. The first setup utilized a micro-Raman Witec alpha300 RA Spectrometer, equipped with a 50x objective lens, a 457 nm excitation laser, delivering 0.5 mW of power and focused to a 0.3 μm laser spot. This setup allowed for high spatial resolution, enabling luminescence mapping with steps of 0.15 μm.

The second setup was a homemade configuration, shown schematically in Fig. S5, designed to perform both steady-state and time-resolved PL measurements. This setup employed a 371 nm steady-state laser (Power = 0.1 mW, Laser-Spot = 0.5 μm) for PL measurements, with the removable mirror taken out to direct the emission beam into an ANDOR Shamrock 303i spectrometer for data collection.

For time-correlated single photon counting (TCSPC) measurements, a pulsed 371 nm laser (80 MHz repetition rate, 0.5 μm laser spot) was used. The emission beam was directed through the removable mirror into an Oriel-MS125TM spectrograph, connected to a PMA-M photomultiplier detector assembly (instrument response function of 120 ps) from PicoQuant.

Atomic force microscopy (AFM) topographic images of the NWs were measured for all samples using a Nanosurf C3000 AFM operating in tapping mode using cantilevers with 3 N/m spring constant and minimum values of tip approach setpoint to avoid sample damage.

3. Results

AFM data analysis was carried out using Gwyddion and ImageJ software. The images show an average length of 3–5 μm and average height of 250 nm (see Fig. 2(A)–S1, S2 and S3), reflecting the diameter of the AAO template pores and the consistency with nominal growth parameters. For a detailed representation of the sample morphology, Fig. 2(B) (and Figs. S1, S2 and S3 in the Supplementary Materials) presents an AFM image of the $CsPb(Br_{1-x}Cl_x)_3$ NWs, which underscores the uniformity and pristine quality of the NW arrays. Fig. 2(C) shows an optical microscope image of a single NW, providing a different perspective. Additionally, Fig. 2(D) and (E) illustrate the photoluminescence map of the NWs, revealing a compositional gradient along its length.

Time-resolved PL was measured on the heterojunction NW. Fig. 3(A) shows the time decay curves for its respective spectra, evidencing a difference in the average decay time of the system at 305 K. This is near the expected phase transition temperature (orthorhombic to tetragonal) for pure $CsPbCl_3$.

It is important to notice, however, that the heterojunction NW may

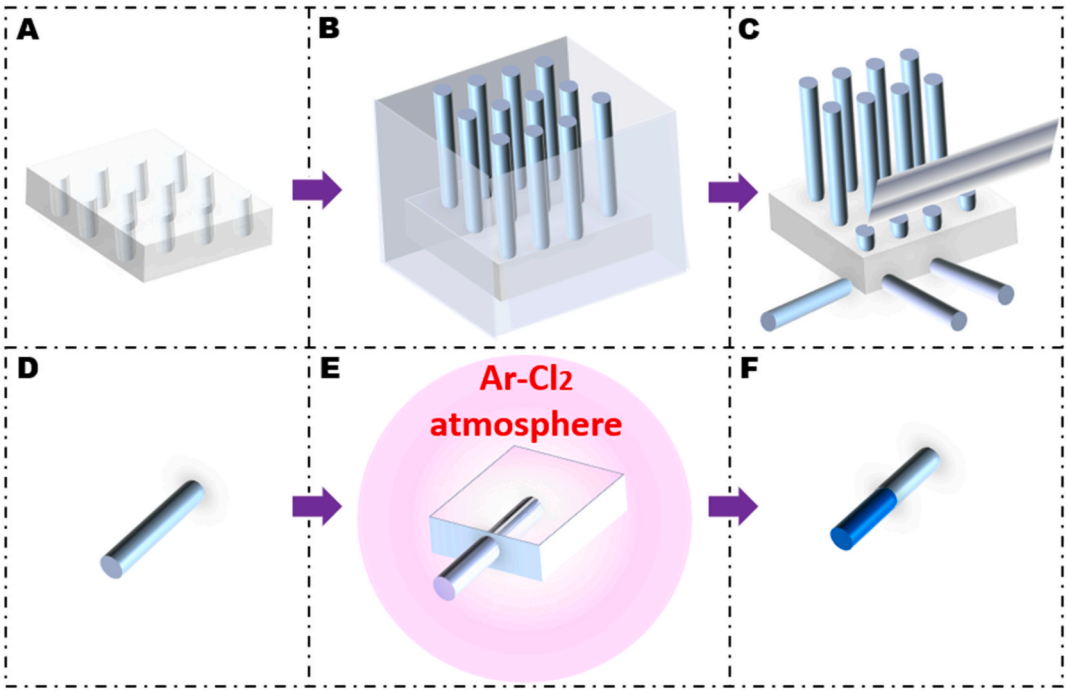

Fig. 1. Schematic illustration of the synthesis of $CsPb(Br_{1-x}Cl_x)_3$ NWs. (A) Depicts the Anodized Aluminum Oxide (AAO) template. (B) Shows the growth of $CsPbBr_3$ using the AAO template at high temperatures for 30 min. Subsequently, in (C), it is cut by a tip and transferred to the desired substrate, forming a $CsPbBr_3$ NW as shown in (D). (E) Illustrates the process after an electron beam lithography, based on non-polar solvents and a PMMA coating that reveals only half of the NW. It is then subjected to an anion exchange loaded into a Plasma-Therm Apex RIE tool in an Ar/Cl_2 atmosphere, resulting in (F) a $CsPb(Br_{1-x}Cl_x)_3$ heterojunction with one half being Br-rich (colored green, upper part of the NW) and the other half being Cl-rich (colored blue, lower part of the NW). (For interpretation of the references to color in this figure legend, the reader is referred to the Web version of this article.)

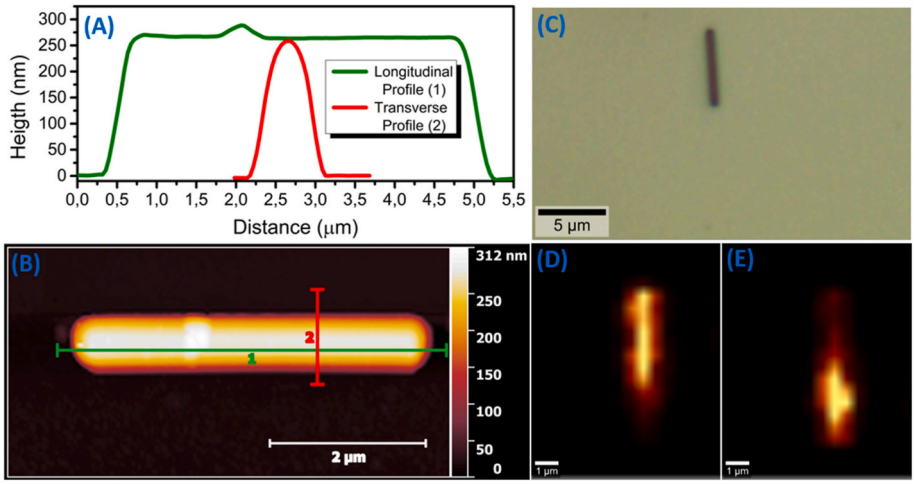

Fig. 2. (A) Profile of the NW obtained using Gwyddion software from AFM measurements. (B) AFM topographic image of a CsPb($Br_{1-x}Cl_x$)$_3$ heterojunction NW. (C) Optical microscopy image of the heterojunction NW alongside its photoluminescence (PL) response when excited at $\lambda_{exc} = 457$ nm. (D) and (E) PL emission maps centered at 507 nm and 523 nm, respectively, each with a bandwidth of 2 nm.

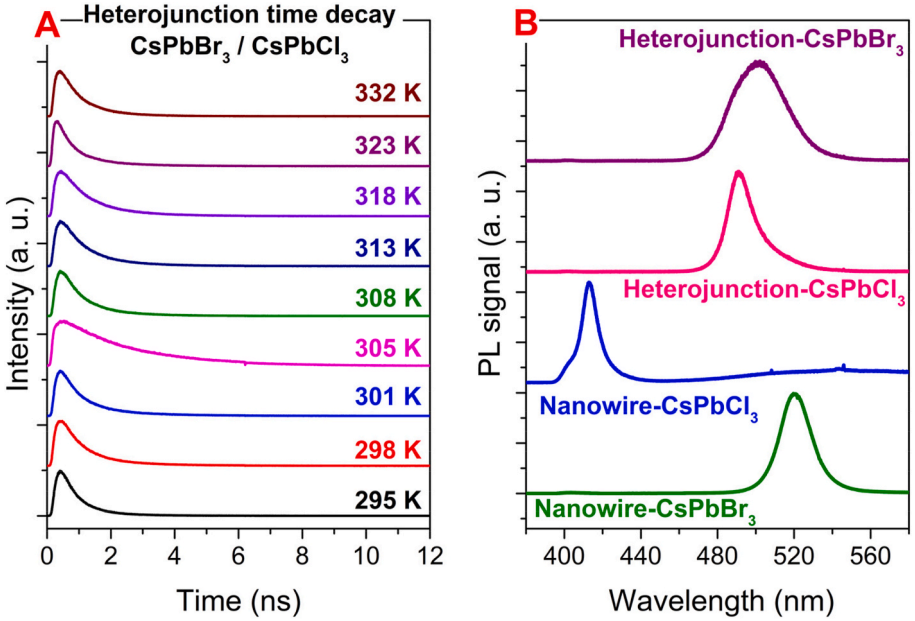

Fig. 3. (A) Time-decay curves for different temperatures during heating of CsPb($Br_{1-x}Cl_x$)$_3$ heterojunction NW. (B) Photoluminescence curves for fully exchanged and Cl-free (pristine) NWs, in blue and in green, respectively. Curves for both sides of CsPb($Br_{1-x}Cl_x$)$_3$ heterojunction NW are represented in purple for the Br-rich half, and pink for the Cl-rich half. (For interpretation of the references to color in this figure legend, the reader is referred to the Web version of this article.)

not be completely Br-free at any point of its crystalline structure. In order to confirm it, PL spectra of the heterostructure has been acquired and compared it with pure $CsPbBr_3$ and $CsPbCl_3$ NWs. Fig. 3(B) shows the PL curve of the respective CsPb($Br_{1-x}Cl_x$)$_3$ NWs, both as grown (Cl-free, pristine), fully exchanged and the heterostructure. The $CsPbBr_3$ NW has a characteristic peak centered in the green region of the spectra, while the pure $CsPbCl_3$ peak is shifted towards blue. The heterojunction was measured with the excitation laser placed at the Br-rich end and a collection of spectra was made along the larger dimension to the other end of the Cl-rich NW. It is notable that the peaks at both ends are located within the spectral range of the two non-mixed perovskites but are asymmetrically shifted toward the green peak. It is also remarkable that a slight shift appears in the Cl-rich region when compared to its Br-rich counterpart which is increasingly evident when moving the laser to the opposite end (see Fig. S4).

The lifetime spectrum of the heterojunction as a function of temperature, illustrated in Fig. 4, was analyzed using a bi-exponential decay model. A least squares method was used to fit the biexponential model using the function $f(t) = y_0 + A_1 e^{-C_1 t} + A_2 e^{-C_2 t}$. The range used was from the beginning of the intensity decay to the very end of the measured time interval. The fitting iteration was stopped when χ^2 residue less than 10^{-9} has been reached. This analysis revealed the presence of two distinct excitonic recombination channels, labeled as P1 and P2. Many studies employ multiexponential fitting procedures due to the passivated nature of their samples [17–21]; however, our samples were unpassivated. The P1 channel, representing the slower recombination process, exhibited a stable lifetime across the examined temperature range. In contrast, the P2 channel, corresponding to the faster process, demonstrated a significant increase in lifetime at the phase transition temperature of approximately 305 K (see values in Table S1 in the Supplementary Materials).

This enhancement was nearly threefold compared to the average

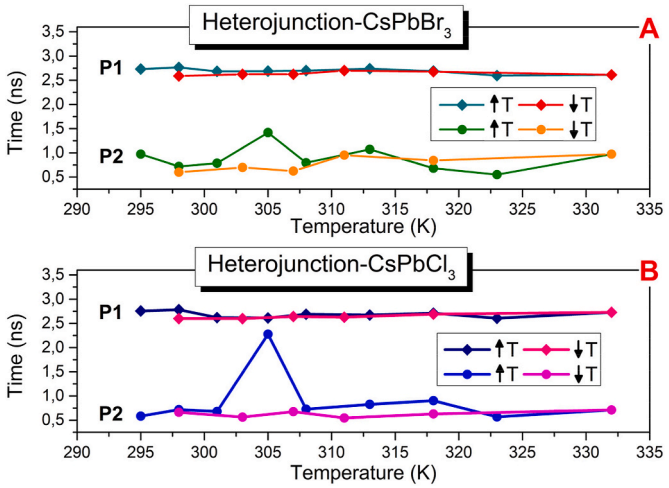

Fig. 4. Lifetime of the 2 luminescent processes (P1 and P2) present in the CsPb$(Br_{1-x}Cl_x)_3$ heterojunction NW for different temperatures during heating. Measurements in (A) were performed in the Br-rich half, while (B) shows the Cl-rich half.

exciton lifetime at other temperatures studied, emphasizing the impact of crystallographic phase transitions on exciton dynamics (see Fig. S11). In addition to the lifetime changes, the relative contribution of each recombination channel—evaluated through the integrated area under the fitted decay components—also revealed a temperature-dependent behavior.

The non-radiative channel (P2) dominates across most of the temperature range, but near the presumed phase transition temperature, a notable modulation in the radiative channel (P1) occurs. This suggests that structural reorganization during the probably phase transition temporarily alters the balance between radiative and non-radiative pathways, possibly due to changes in exciton confinement or the formation of ferroelastic domains. To confirm the reproducibility of these findings, multiple heating cycles were performed on the same NW as well as on additional heterostructured NWs, consistently replicating the observed effects. The data from one typical cycle are presented in the main text, and the results from one additional cycle are detailed in Fig. S9 in the Supplementary Material, illustrating the stability and repeatability of the exciton lifetime enhancement at the phase transition.

The behavior of the central position of the green luminescence peak can be seen in Fig. 5 for pure $CsPbBr_3$ and for the heterostructure CsPb$(Br_{1-x}Cl_x)_3$ NW during heating and cooling processes (both can be seen in more detail in the Supplementary Material in Figs. S6, S7, S8 and S9). The PL values remain nearly constant for $CsPbBr_3$ for temperature up to around 350 K, when a blue shift takes place. This temperature matches with the orthorhombic to tetragonal phase transition seen for pure $CsPbBr_3$ NWs in different works [7]. Subsequently with the blue shift, the peak center is red shifted back towards green at around 360 K. It was shown before that $CsPbBr_3$ NWs can present stepped transition temperatures for different domains, which may be induced by strain inhomogeneity along the crystal [8]. This phenomenon, by itself, may induce extra strain along the NW, once the new lattice is forced to accommodate orthorhombic and tetragonal domains together. As the temperature keeps increasing, new domains suffer phase transitions, and the lattice is relaxed. Oscillations in the PL peak center near the nominal transition temperature may be explained by the partial transitions along this NW. In contrast with the pristine nanostructure, the CsPb$(Br_{1-x}Cl_x)_3$ heterojunction NW shows a red shift at around 305 K, and then a plateau during heating up to 335 K. A smooth blue shift can be seen along the whole cooling curve, indicating hysteresis in the process. Cycles were also repeated both for the pristine and for the heterostructured NWs.

4. Discussion

Before we start our analysis, we must point out that our samples have a volume of roughly a half cubic micron. Such characteristic is distinct

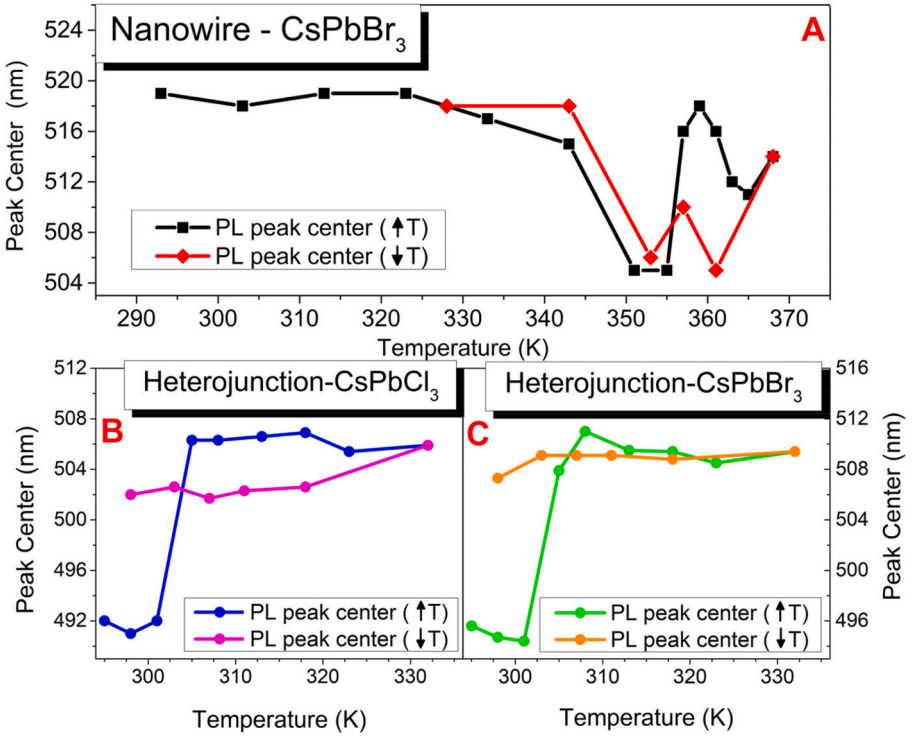

Fig. 5. Curves of the PL peak center of the luminescence as a function of temperature. In (A) we show measurements for the $CsPbBr_3$ NW, while results for the heterojunction NW are shown in (B) for the Cl-rich half, and in (C) for the Br-rich half. Peak center error bars are smaller than point sized for all graphs.

from usual perovskite nanocrystals (either purely inorganic or hybrid) obtained through wet chemistry, which are nanometer-sized and have less than a millionth of a cubic micron [22]. In that sense, surface effects, such as those associated with surface defects, have a minor role on the overall optoelectronic properties [22,23]. Moreover, although metal-halide perovskites generally have many structural defects, it can be lowered by the epitaxial growth used in our case [24,25]. Finally, we focus our attention on the crystallographic phase transitions, rather than the crystallographic phase itself. For the pure $CsPbBr_3$ NW, the investigated phase transition studied in this work, from orthorhombic to tetragonal, is expected to occur at T = 361 K [26]. For the pure $CsPbCl_3$ NW, the corresponding phase transition takes place at T = 305 K [27]. The $CsPb(Br_{1-x}Cl_x)_3$ heterostructure is expected to show phase transitions around these values. It is important to notice that actual transition temperature can be shifted in nanostructures due to, among other reasons, residual strain inhomogeneities along the structure [7,8]. We have chosen these phase transitions because several works had unambiguously shown these as well determined phase transition processes through different experimental techniques [28,29].

Phase transitions of $CsPbBr_3$ and $CsPbCl_3$ are well described in the literature and were explored in detail along the past decades [30,31]. Critical temperatures referenced in past works are valid for bulk crystals but can be shifted in nanostructures, where surface conditions represent a relatively larger fraction of the studied perovskite materials [8,32]. Micro-PL cannot unambiguously determine the local crystal phase, but it is often used to infer changes in the crystalline structure [33]. We hypothesize that, in the studied nanowires, small surface lattice changes induce a relevant modification of the observed PL signal, requiring further structural investigation of nanometric surface-sensitive probes to ensure a robust phase description.

First, PL signals retrieved from the studied samples show that both sides of the $CsPb(Br_{1-x}Cl_x)_3$ heterojunction NW show emission peaks towards the green region even when excited at $\lambda_{exc} = 371$ nm (Fig. 3(A)). This indicates that charge carriers have a large mean free path, with electrons and holes involved in the heterojunction diffusing from the larger bandgap region (Cl-rich half) to the narrower bandgap of the NW portion (Br-rich half), most likely with the energy diffusion being enhanced by photon recycling [34,35]. Therefore, changes in charge transport of any of the halves of the $CsPb(Br_{1-x}Cl_x)_3$ heterojunction NW are perceived in the PL signal of the other half.

Recent findings demonstrate that the introduction of HCl vapor leads to notable changes in the lattice parameters and induces ferroelastic domains within $CsPb(Br_{1-x}Cl_x)_3$ heterostructured NWs. These structural transformations are closely linked to variations

in local anion composition, which significantly influence the photoluminescent properties of the NWs. This aligns with our observations of enhanced exciton lifetimes and altered photoluminescence peak positions, suggesting that the ferroelastic and possibly flexoelectric properties induced by anion exchange play a critical role in the optoelectronic behavior of these materials [36]. Additionally, recent studies have shown that exposing $CsPb(Br_{1-x}Cl_x)_3$ NWs to Cl_2 gas via an $Ar-Cl_2$ atmosphere results in similar structural and photoluminescent modifications [37]. These findings highlight that, regardless of the Cl source, whether HCl vapor or Cl_2 gas, the induced ferroelastic domains and altered electronic properties are significant for understanding and enhancing the performance of perovskite-based optoelectronic devices.

Recent studies have demonstrated the flexoelectric effect in metal halide perovskites (MHPs), describing how strain gradients can induce polarization in these materials. For instance, research on all-inorganic $CsPbBr_3$ nanocrystals has shown that strain gradients generated during epitaxial growth can lead to polarization effects, highlighting the flexoelectric response intrinsic to these systems [6]. These findings are particularly relevant for $CsPb(Br_{1-x}Cl_x)_3$ heterostructures, as similar strain-induced polarization phenomena may play a crucial role in their optoelectronic properties, potentially influencing charge transport and exciton dynamics under varying thermal conditions.

Furthermore, theoretical approaches have been developed to isolate flexoelectric contributions from piezoelectric effects in perovskite oxides, highlighting the intrinsic flexoelectric response independent of other electromechanical interactions [38,39]. This distinction is crucial for accurately understanding the underlying mechanisms in $CsPbX_3$ perovskites where complex interactions between lattice strain and electronic properties occur.

Additionally, molecular dynamics simulations have provided insights into how bending and strain gradients can influence the polarization within perovskite structures, indicating a proportional relationship between curvature and polarization [40]. These findings are particularly relevant for explaining the observed changes in luminescence and carrier dynamics in $CsPb(Br_{1-x}Cl_x)_3$ NWs, as the flexoelectric effects could enhance carrier separation and reduce recombination at the interfaces or within strain-graded regions of the NW.

Given the dimensions of the grown NW used in this study (see Supplementary Material), one could not simply argue that quantum confinement effects on the charge carriers, either for electrons or holes, is of utmost importance for the observed bandgap increase compared to bulk $CsPbX_3$ [41]. It was recently demonstrated, however, the formation of ferroelastic domains in similar MHPs nanostructures and its dynamics over temperature variation and crystal phase transitions [7–10].

Previous studies have demonstrated the emergence of ferroelastic domains in $CsPbX_3$ nanostructures as a function of temperature and pressure changes [7,8,36,37]. These domains typically appear in an ordered and reversible manner, propagating strain throughout the nanowire due to lattice parameter mismatches at the domain wall interfaces.

This effect is intrinsically linked to the orthorhombic crystal structure, which facilitates ferroelasticity [7,8]. However, the precise mechanisms governing domain pinning remain unclear. It is not yet determined whether structural defects act as pinning sites, whether domain periodicity arises purely from strain propagation, or if both effects contribute simultaneously. In mixed-halide nanowires, where a chemical gradient is already present, similar domain formations have been observed even at room temperature, suggesting that additional factors may influence their stability [36]. These observations further highlight the need for a more detailed model to explain how ferroelastic domains influence charge carrier dynamics in MHPs, particularly across phase transition temperatures. The effect of ferroelastic domains on the basic physical properties, and a model explaining how they can affect charge carries in MHPs over the phase transitions temperature range, is up to be discussed.

About a decade ago, strain-induced low dimensional confined structures based on a single material were proposed (not based on either piled heterojunctions or on chemically distinct layer-by-layer growth). Those confined structures, similar to heterostructures and superlattices, could be obtained by applying strain spatially to a single material in a periodic or aperiodic way [42]. Based on this previous work, we can propose a mechanism by means of a model that is discussed below.

Recent works predict that the bandgap of bulk $CsPbX_3$ perovskites depend on the strain [43–45]. Thus, alternated-strain layer configuration in $CsPbX_3$ could form a superlattice-like potential for electrons in local conduction band (CB) and holes in local

valence band (VB), which is imposed by the local electrochemical potential. This potential distorts the electronic structure producing an effective bandgap, the magnitude of which depends on the amount of strain present in that specific region on NW (Fig. 6). Additionally, given that the spatial periodicity of ferroelastic domains, this existence of different domains with varying degrees of strain results in a physical behavior that resembles a disordered superlattice. Disordered superlattices have the interesting characteristic of increasing Anderson localization of charge carriers which, in turn, enhances the exciton recombination rate, which can be observed in luminescence, and may shift emission spectra depending on the amount of localization caused

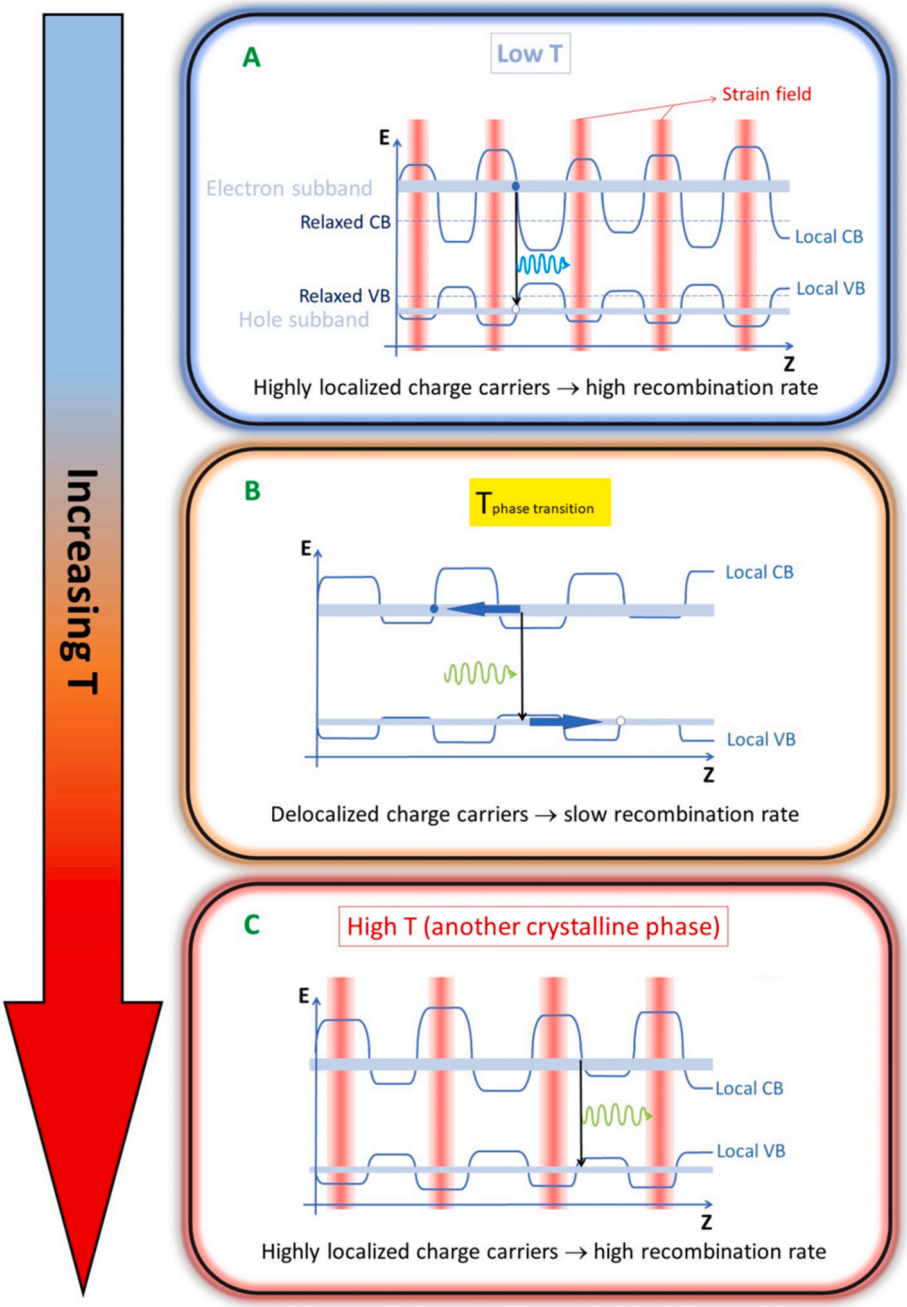

Fig. 6. Schematic evolution of the electronic band structure as a function of the position along the NW growth direction. The temperature increases from the top to the bottom panel. Precisely at the phase transition, the charge carriers have the largest mean free path along the growth axis. The boxes show the electronic band structure for (A) low temperature, (B) at the temperature in which the probable phase transition occurs and (C) a higher temperature.

[46,47].

This phenomenon has been originally studied on III-V semiconductor systems, and here we exploit the model for perovskites.

Based on the observed hysteresis phenomenon during thermal cycling, as evidenced by the shift of the PL peak center at the heterojunction of a NW, it seems that, for the $CsPb(Br_{1-x}Cl_x)_3$ NWs, after the reordering of the ferroelastic domains, the spatial periodicity of the disordered strain superlattice is altered to what seems a different crystallographic phase, which may take place due to a stoichiometric change where Cl is lost to the environment due to the heating process. It is important to emphasize that this model assumes a crystal phase transition expected near 305 K for $CsPbCl_3$ [48], as well as the formation of ferroelastic domains at the critical temperature, which cannot be directly inferred by our measurements but has been observed before for similar systems [7,8]. This process changes the exciton recombination energy (Fig. 3(A) and (B)). This is in agreement with a previous study which showed that $CsPbCl_3$ exhibits a hysteretic behavior related to charge transport when heated and cooled between 305 and 325 K [27].

At the same time, the flexoelectric effect is reduced at the phase transition temperature due to the smearing of the strain gradient caused by the reordering, as illustrated in Fig. 6. In turn, this smearing out of polarization dynamics at the precise juncture of the phase transition causes an increase of mean free path of charge carriers and consequently an increase of exciton lifetime, also observed in the heterojunction NW. In fact, a work by Lee et al. showed the feasibility of fabricating a device using flexoelectric rectification of charge transport in strain-graded dielectrics [49].

Concerning the $CsPb(Br_{1-x}Cl_x)_3$ heterojunction NW, if a composition

gradient takes place along the NW axis, it can be expected that the Cl anion inward migration induces some degree of disorder in the NW lattice. This possibility is supported by the mechanical fragility observed by AFM in the resulting $CsPbCl_3$ (homogeneous) NW (see Supplementary Materials, Fig. S2, which shows the NW crumbling). Such effects influence the phase exhibited by that sample and its respective transition temperature.

However, according to theoretical works, for any value of x between 0 and 1, a lattice of $CsPb(Br_{1-x}Cl_x)_3$ is a stable solid solution with negligible chance of segregation [50].

5. Conclusion

In summary, we probed the PL and PL lifetime for $CsPb(Br_{1-x}Cl_x)_3$ NWs over temperature variation across expected crystal phase transition temperatures. NWs with

$x = 0$, $x = 1$ and a heterostructure were studied. Our results indicate increased PL lifetime near an expected phase transition for pure $CsPbCl_3$. A theoretical model used to explain the phenomenon indicates that the mean free path of charge carriers may be enlarged at the crystalline phase transitions of $CsPb(Br_{1-x}Cl_x)_3$ perovskites at modest temperatures above room temperature. Besides the influence on charge carrier temporal evolution, a shift in the PL peak is also observed during phase transitions.

This happens regardless of the chemical composition (x between 0 and 1) of the MHP. Flexoelectricity may be generated by electronic band edge spatial modulation (adiabatic approximation of the electrochemical potential) caused by strain gradient of the ferroelastic domain walls. Understanding the phenomenon could help to improve perovskite-based photovoltaic devices, especially for operating in light concentration setups above room temperature.

CRediT authorship contribution statement

E. Pereira-Andrade: Writing – review & editing, Writing – original draft, Visualization, Validation, Methodology, Investigation, Formal analysis, Data curation, Conceptualization. **M.V.H. Machado:** Writing – original draft, Visualization, Validation, Investigation. **N. Lamers:** Writing – review & editing, Writing – original draft, Validation, Resources, Methodology, Investigation. **Z. Huang:** Writing – review & editing, Writing – original draft, Visualization, Validation, Methodology, Investigation. **J. Wallentin:** Writing – review & editing, Writing – original draft, Visualization, Validation, Supervision, Resources, Methodology, Investigation, Funding acquisition. **A. Malachias:** Writing – review & editing, Writing – original draft, Visualization, Validation, Resources, Methodology, Investigation, Formal analysis, Data curation. **L.A. Cury:** Writing – original draft, Visualization, Validation, Supervision, Resources, Methodology, Investigation, Funding acquisition, Formal analysis, Data curation, Conceptualization. **L.A.B. Marçal:** Writing – review & editing, Writing – original draft, Visualization, Validation, Supervision, Resources, Methodology, Investigation, Formal analysis, Conceptualization. **G.A.M. Sáfar:** Writing – review & editing, Writing – original draft, Visualization, Validation, Supervision, Project administration, Methodology, Investigation, Funding acquisition, Formal analysis, Data curation, Conceptualization.

Funding

This project has received funding from PRPq/PRPG (UFMG/Brazil), CNPq (Brazil), CAPES (Brazil), FAPEMIG (Brazil), the European Research Council (ERC) under the European Union's Horizon 2020 research and innovation program and from the Olle Engkvist foundation, NanoLund, and Marie Sklodowska Curie Actions Cofund.

Declaration of competing interest

The authors declare no conflict of interest.

Acknowledgments

We thank CNPq (Brazil), CAPES (Brazil) and FAPEMIG (Brazil) for financial resources and LCPNano for its facilities. This project has received funding from the European Research Council (ERC) under the European Union's Horizon 2020 research and innovation program (Grant Agreement No. 801847). This research was also funded by the Olle Engkvist foundation, NanoLund, and Marie Sklodowska Curie Actions Cofund, Project INCA 600398.

Appendix A. Supplementary data

Supplementary data to this article can be found online at https://doi.org/10.1016/j.solidstatesciences.2025.108043.

Data availability

Data will be made available on request.

References

[1] F. Ambrosio, F. De Angelis, A.R. Goni, The ferroelectric-ferroelastic debate about metal halide perovskites, J. Phys. Chem. Lett. 13 (2022) 7731–7740, https://doi.org/10.1021/acs.jpclett.2c01945.
[2] B.Y. Huang, Z.H. Liu, C.W. Wu, Y. Zhang, J.J. Zhao, X. Wang, J.Y. Li, Polar or nonpolar? That is not the question for perovskite solar cells, Natl. Sci. Rev. 8 (2021) nwab094, https://doi.org/10.1093/nsr/nwab094.
[3] X. Li, S.Q. Chen, P.F. Liu, Y.L. Zhang, Y. Chen, H.L. Wang, H.M. Yuan, S.H. Feng, Evidence for ferroelectricity of all-inorganic perovskite CsPbBr3 quantum dots, J. Am. Chem. Soc. 142 (2020) 3316–3320, https://doi.org/10.1021/jacs.9b12254.
[4] H. Rohm, T. Leonhard, A.D. Schulz, S. Wagner, M.J. Hoffmann, A. Colsmann, Ferroelectric properties of perovskite thin films and their implications for solar energy conversion, Adv. Mater. 31 (2019) 1806661, https://doi.org/10.1002/adma.201806661.
[5] I. Mela, C. Poudel, M. Anaya, G. Delport, K. Frohna, S. Macpherson, T.A.S. Doherty, A. Scheeder, S.D. Stranks, C.F. Kaminski, Revealing nanomechanical domains and their transient behavior in mixed-halide perovskite films, Adv. Funct. Mater. 31 (2021) 2100293, https://doi.org/10.1002/adfm.202100293.
[6] L.L. Shu, et al., Photoflexoelectric effect in halide perovskites, Nat. Mater. 19 (2020) 605, https://doi.org/10.1038/s41563-020-0659-y.
[7] L.A.B. Marcal, E. Oksenberg, D. Dzhigaev, S. Hammarberg, A. Rothman, A. Bjorling, E. Unger, A. Mikkelsen, E. Joselevich, J. Wallentin, In situ imaging of temperature-dependent fast and reversible nanoscale domain switching in a single-crystal perovskite, Phys. Rev. Mater. 6 (2022) 054408, https://doi.org/10.1103/PhysRevMaterials.6.054408.
[8] L.A.B. Marcal, D. Dzhigaev, Z.J. Zhang, E. Sanders, A. Rothman, E. Zatterin, E. Bellec, T.U. Schulli, A. Mikkelsen, E. Joselevich, J. Wallentin, In situ imaging of ferroelastic domain dynamics in CsPbBr3 perovskite nanowires by nanofocused scanning X-ray diffraction, ACS Nano 14 (2020) 15973–15982, https://doi.org/10.1021/acsnano.0c07426.
[9] L.A.B. Marcal, et al., Inducing ferroelastic domains in single-crystal CsPbBr3 perovskite nanowires using atomic force microscopy, Phys. Rev. Mater. 5 (2021) L063001, https://doi.org/10.1103/PhysRevMaterials.5.L063001.
[10] D. Dzhigaev, Z.J. Zhang, L.A.B. Marcal, S. Sala, A. Bjorling, A. Mikkelsen, J. Wallentin, Three-dimensional coherent x-ray diffraction imaging of ferroelastic domains in single CsPbBr3 perovskite nanoparticles, New J. Phys. 23 (2021) 063035, https://doi.org/10.1088/1367-2630/ac02e0.
[11] J. Shi, H. Zhang, Y. Li, J.J. Jasieniak, Y. Li, H. Wu, Y. Luo, D. Li, Q. Meng, Identification of high-temperature exciton states and their phase-dependent trapping behaviour in lead halide perovskites, Energy Environ. Sci. 11 (2018) 1460–1469, https://doi.org/10.1039/c7ee03543h.
[12] E. Parrott, R. Milot, T. Stergiopoulos, H. Snaith, M. Johnston, L. Herz, Effect of structural phase transition on charge-carrier lifetimes and defects in CH3NH3SnI3 perovskite, J. Phys. Chem. Lett. 7 (2016) 1321–1326, https://doi.org/10.1021/acs.jpclett.6b00322.
[13] S. Gautam, M. Kim, D. Miquita, J. Bouree, B. Geffroy, O. Plantevin, Reversible photoinduced phase segregation and origin of long carrier lifetime in mixed-halide perovskite films, Adv. Funct. Mater. 30 (2020) 2002622, https://doi.org/10.1002/adfm.202002622.
[14] S. Ghasemi, S. Hosseini, F. Mousavi, Electrophoretic deposition of graphene nanosheets: a suitable method for fabrication of silver-graphene counter electrode for dye-sensitized solar cell, Colloids Surf. A Physicochem. Eng. Asp. 520 (2017) 477–487, https://doi.org/10.1016/j.colsurfa.2017.02.004.

[15] N. Lamers, Z.J. Zhang, I.G. Scheblykin, J. Wallentin, Gas-phase anion exchange for multisegment heterostructured CsPb(Br1-xClx)(3) perovskite nanowires, Adv. Opt. Mater. 12 (2023) 8, https://doi.org/10.1002/adom.202300435.
[16] N. Lamers, Z.J. Zhang, J. Wallentin, Perovskite-compatible electron-beam-lithography process based on nonpolar solvents for single-nanowire devices, ACS Appl. Nano Mater. 5 (2022) 3177–3182, https://doi.org/10.1021/acsanm.2c00188.
[17] J. Park, Y. Kim, S. Ham, J. Woo, T. Kim, S. Jeong, D. Kim, A relationship between the surface composition and spectroscopic properties of cesium lead bromide (CsPbBr3) perovskite nanocrystals: focusing on photoluminescence efficiency, Nanoscale 12 (2020) 1563–1570, https://doi.org/10.1039/c9nr08516e.
[18] D. Strandell, P. Kambhampati, Light emission from CsPbBr3 metal halide perovskite nanocrystals arises from dual emitting states with distinct lattice couplings, Nano Lett. 23 (2023) 11330–11336, https://doi.org/10.1021/acs.nanolett.3c03975.
[19] D. Strandell, D. Zenatti, P. Nagpal, A. Ghosh, D. Dirin, M. Kovalenko, P. Kambhampati, Hot excitons cool in metal halide perovskite nanocrystals as fast as CdSe nanocrystals, ACS Nano 18 (2023) 1054–1062, https://doi.org/10.1021/acsnano.3c10301.
[20] D. Strandell, D. Dirin, D. Zenatti, P. Nagpal, A. Ghosh, G. Raino, M. Kovalenko, P. Kambhampati, Enhancing multiexcitonic emission in metal-halide perovskites by quantum confinement, ACS Nano 17 (2023) 24910–24918, https://doi.org/10.1021/acsnano.3c06497.
[21] N. Yarita, H. Tahara, T. Ihara, T. Kawawaki, R. Sato, M. Saruyama, T. Teranishi, Y. Kanemitsu, Dynamics of charged excitons and biexcitons in CsPbBr3 perovskite nanocrystals revealed by femtosecond transient-absorption and single-dot luminescence spectroscopy, J. Phys. Chem. Lett. 8 (2017) 1413–1418, https://doi.org/10.1021/acs.jpclett.7b00326.
[22] G. Almeida, I. Infante, L. Manna, Resurfacing halide perovskite nanocrystals, Science 364 (2019) 833–834, https://doi.org/10.1126/science.aax5825.
[23] C. Li, Y. Li, T. Zhou, R. Xie, Ultrasonic synthesis of Mn-doped CsPbCl3 quantum dots (QDs) with enhanced photoluminescence, Opt. Mater. 94 (2019) 41–46, https://doi.org/10.1016/j.optmat.2019.04.053.
[24] C. Han, X. Xiao, W. Zhang, Q. Gao, J. Qi, J. Liu, Impact and role of epitaxial growth in metal halide perovskite solar cells,", ACS Mater. Lett. 5 (9) (2023-08-10 2023) 2445–2463, https://doi.org/10.1021/acsmaterialslett.3c00496.
[25] E. Shi, L. Dou, Halide perovskite epitaxial heterostructures, Acc. Mater. Res. 1 (2020) 213–224, https://doi.org/10.1021/accountsmr.0c00047.
[26] S. Svirskas, S. Balciunas, M. Simenas, G. Usevicius, M. Kinka, M. Velicka, D. Kubicki, M.E. Castillo, A. Karabanov, V.V. Shvartsman, M.D. Soares, V. Sablinskas, A.N. Salak, D.C. Lupascu, J. Banys, Phase transitions, screening and dielectric response of CsPbBr3, J. Mater. Chem. A 8 (2020) 14015–14022, https://doi.org/10.1039/d0ta04155f.
[27] M. Bruzzi, M. Latino, N. Falsini, N. Calisi, A. Vinattieri, Electrical and optical characterization of CsPbCl3 films around the high-temperature phase transitions, Nanomaterials 12 (2022) 570, https://doi.org/10.3390/nano12030570.
[28] S. Hirotsu, J. Harada, M. Iizumi, K. Gesi, Structural phase-transitions in CSPBBR3, J. Phys. Soc. Jpn. 37 (1974) 1393–1398, https://doi.org/10.1143/jpsj.37.1393.
[29] M.I. Cohen, K.F. Young, T.T. Chang, W.S. Brower, Phase transitions in CSPBCL3, J. Appl. Phys. 42 (1971) 5267, https://doi.org/10.1063/1.1659935.
[30] C. Stoumpos, et al., Crystal growth of the perovskite semiconductor CsPbBr3: a new material for high-energy radiation detection, Cryst. Growth Des. 13 (2013) 2722–2727, https://doi.org/10.1021/cg400645t.
[31] M.I. Cohen, K.F. Young, T.T. Chang, W.S. Brower, Phase transitions in CSPBCL3, J. Appl. Phys. 42 (1971) 5267, https://doi.org/10.1063/1.1659935.
[32] P. Cottingham, R. Brutchey, Depressed phase transitions and thermally persistent local distortions in CsPbBr3 quantum dots, Chem. Mater. 30 (2018) 6711–6716, https://doi.org/10.1021/acs.chemmater.8b02295.
[33] A. Dobrovolsky, A. Merdasa, E. Unger, A. Yartsev, I. Scheblykin, Defect-induced local variation of crystal phase transition temperature in metal-halide perovskites, Nat. Commun. 8 (2017-06-26 2017), https://doi.org/10.1038/s41467-017-00058-w. Art no. 34.
[34] J.H. Fu, S. Ramesh, J.W.M. Lim, T.C. Sum, Carriers, quasi-particles, and collective excitations in halide perovskites, Chemical Reviews, Early Acces (2023) 78, https://doi.org/10.1021/acs.chemrev.2c00843.
[35] L.M. Pazos-Outon, M. Szumilo, R. Lamboll, J.M. Richter, M. Crespo-Quesada, M. Abdi-Jalebi, H.J. Beeson, M. Vrucinic, M. Alsari, H.J. Snaith, B. Ehrler, R. H. Friend, F. Deschler, Photon recycling in lead iodide perovskite solar cells, Science 351 (2016) 1430–1433, https://doi.org/10.1126/science.aaf1168.
[36] L. Marçal, et al., Structural and chemical properties of anion exchanged CsPb(Br(1-x)Cl x)3 heterostructured perovskite nanowires imaged by nanofocused x-rays, Nanotechnology 35 (2024) 265710, https://doi.org/10.1088/1361-6528/ad355c.
[37] S. Hammarberg, L.A.B. Marcal, N. Lamers, Z. Zhang, H. Cheng, A. Bjorling, J. Wallentin, Nanoscale X-ray imaging of composition and ferroelastic domains in heterostructured perovskite nanowires: implications for optoelectronic devices, ACS Appl. Nano Mater. 6 (2023) 17698–17705, https://doi.org/10.1021/acsanm.3c02978.
[38] P. Zubko, G. Catalan, A. Tagantsev, Flexoelectric Effect in Solids, ANNUAL Review Of Materials Research 43 (2013) 387–421, https://doi.org/10.1146/annurev-matsci-071312-121634.
[39] J. Narvaez, F. Vasquez-Sancho, G. Catalan, Enhanced flexoelectric-like response in oxide semiconductors, Nature 538 (2016) 219, https://doi.org/10.1038/nature19761.
[40] L. Zhou, et al., Prediction of flexoelectricity in BaTiO3 using molecular dynamics simulations, Chin. Phys. B 32 (2023) 017701, https://doi.org/10.1088/1674-1056/ac70be.
[41] M.R. Amara, et al., Spectral fingerprint of quantum confinement in single CsPbBr3 nanocrystals, Nano Lett. 23 (2023) 3607–3613, https://doi.org/10.1021/acs.nanolett.3c00793.
[42] N. Sekkal, V.R. Velasco, Strain-induced low dimensional confinement structures, Appl. Phys. Lett. 93 (2008) 201104, https://doi.org/10.1063/1.3030981.
[43] M.R. Islam, A.A. Mazumder, M.R.H. Mojumder, A. Shifat, M.K. Hossain, Strain-induced tunable optoelectronic properties of inorganic halide perovskites APbCl(3) (A = K, Rb, and Cs), Jpn. J. Appl. Phys. 62 (2023) 011002, https://doi.org/10.35848/1347-4065/acb09e.
[44] R. Islam, K. Liu, Z.J. Wang, S. Hasan, Y.L. Wu, S.C. Qu, Z.G. Wang, Strain-induced electronic and optical properties of inorganic lead halide perovskites APbBr(3) (A = Rb and cs), Mater. Today Commun. 31 (2022) 103305, https://doi.org/10.1016/j.mtcomm.2022.103305.
[45] X.Y. Li, Y.Q. Luo, M.V. Holt, Z.H. Cai, D.P. Fenning, Residual nanoscale strain in cesium lead bromide perovskite reduces stability and shifts local luminescence, Chem. Mater. 31 (2019) 2778–2785, https://doi.org/10.1021/acs.chemmater.8b04937.
[46] K.A. Mader, L.W. Wang, A. Zunger, Electronic consequences of random layer-thickness fluctuations in alas/gaas superlattices, J. Appl. Phys. 78 (1995) 6639–6657, https://doi.org/10.1063/1.360728.
[47] T.C. Chang, W.K. Yeh, Y.J. Mei, W.C. Tsai, Y.F. Chen, Photoluminescence from ordered and disordered Si-SiGe superlattices, Opt. Quant. Electron. 28 (1996) 1295–1303, https://doi.org/10.1007/bf00326202.
[48] D. Tyagi, et al., Recent advances in two-dimensional perovskite materials for light-emitting diodes,", Discover Nano 19 (2024) 109, https://doi.org/10.1186/s11671-024-04044-2.
[49] D. Lee, S.M. Yang, J.G. Yoon, T.W. Noh, Flexoelectric rectification of charge transport in strain-graded dielectrics, Nano Lett. 12 (2012) 6436–6440, https://doi.org/10.1021/nl3038129.
[50] J.S. Bechtel, A. Van der Ven, First-principles thermodynamics study of phase stability in inorganic halide perovskite solid solutions, Phys. Rev. Mater. 2 (2018) 045401, https://doi.org/10.1103/PhysRevMaterials.2.045401.

Supplementary Material

Thermal Effects on the Dynamics of Excitons in $CsPb(Br_{1-x}Cl_x)_3$

E. Pereira-Andrade[1], M.V. H. Machado[1], N. Lamers[2], Z. Huang[2], J. Wallentin[2], A. Malac hias[1], L. A. Cury[1], L. A. B. Marçal[3], G. A. M. Sáfar[1*]

[1]Departamento de Física, Instituto de Ciências Exatas, Universidade Federal de Minas Gerais, Av. Antônio Carlos, 6627, Belo Horizonte, Minas Gerais, Brazil.

[2]Synchrontron Radiation Research and NanoLund, Lund University, Box 118, Lund22100, Sweden.

[3]Brazilian Synchrotron Light Laboratory (LNLS), Brazilian Center for Research in Energy and Materials (CNPEM), 13083-970, Campinas, Sao Paulo, Brazil

*Corresponding Author e-mail: safar@fisica.ufmg.br

Index

AFM measurements.....2

PL and TCSPC measurements.....5

AFM measurements

Atomic force microscopy (AFM) measurements were performed using a NanoSurfC3000 AFM system operating in tapping mode within a nitrogen-filled chamber, providing an inert atmosphere to control contamination and humidity during the measurements. The AFM data provided detailed insights into the morphology of the nanowires (NWs). The NWs exhibit an average length between 3 and 5 microns, with consistent surface features across the samples, reflecting the high quality of the synthesis process.

Figure S1 presents topographic AFM images of $CsPbBr_3$ NWs, demonstrating their uniform morphology, although one of the NWs (Figure S1 (c)) was found to be broken during the measurement process. This breakage may result from mechanical fragility induced by local structural strain, as discussed in the main text. Specifically, the presence of strain heterogeneities, commonly observed in perovskite structures, can generate internal stress that contributes to the mechanical degradation of these nanostructures under mechanical environmental influences.

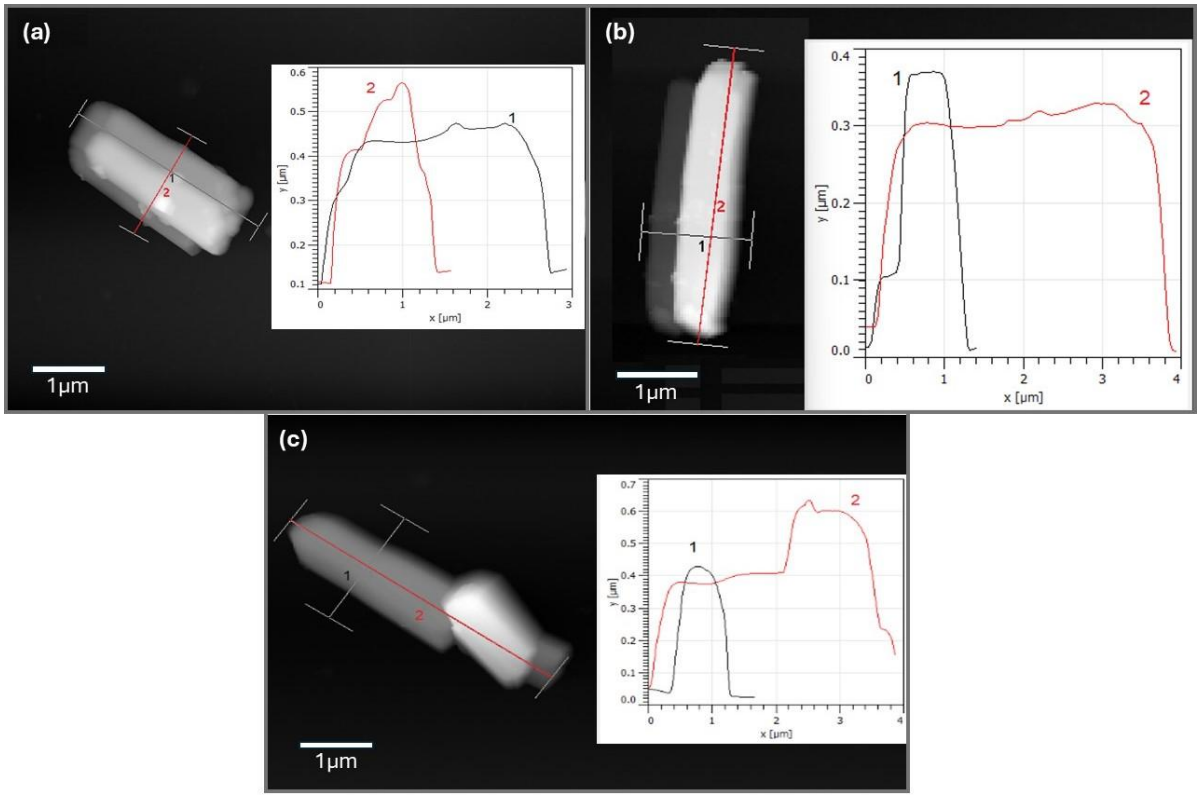

Figure S1.*Topographic AFM images of $CsPbBr_3$ NWs deposited on a Si_3N_4 substrate. (a) Image of a single $CsPbBr_3$ NW showing its smooth and uniform surface. (b) Another $CsPbBr_3$ NW displaying similar morphology, confirming the consistency in synthesis. (c) AFM image of a $CsPbBr_3$ NW that broke during measurement. The insets in each panel present the corresponding horizontal (1) and vertical (2) profiles, displaying the NWs' thicknesses and lengths, extracted using Gwyddion software.*

Figure S2 shows the topography of a $CsPbCl_3$ NW, which is obtained through a complete anion exchange process. In this process, the bromine (Br) ions in the original $CsPbBr_3$ NWs are entirely replaced by chlorine (Cl) ions, resulting in the transformation of the nanowire into

$CsPbCl_3$. The AFM images demonstrate the structural integrity of the exchanged NWs, with minimal surface defects, indicating successful exchange without compromising the morphology.

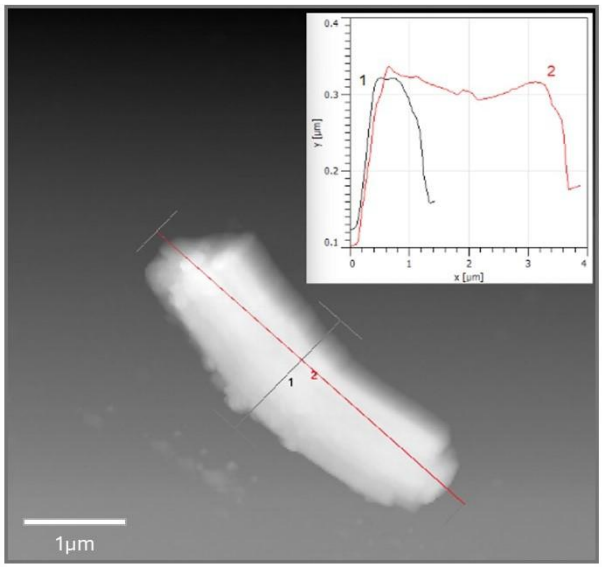

Figure S2.*Topographic AFM image of a $CsPbCl_3$ NW obtained through complete anion exchange, where Br ions in the original $CsPbBr_3$ NWs are replaced by Cl ions. The NW is deposited on a Si_3N_4 substrate, maintaining a smooth and uniform surface, indicative of the successful exchange process without compromising the structural integrity. The inset displays the horizontal (1) and vertical (2) profiles, showing the NW's thickness and length, extracted using Gwyddion software.*

Figure S3 presents AFM measurements of a partially modified NW, with one half composed of $CsPbBr_3$ and the other half of $CsPbCl_3$, forming a heterojunction. However, the topographic measurements do not reveal any visible changes or transitions along the interface between the two regions. The nanowire maintains a uniform structure and appearance throughout its length, further indicating that the anion exchange process does not compromise the surface morphology or structural integrity of the NW.

The insets of the AFM images display the vertical and horizontal profiles, illustrating the length and thickness of the nanowires. These profiles were extracted and analyzed using the data processing software Gwyddion, providing precise measurements of the NWs' dimensions and confirming the consistency of their morphology across the different samples.

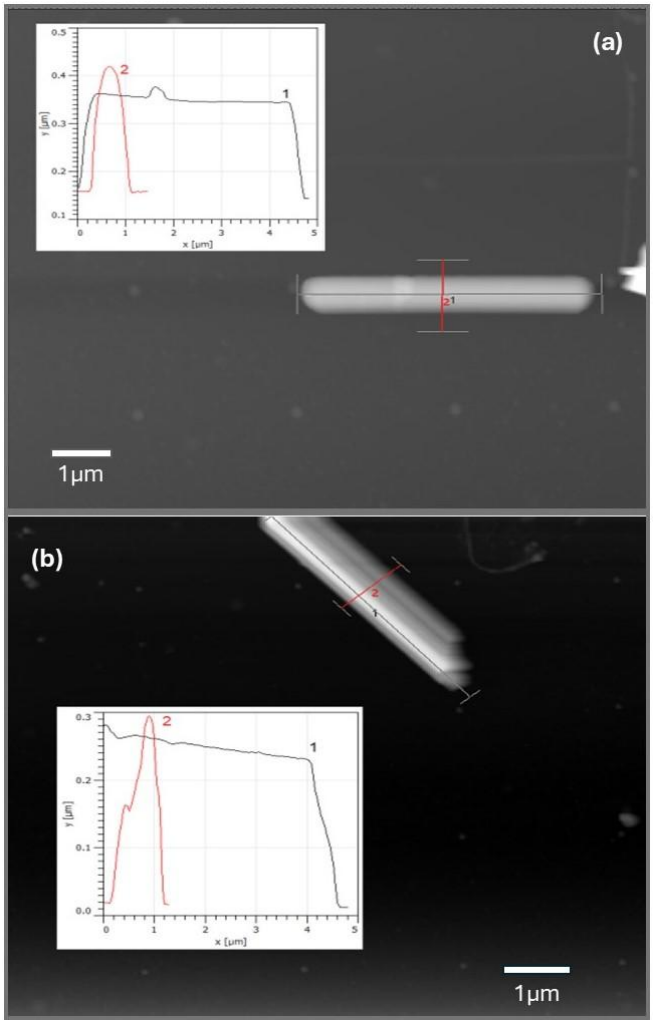

Figure S3.*Topographic AFM images of two different heterojunction nanowires (NWs) composed of* $CsPb(Br_{1-x}Cl_x)_3$*. (a) and (b) display NWs where one half consists of* $CsPbBr_3$ *and the other of* $CsPbCl_3$*. The AFM measurements reveal no visible topographic transitions along the interface. The insets in both panels show the horizontal (1) and vertical (2) profiles, highlighting the thickness and length of the NWs, obtained using Gwyddion software.*

PL and TCSPC measurements

Different setups were employed for the photoluminescence (PL) measurements to explore the optoelectronic properties of the NWs. The first setup utilized a micro-Raman Witec alpha300 RA Spectrometer, equipped with a confocal microscope and a 50x objective lens for precise optical analysis. For the measurements, a 457 nm excitation laser was used with a power of 0.5 mW, focused to a laser spot size of 0.3 µm. The motorized stage of the system enables precise spatial control, allowing high-resolution luminescence mapping. The combination of the small laser spot and confocal capabilities ensures localized excitation, which is essential for investigating the PL response in detail across different regions of the NWs, as described in the manuscript.

Figure S4(a) shows an optical microscope image of a heterojunction NW acquired using the Witec system. The luminescence mapping was performed with 0.15 µm step increments along the length of the NW, providing high spatial resolution to capture the variations in emission properties. Figures S4(b) and S4(c) present the resulting PL maps centered at 507 nm and 523 nm, respectively, each with a 2 nm bandwidth. These maps highlight the spatial variation in emission along the heterojunction NW, with the region corresponding to 507 nm emission being Cl-rich (Figure S4b), while the 523 nm emission region is Br-rich (Figure S4c).

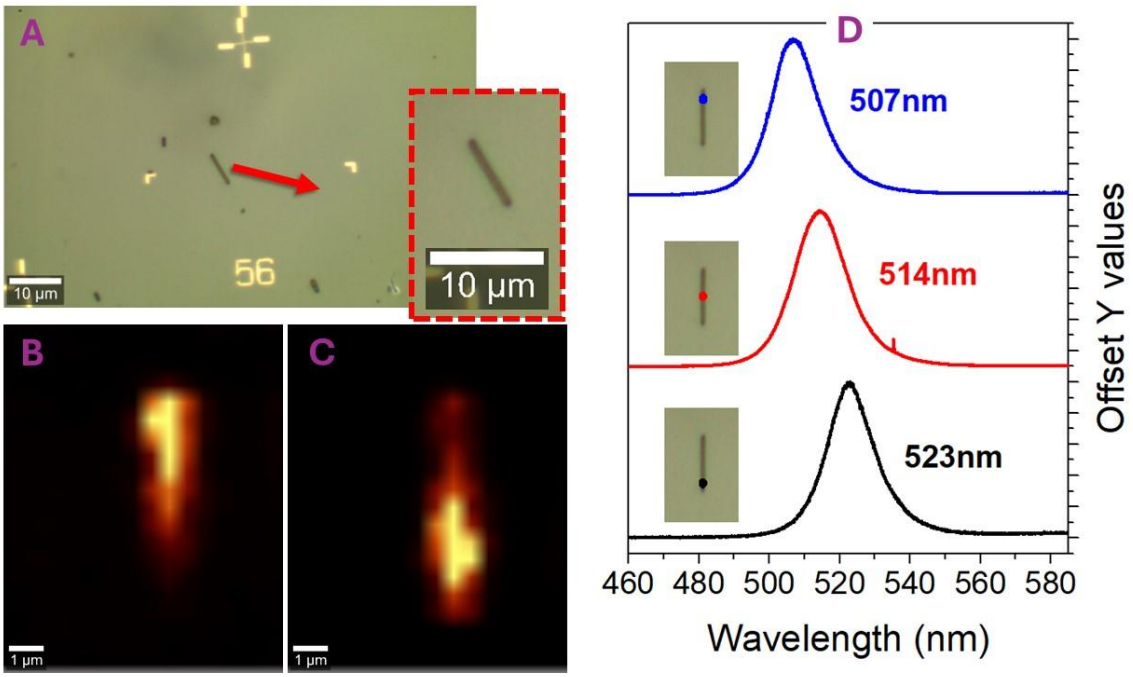

Figure S4. *(A) Optical microscope image of a heterojunction NW obtained using the Witec system. The inset shows a zoomed-in view of the same NW. (B) and (C) Luminescence maps of the heterojunction NW, centered at 507 nm and 523 nm, respectively, with a bandwidth of 2 nm. (D) Micro-PL spectra collected at different locations along the NW: the Cl-rich region (blue, 507 nm), the center of the NW (red, 514 nm), and the Br-rich region (black, 523 nm). These measurements highlight the compositional gradient along the NW, resulting in a gradual redshift in the emission peaks.*

Figure S4(d) displays micro-PL spectra collected at different locations along the NW. The blue spectrum, taken from the Cl-rich region, shows a PL peak centered at 507 nm. The red spectrum, obtained from the center of the NW, exhibits a peak at 514 nm, while the black spectrum, from the Br-rich end, presents a peak centered at 523 nm. This progressive redshift along the NW reflects the compositional gradient resulting from the anion exchange process.

As explained in the manuscript, this shift occurs due to the modulation of the electronic bandgap along the heterojunction. The narrower bandgap in the Br-rich region leads to longer wavelength emission, whereas the wider bandgap in the Cl-rich region produces shorter wavelength emission. These results confirm that the band structure of the NW is effectively tuned by the anion composition, influencing excitonic recombination dynamics and resulting in distinct PL emissions along the heterojunction.

The second setup, shown schematically in Figure S5, was employed for both steady-state PL and time-correlated single photon counting (TCSPC) measurements. For steady-state PL measurements, a continuous-wave 371 nm laser is used, while for TCSPC measurements, a pulsed 371 nm laser with a repetition rate of 80 MHz and a laser spot size of 0.5 μm is employed. The sample is mounted on a controllable heating stage, allowing precise temperature variation during the experiments, enabling the investigation of the temperature dependence of the photophysical properties of the NWs.

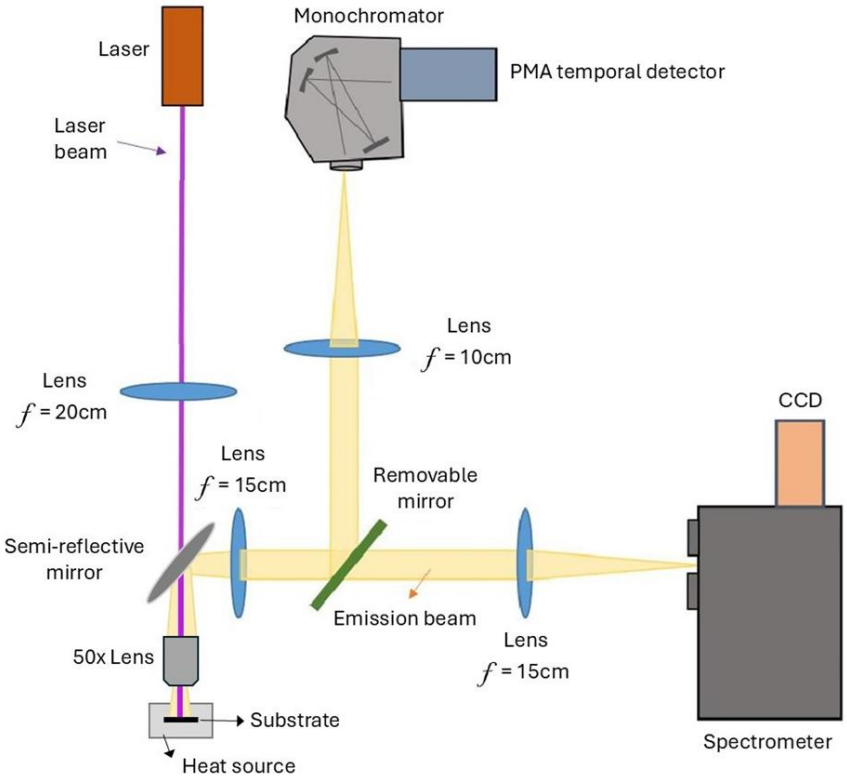

Figure S5. *Schematic representation of the optical setup used for steady-state PL and TCSPC measurements. The system utilizes either a continuous-wave 371 nm laser for PL measurements or a pulsed 371 nm laser (80 MHz repetition rate) for TCSPC. The laser beam is directed through several optical components, including lenses (focal lengths of 10 cm, 15 cm, and 20 cm) and a semi-reflective mirror, before focusing on the sample via a 50x objective lens. For PL measurements, the emission signal by passes the removable mirror and is sent directly to the ANDOR-Shamrock-303i spectrometer. In TCSPC mode, the removable mirror redirects the signal through an Oriel-MS125TM spectrograph to a PMA-M photomultiplier detector assembly, with an instrument response function of approximately 120 ps.*

The emission beam passes through several optical components, including lenses with focal lengths of 10 cm, 15 cm, and 20 cm, a semi-reflective mirror, and a removable mirror. Depending on the measurement, the removable mirror directs the emission either to the ANDOR-Shamrock-303i spectrometer for steady-state PL measurements or to an Oriel-

MS125TM spectrograph connected to a PMA-M photomultiplier detector assembly from PicoQuant for TCSPC measurements. The photomultiplier setup, with an instrument response function of approximately 120 ps, ensures precise time resolution for the TCSPC experiments. Before reaching the photomultiplier, the emission and any remaining laser light pass through a neutral filter to extinguish the excitation signal, ensuring that only the PL emission from the focal region of the 50x objective lens is detected. TCSPC data is collected using PicoHarp software and analyzed by fitting a bi-exponential decay model, following the equation$I(t) = A_1 e^{-t/\tau_1} + A_2 e^{-t/\tau_2}$ where A_1 and $A_2$are the exponential factors, and τ_1 and τ_2 are the fast and slow decay times, respectively.

To explore the temperature dependence of the PL response, $CsPbCl_3$ NWs were analyzed under varying temperatures using this setup. The PL spectra recorded across the temperature range, as shown in Figure S6 (left), reveal a progressive shift in the emission peak. A notable and abrupt change in the peak position occurs at the known phase transition temperature of $CsPbCl_3$, consistent with reports in the literature. The right panel of Figure S6 further quantifies this shift by plotting the PL peak center as a function of temperature, highlighting the significant influence of the phase transition on the optical properties of the material.

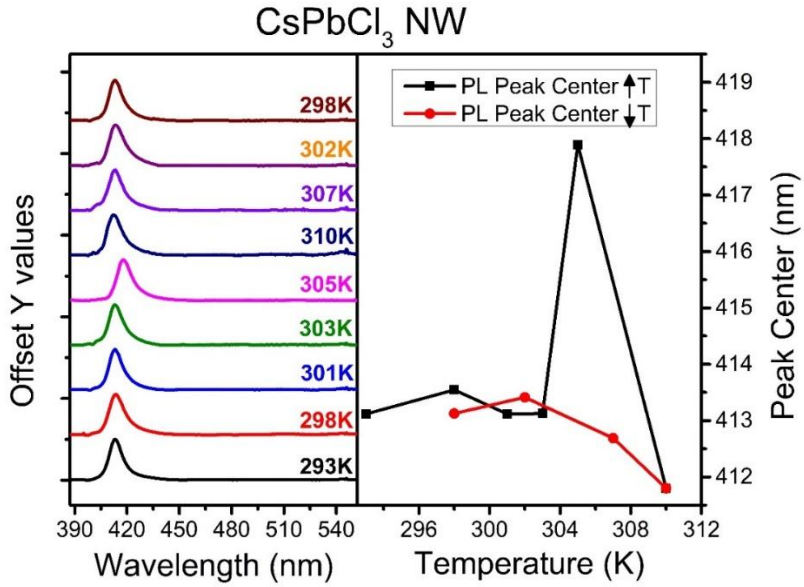

Figure S6. *(Left) PL spectra of a $CsPbCl_3$ nanowire (NW) measured using the second setup, with varying temperature. (Right) Variation of the PL peak center as a function of temperature, showing a significant shift at the known phase transition temperature of $CsPbCl_3$ reported in the literature.*

The heterojunction NWs were also studied to assess the thermal response of both the Cl-rich and Br-rich regions. For the Cl-rich region, Figure S7(a) shows the spectral evolution during heating, while Figure S7(b) presents the spectra obtained during cooling. A noticeable hysteresis effect is observed: the PL peak does not immediately return to its original position upon cooling, indicating that the optical response exhibits a memory effect. This suggests that structural or compositional rearrangements occur during the heating-cooling cycle, affecting the emission characteristics and resulting in a delayed return to the initial emission state.

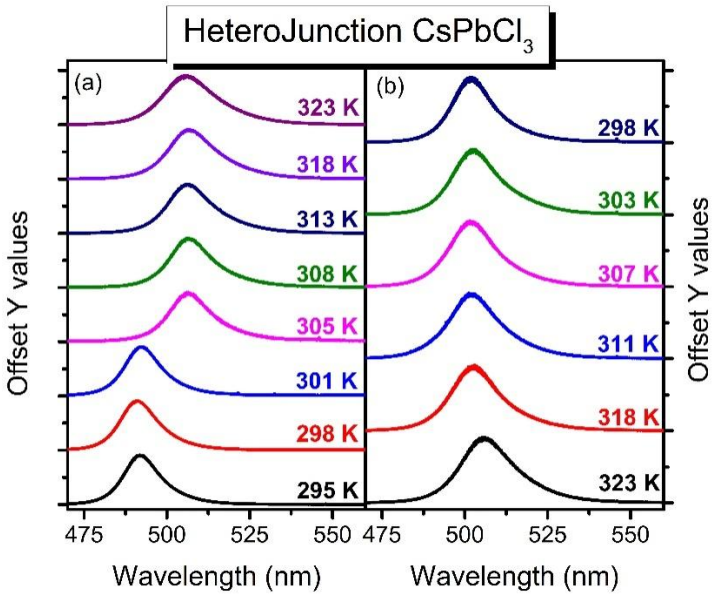

Figure S7. *PL spectra of the Cl-rich region of a heterojunction NW. (a) Evolution of the spectra during the heating process. (b) PL spectra collected during the cooling process, completing a full heating-cooling cycle.*

In the Br-rich region of the heterojunction NW, as shown in Figures S8(a) and S8(b), the PL spectra display a redshift during the heating process, similar to the behavior observed in the Cl-rich region. However, an intriguing feature is that despite the measurements being performed on the Br-rich part of the NW, a shift is still detected at the phase transition temperature associated with $CsPbCl_3$, mirroring the behavior seen in the Cl-rich region. This suggests that the optical response of the heterojunction is influenced by interactions between the two regions. One possible explanation for this behavior is photorecycling, where photon reabsorption and re-emission processes between the Br-rich and Cl-rich regions modulate the observed emission characteristics.

Temperature-dependent measurements were conducted across multiple thermal cycles and on different NWs to ensure the reproducibility and consistency of the observed behavior. Figure S9 presents the evolution of the PL peak center for the Cl-rich region of the heterojunction NW during a different thermal cycle, demonstrating the reliability of the results. The consistent shift observed in the peak position across multiple cycles further confirms the stability of the material's optical response and the robustness of the phase transition effect in $CsPbCl_3$. These repeatable trends highlight the coherence of the measurements, reinforcing the conclusion that the structural and optical changes induced by thermal cycling are intrinsic properties of the heterojunction nanowires.

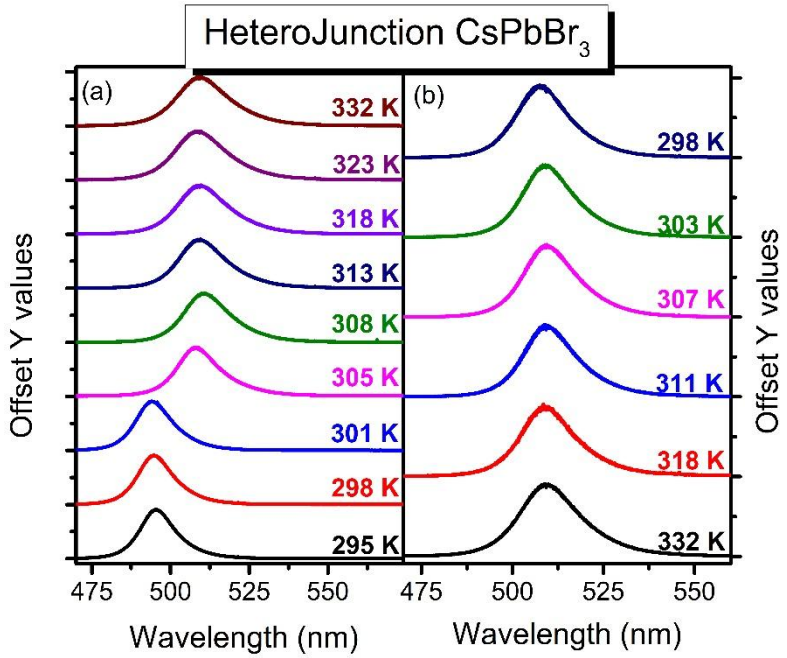

Figure S8. *PL spectra of the Br-rich region of a heterojunction NW. (a) Evolution of the spectra during the heating process. (b) PL spectra collected during the cooling process, completing a full heating-cooling cycle.*

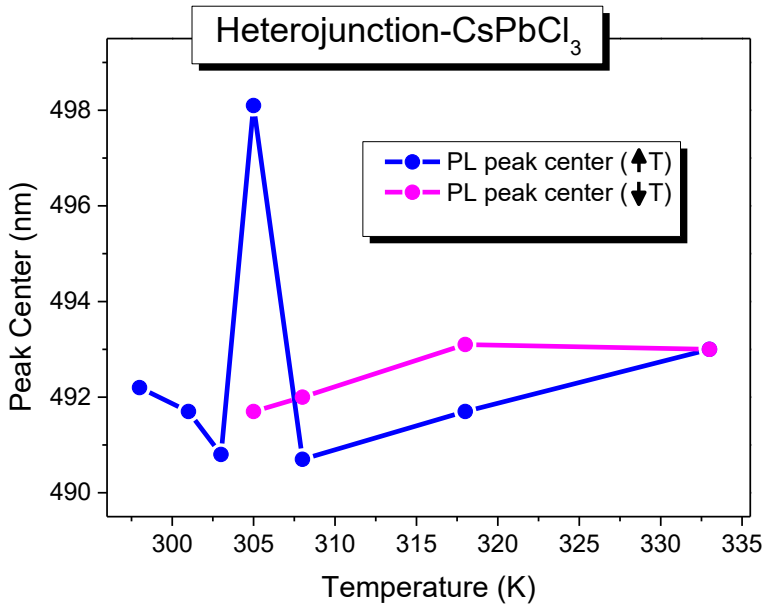

Figure S9. *Evolution of the PL peak center for the Cl-rich region of the heterojunction NW during a different thermal cycle, showing both the heating (blue) and cooling (pink) processes. The consistent behavior across cycles demonstrates the reproducibility and coherence of the PL response with temperature changes.*

To further investigate the temperature dependence of excitonic recombination dynamics, time-resolved PL measurements were performed on a $CsPbBr_3$ NW. Figure S10(a) presents the PL decay spectra collected over a range of temperatures, highlighting the changes in decay dynamics with increasing temperature. Figure S10(b) shows how the decay time

evolves across the measured temperatures. A pronounced change is observed near 361 K, corresponding to the known crystallographic phase transition temperature for $CsPbBr_3$ reported in the literature. This phase transition influences the excitonic behavior, reflected in the changes in decay dynamics as the temperature increases.

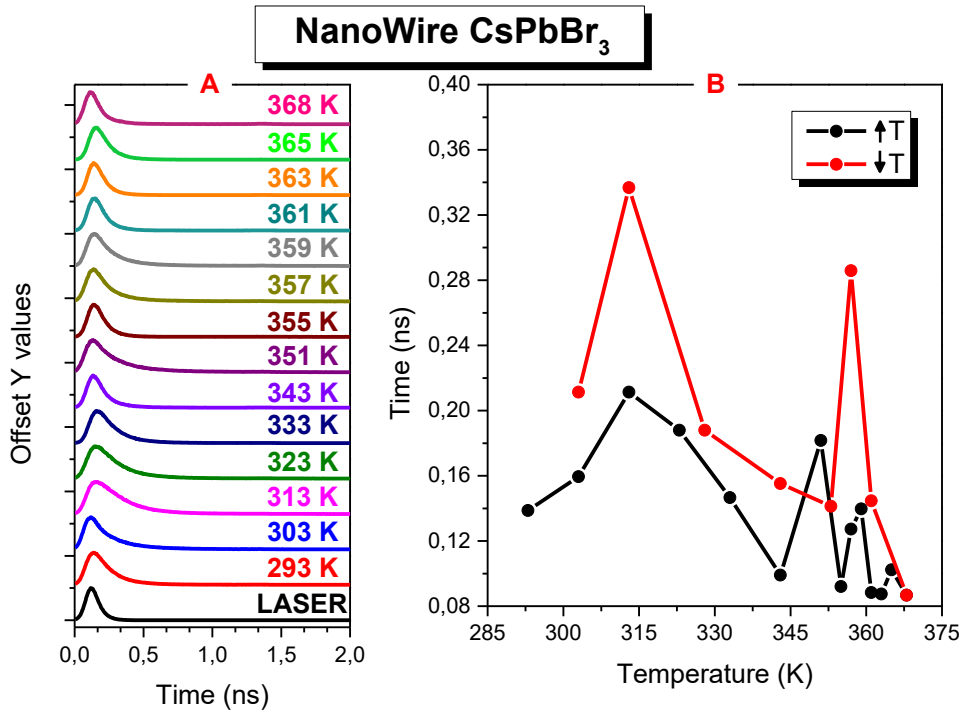

Figure S10. *(a) Time-resolved PL decay spectra of a $CsPbBr_3$ NW measured across different temperatures. (b) Decay time variation as a function of temperature, showing a significant change around 361 K, corresponding to the crystallographic phase transition of $CsPbBr_3$.*

Quantitative analysis of the decay processes for the heterojunction NW is summarized in Table S1. The left side of the table corresponds to the Br-rich region of the heterojunction, while the right side corresponds to the Cl-rich region. The two decay components, P1 and P2, represent distinct excitonic processes. According to the manuscript, P1 is associated with radiative excitonic recombination, while P2 corresponds to non-radiative recombination pathways. The average decay times for both P1 and P2 are provided, excluding the data point at 305 K (highlighted in gray) to eliminate the influence of the phase transition. At 305 K, corresponding to the phase transition temperature for the Cl-rich region, the decay time for P1 is 2.61 ns (very close to the average value of 2.67 ns), showing minimal alteration during the transition. However, a more pronounced change is observed for P2, which increases to 2.28 ns in the Cl-rich region, significantly deviating from the average of 0.68 ns. A similar, though smaller, effect is also observed in the Br-rich region, where P2 at 305 K is 1.42 ns, compared to the average value of 0.79 ns. These results highlight that while the radiative recombination (P1) remains relatively stable across the phase transition, the non-radiative recombination (P2) is strongly affected, particularly in the Cl-rich region, reflecting the structural rearrangements and affecting carrier recombination dynamics during the phase transition.

The trends in these decay processes are further illustrated in Figure S11, which is analogous to Figure 4 in the manuscript but includes black dotted lines representing the average decay time (excluding the 305 K point) to emphasize the differences in lifetime across temperatures. In Figure S11(a), the lifetime trends for the Br-rich region are shown, demonstrating a noticeable difference in lifetime compared to other temperatures, particularly near the transition temperature. Similarly, Figure S11(b) presents the lifetime trends for the Cl-rich region, providing a comparative perspective on the decay dynamics between the two regions of the heterojunction NW. These results underline the influence of temperature and phase transitions on excitonic recombination in both regions, offering insights into how composition and thermal effects modulate the optical properties of the heterojunction NWs.

Heterojunction-$CsPbBr_3$						**Heterojunction-$CsPbCl_3$**					
Temperature (K)	P_1 (ns)	A_1	P_2 (ns)	A_2	A_1/A_2	Temperature (K)	P_1 (ns)	A_1	P_2 (ns)	A_2	A_1/A_2
295	2.73	0.15	0.97	0.54	0.28	295	2.76	0.03	0.58	0.64	0.04
298	2.77	0.04	0.72	1.05	0.04	298	2.78	0.07	0.72	0.55	0.13
301	2.68	0.06	0.79	0.95	0.06	301	2.62	0.09	0.68	0.38	0.24
305	2.69	0.11	1.42	0.59	0.18	305	2.61	0.00	2.28	1.35	0.00
308	2.70	0.03	0.80	1.10	0.02	308	2.69	0.05	0.73	0.73	0.07
313	2.74	0.01	1.07	1.03	0.01	313	2.67	0.05	0.83	0.99	0.05
318	2.69	0.05	0.68	1.31	0.04	318	2.71	0.06	0.90	0.95	0.06
323	2.60	0.07	0.55	0.77	0.09	323	2.60	0.08	0.57	0.63	0.13
332	2.61	0.14	0.97	0.55	0.25	332	2.73	0.03	0.71	1.12	0.02
318	2.68	0.07	0.84	0.63	0.10	318	2.69	0.05	0.63	0.54	0.09
311	2.70	0.04	0.95	0.75	0.05	311	2.63	0.04	0.55	1.11	0.03
307	2.62	0.05	0.62	0.83	0.06	307	2.64	0.06	0.68	0.96	0.07
303	2.62	0.03	0.70	0.64	0.05	303	2.60	0.03	0.56	0.55	0.06
298	2.59	0.03	0.60	1.21	0.02	298	2.60	0.04	0.66	0.54	0.07
Average	2.67	0.06	0.83	0.85	0.09	Average	2.67	0.05	0.79	0.79	0.08

Table S1. *Bi-exponential decay fitting parameters for the Br-rich (left) and Cl-rich (right) regions of the heterojunction $CsPb(Br_{1-x}Cl_x)_3$ nanowires. P_1 corresponds to the radiative excitonic recombination channel, while P_2 represents non-radiative processes. A_1 and A_2 denote the integrated areas under each decay component, reflecting the total contribution of the radiative and non-radiative channels, respectively. The A_1/A_2 ratio indicates the relative strength of radiative emission compared to non-radiative losses. The data point at 305 K (highlighted in gray) corresponds to the temperature near the presumed phase transition and was excluded from the average calculation.*

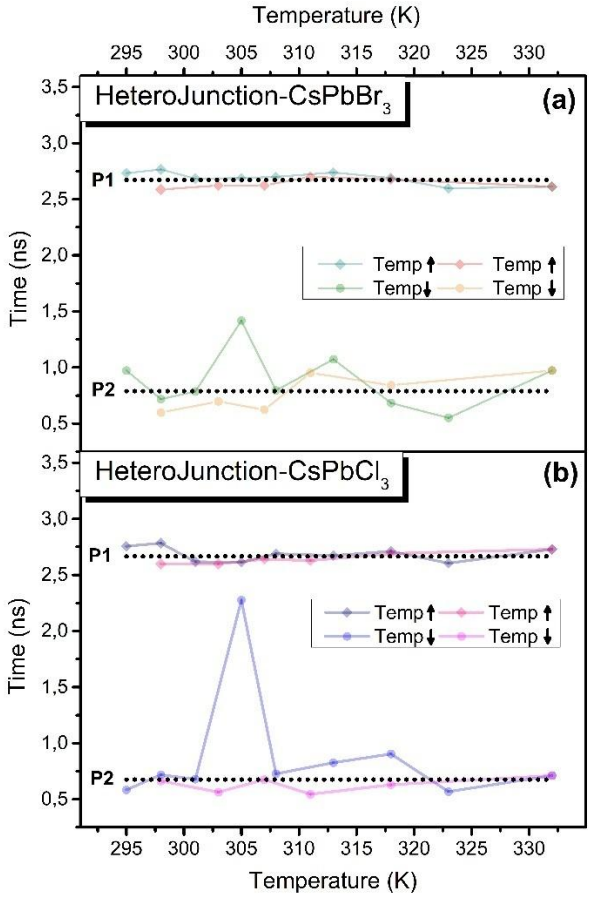

Figure S11. *Comparison of decay times (P1 and P2) for the heterojunctionNWs as a function of temperature. (a) Lifetime trends for the Br-rich region, and (b) Lifetime trends for the Cl-rich region. The black dotted lines represent the average decay times, excluding the 305 K point, highlighting the deviation in lifetime behavior near the phase transition. These results emphasize the differences in excitonic recombination dynamics between the two regions and across different temperatures.*